Transportation Research Part C 173 (2025) 105008

Contents lists available at ScienceDirect

Transportation Research Part C

journal homepage: www.elsevier.com/locate/trc

Dynamic multi-region MFD stochastic user equilibrium: Formulation and parameter estimation in a large-scale case study

Lawrence Christopher Duncan [a,*], Thomas Kjær Rasmussen [a], David Paul Watling [b], Otto Anker Nielsen [a]

[a] Department of Technology, Management and Economics, Technical University of Denmark, Akademivej Bygning 358 2800 Kgs. Lyngby, Denmark
[b] Institute for Transport Studies, University of Leeds, 36-40 University Road, Leeds LS2 9JT United Kingdom

ARTICLE INFO

Keywords:
Multi-region
Macroscopic fundamental diagram
Dynamic model
MFD calibration
GPS trajectory data
Parameter estimation

ABSTRACT

Multi-region Macroscopic Fundamental Diagram (MFD) traffic equilibrium models have been developed as a more easily calibratable, maintainable, and computationally efficient alternative to traditional link-network traffic assignment models with full disaggregate network representation. There are four gaps in the research into these models that we highlight: i) the lack of stochasticity accounted for in the modelling of regional path choice, ii) the estimation of parameters of regional path choice models within the traffic equilibrium, iii) regional path choices being based on region travel times actually experienced (rather than instantaneous travel times), and iv) the paucity of real-life case studies. Motivated by these gaps, this paper presents a new dynamic multi-region MFD Stochastic User Equilibrium (SUE) model, and applies it in a real-life case study. The traffic dynamics are described by a new traffic propagation model utilising features of a space–time graph. Regional path choices can be based on region travel times actually experienced. The model produces continuous equilibrated regional path choice probability outputs, thereby facilitating the development of a rigorous statistical estimation procedure for calibrating parameters from tracked regional path choice data. This estimation procedure is operationalised in a large-scale and detailed multi-region MFD system, with 39 underlying rural and urban regions and 96 directional, superimposed motorway regions, 135 regions in total. Results provide empirical evidence to support hypotheses that regional path choice modelling should consider stochasticity, regional path overlap, multiple attributes, and experienced region travel times. Numerical experiments also demonstrate continuity, differences between the instantaneous and experienced dynamic models, relative insensitivity to the time-slice grain, and realism of the model.

1. Introduction

Region-based Macroscopic Fundamental Diagram (MFD) traffic models have been proposed as an aggregated way of modelling large-scale transport systems. There are several potential advantages of adopting such an aggregated approach over a traditional detailed link-network traffic assignment model. Firstly, the aggregated model should be simpler to calibrate, as it requires data at a

* Corresponding author at: Department of Technology, Management and Economics, Technical University of Denmark, Akademivej Bygning 358, 2800 Kgs. Lyngby, Denmark.
E-mail address: lawdun@dtu.dk (L.C. Duncan).

https://doi.org/10.1016/j.trc.2025.105008
Received 7 May 2024; Received in revised form 10 January 2025; Accepted 12 January 2025
Available online 27 February 2025

coarser grain. For example, the speed-accumulation and/or production-accumulation MFD functions require aggregated data over a large area (region). Detailed models, on-the-other-hand, require link-level calibration, and data may not be available at such a level across the whole area modelled. Moreover, it can often be challenging to connect data to the underlying links due to uncertainties in map-matching from GPS or mobile phone cell data (Quddus et al., 2007). The above also means the aggregated model should be simpler to maintain as circumstances change, a particular challenge with detailed models over such a large scale, typically covering many jurisdictions. Another advantage is that the aggregated model would be expected to be significantly faster computationally than running the detailed link-network model. This is a particular advantage if many scenarios need to be run, or if the model is embedded as a sub-problem in an overall problem concerned with calibration (e.g., Mariotte et al. (2020)), parameter estimation, or optimisation of a design. Furthermore, many policies that one may wish to test, while having a spatial element, may not need a detailed level network to evaluate them.

Region-based MFD traffic models have, for example, been used to model traffic in numerous traffic management studies, such as: route guidance management (Yildirimoglu et al., 2015; Knoop et al., 2012; Hosseinzadeh et al., 2023; Menelaou et al., 2023), traffic control in urban networks (Geroliminis et al., 2012; Keyvan-Ekbatani et al., 2012,2015a,2015b; Ramezani et al., 2015; Haddad et al., 2013; Haddad, 2017a,2017b; Zhong et al., 2018a,2020; Guo & Ban, 2020; Batista et al., 2021a; Fu et al., 2021), parking management (Zheng and Geroliminis, 2016), vehicle dispatching (Ramezani & Nourinejad, 2018; Alisoltani et al., 2020,2021; Beojone & Geroliminis, 2021; Ramezani & Valadkhani, 2023; Valadkhani & Ramezani, 2023), emissions estimation (Barmpounakis et al., 2021; Batista & Leclercq 2020; Batista et al., 2022), and congestion pricing (Amirgholy & Gao, 2017; Chen et al., 2023; Genser & Kouvelas, 2022; Gu et al., 2018,2019; Gu & Saberi, 2021; Wang & Gayah, 2021; Daganzo & Lehe, 2015; Lehe, 2017; Dantsuji et al., 2021; Zheng & Geroliminis, 2013,2020; Mansourianfar et al., 2021,2024). Numerous approaches have been proposed for calibrating MFD parameters, with latest techniques including maximum likelihood estimation (Aghamohammadi & Laval, 2022) and a mean-field variational Bayesian method (Ma et al., 2024), see Ma et al. (2024) for a recent review. And, multimodal "3D" MFDs have been developed to capture the effects of different transport modes on the shape of the MFD function (Geroliminis et al., 2014; Loder et al., 2017; Huang et al., 2019,2022; Fu et al., 2020; Zheng & Geroliminis, 2013,2020; Dantsuji et al., 2021; Johari & Keyvan-Ekbatani, 2024).

The traffic dynamics in region-based MFD traffic models have typically been based on a continuous-time approach, governed by a state equation that associates accumulation of vehicles with balance between inflow and outflow (Batista et al., 2022). Depending on the assumption made of the outflow rate, three models can be distinguished in the literature: the accumulation-based model (Daganzo, 2007; Geroliminis & Daganzo, 2008), the trip-based model (Arnott, 2013; Fosgerau, 2015; Lamotte & Geroliminis, 2016; Mariotte et al., 2017; Leclercq et al., 2017), and the time-delay model (Huang et al., 2020; Zhong et al., 2020). A recent review and comparison of these models can be seen in Huang et al. (2024).

Most region-based MFD traffic models have been concerned with capturing traffic behaviour across a large single region. As Chen et al. (2023) note though, urban networks exhibit high heterogeneity in traffic conditions, and thus a single-region treatment is insufficient for monitoring and control. Multi-region systems have much greater capabilities for capturing heterogeneity in traffic conditions. The area is partitioned into several regions, each with its own MFD function, and traffic travels along sequences of regions (regional paths) from origin to destination region. Regional path choice (traffic assignment) has been determined in several studies through route guidance, aiming to minimise drivers' travel costs (see e.g. Hosseinzadeh et al. (2023), Menelaou et al. (2023)). However, as Guo & Ban (2020) note, in reality, travellers usually try to minimise their own disutilities, implying that determining the regional path choice through a user equilibrium is probably more realistic.

Yildirimoglu & Geroliminis (2014) developed the first multi-region MFD traffic equilibrium model, where a Multinomial Logit (MNL) regional path choice model was adopted for traffic flow equilibration along with a stochastic network loading procedure to estimate time-dependent regional trip lengths. Batista & Leclercq (2019) later developed a monte carlo simulation-based approach for the traffic equilibrium based on drawing from discrete distributions of trip lengths / speed-MFD distributions to account for variability in these attributes. Extending this work, Batista & Leclercq (2020) accounted for bounded rational drivers with indifferent preferences as well as preferences for more travel time reliability. And, Batista et al. (2021b) developed a heuristic approach for updating the traffic-dependent trip lengths / regional paths during the dynamic traffic assignment. Other studies have tended to adopt a Deterministic User Equilibrium (DUE) (Wardrop, 1952) approach for the traffic assignment. For example, Mariotte et al. (2020) adopt a DUE-variant based on travellers minimising average travel times across the entire time horizon. Huang et al. (2020) propose a DUE approach that accounts for time-varying delays as well as departure time choice. Loder et al. (2022) develop a static multi-region multimodal-MFD DUE model and use it to address the network design problem. Wang & Gayah (2021) develop a partly-MFD multi-region DUE model to explore cordon tolling two urban regions to push traffic onto two motorway regions. Guo & Ban, (2020) develop a perimeter control management system where drivers are assumed to follow the DUE principle.

There are four gaps in the research into multi-region MFD traffic equilibrium modelling that we highlight.

The *first* gap regards the lack of stochasticity accounted for in the modelling of regional path choice. Not only are there the usual reasons why stochasticity is typically accounted for, e.g., due to perception errors of travellers, misspecifications of travel cost functions, and/or heterogeneity in preferences (Sheffi, 1985), there are reasons attributed to how actual link-route choices are represented as aggregate regional path choices. For example, uncertainties in the determination of regional path costs from aggregating associated link-route costs, and uncertainties in the partitioning of regions which affects the composition of the regional paths. As noted above, however, the majority of models adopt a DUE approach for the traffic assignment, which neglects any stochasticity. The model developed by Batista & Leclercq (2019) addresses some modelling uncertainties by capturing variability in the regional trip lengths and MFD speeds, but neglects others. The original Yildirimoglu & Geroliminis (2014) model is the only approach to the best of our knowledge that accounts for stochasticity, with the MNL regional path choice model capturing uncertainty in "travellers'

perception of travel time" and "randomness in the system". However, due to the random sampling of origin and destination points during the network loading procedure, it is unclear whether the model will produce continuous outputs as model parameters are varied, and therefore whether model parameters can be estimated according to proper statistical methods. This leads us on to the second gap.

The *second* gap is that no methods have thus far been proposed for estimating parameters of underlying regional path choice models within multi-region MFD traffic equilibrium models. To be able to properly measure levels of stochasticity, measure regional path attribute preferences, or even account for different scales of attributes (e.g., hours − minutes), model parameters need to be estimated according to observed behaviour. However, no such methods have been developed thus far for achieving this.

The *third* gap is that there remains a gap in the literature for models and applications that base regional path choice on experienced travel times. The majority of multi-region MFD traffic equilibrium models have been based on the accumulation-based MFD model, where regional path choices at each departing time interval based on the current/instantaneous region travel times at that interval.[1] However, the traffic state will inevitably evolve during a driver's journey, so that the traffic state actually experienced in latter regions of the regional path may be considerably different from the conditions prevailing in such regions when the driver departed, which has the potential to influence regional path choice. The trip-based model naturally accounts for experienced travel times, but as Huang et al. (2020) note there are several technical barriers involved with implementing the model (see Section 1 of that paper for details). The time-delay model extends the accumulation-based model to account for experienced travel times, but the model has not yet been formulated to account for stochasticity, nor been calibrated and validated in a real-life case study.

The *fourth* gap is the paucity of real-life case studies. Some studies apply proposed models to synthetic multi-region MFD setups (e.g., Yildirimoglu & Geroliminis, 2014; Huang et al., 2020,2024; Guo & Ban, 2020), some apply proposed models to real-life underlying networks but with simulated MFD conditions (e.g., districts of the Lyon network (Batista & Leclercq, 2019,2020)), while studies that set up a real-life multi-region MFD system and apply to it a multi-region MFD traffic equilibrium model are scarce. A notable study is Mariotte et al. (2020), where a multi-region MFD traffic equilibrium model is calibrated and validated for the city of Lyon. However, the system is relatively small-scale, concerned only with a maximum of 5 regions,[2] all of which within the city urban area, and where the motorways are considered as part of the urban MFD.

Motivated by these gaps, in this paper we develop a new dynamic multi-region MFD Stochastic User Equilibrium (SUE) model basing regional path choice on experienced travel times, and estimate and apply the model in a real-life case study. The first thing to note is that the traffic dynamics are based on a new approach, presented as an alternative to the existing continuous-time inflow-outflow model (of which the accumulation, trip, and time-delay models are versions of). The traffic propagation model we develop is based on the same principle as the trip-based model. As Huang et al. (2024) describe, the trip-based model "assumes that travel time depends on the time-varying traffic speed over the course of a trip". Our model is also based on this principle, but the way in which we calculate the time-varying traffic speeds and model the traffic propagation are very different.

The traffic propagation model we develop is a discrete-time traffic propagation model that is designed to operate with fairly large time-slices. For example, we anticipate applying the model to problems concerning time horizons of a day or half-day, with time-slice durations in the order of 15–60 min. The reasons for this are as follows:

- Large time-slices suits the granularity of Origin-Destination (OD) travel demand data that is typically available, which is often coarse-grained. In our case study, for example, 1 h is the finest granularity we have available.
- Even if one has available fine-grained OD demand data, there is often considerable variability in travellers' departure times from day to day. There is thus greater repeatability of travellers departing over an hour or 15 min than over say a minute or second.
- The approach suits the kinds of applications we envisage using the model for. The focus of these applications, rather than being on real-time traffic management, will be on the hypothetical testing of future policies aiming to model a habitual change in travel behaviour. This could be for example exploring congestion pricing, low emissions zones, network changes that alter the shape of the MFD, or part of a multimodal system being used to estimate changes in level of service for car traffic with changes in demand.
- One can operate with a small number of time-slices, which can be tractable in detailed multi-region systems with large numbers of regions.

With fine-grained traffic propagation models, such as the continuous-time inflow-outflow model that is approximated in fine-grained time-slices, traffic only travels short distances within each time-slice, and thus it is feasible to capture traffic propagation incrementally through a Markovian-type approach. With coarse-grained time-slices, however, traffic can travel long distances within each time-slice, travelling in multiple regions with different traffic states, and thus a Markovian-type approach is not suitable. One must therefore consider how traffic propagates within each time-slice. To do this, we develop a new approach that utilises features of a Space-Time Graph (STG). Vehicles departing at the beginning and end of each time-slice travelling on each regional path are tracked from origin to destination on the STG, based on region travel times. These trajectories on the STG are then used to calculate region accumulation levels throughout a time-slice, which feed back to determine average vehicle speeds and thereby region travel times. The traffic propagation model is thus expressed as a fixed-point problem in terms of region travel times.

[1] The Yildirimoglu & Geroliminis (2014) accumulation-based model accounts for experienced travel times but as discussed it is unclear whether the model will produce continuous outputs.

[2] A 10-region MFD system was set up in that study, but the proposed traffic equilibrium model could not be applied due to the DUE "always leading to a global gridlock of the MFD simulation due to overloading of some reservoirs".

Although operating with coarse-grained time-slices requires solving a fixed-point problem, it does mean that one can operate with a much smaller number of time-slices. Another possible advantage of the developed model is that it operates solely with the speed-MFD function (i.e. the production-MFD function is not utilised), which has a simpler shape that can be easier to fit to data, at least this was the case in our case study. Note that although we envisage applying the model with large time-slices, there are no restrictions on how fine-grained the time-slices can be, and one can operate with fine-grained time-slices if one wishes.

The proposed traffic propagation model is integrated within an SUE model for equilibrating regional path flows, where regional path choices can be based on region travel times actually experienced. The consequent model is well-behaved outputting continuous regional path choice probabilities, demonstrated in numerical experiments. This facilitates the development of a statistical estimation procedure for consistently estimating parameters of underlying regional path choice models within the proposed dynamic multi-region MFD SUE model. To be able to estimate the model parameters consistent with the equilibrium this means solving a bi-level maximum likelihood problem subject to equilibrium constraints.

The model is applied in a large-scale and detailed case study concerning the large area of Zealand, Denmark, where there are multiple urban areas (cities/towns) and rural areas (between the cities/towns) partitioned into regions, 39 in total. Aiming to best capture homogeneous traffic conditions and detailed traffic propagation, superimposed upon these urban/rural underlying regions are 96 directional motorway regions treated independently, resulting in a total of 135 regions. This is a far greater number of regions, both of the underlying urban/rural regions and in total, than in any real-life multi-region MFD setup examined thus far. Moreover, treating the motorways separately, and in a detailed manner, we believe is a uniquely attractive feature. This is discussed further in Section 5.1.

The structure of the paper is as follows. In Section 2 we set up the general multi-region MFD system, introducing relevant concepts and notation. In Section 3 we describe, formulate, and demonstrate the STG-based traffic propagation model. In Section 4 we embed the traffic propagation model within a dynamic multi-region MFD SUE model (two versions: Instantaneous and Experienced), demonstrate the contrasting model features in an illustrative example, and propose a solution method. In Section 5 we describe how the case study real-life multi-region MFD system was set up, including how the speed-MFD functions were calibrated. In Section 6 we propose a maximum likelihood estimation procedure for consistently estimating parameters of underlying regional path choice models within the proposed dynamic multi-region MFD SUE model, and then operationalise this procedure to estimate parameters of a new correlation-based regional path choice model in the real-life case study. In Section 7 we conduct a series of numerical experiments to analyse the outputs of the model in the case study. In Section 8 we summarise the work and provide thoughts on future research.

2. General multi-region MFD model setup

In seminal research on aggregated traffic models, Daganzo (2007) and Geroliminis & Daganzo (2008) developed the concept of partitioning road networks into a set of regions R, modelling the traffic conditions in the regions, and modelling how traffic flow exchanges between the regions. Region partitioning has been done through using clustering techniques (e.g., Saeedmanesh & Geroliminis (2016,2017), Lopez et al. (2017), Casadei et al. (2018), Ambühl et al. (2019)) or through trial-and-error considering natural geographical borders, administrative zones, and aiming for compactness / low-scatter MFD functions (Mariotte et al., 2020). Fig. 2 displays an example of an area with a three-region partitioning.

The traffic conditions in each region $r \in R$ are described by a production-MFD function $W_r(n_r)$ (in e.g., [veh.km/hr]), which describes the total distance travelled by all vehicles ([veh.km]) in the region per period of time ([/hr]), as a function of the total number of vehicles, n_r, in the region, also known as the accumulation. An associated speed-MFD function describing the average speed $v_r(n_r)$ (in e.g., [km/hr]) of vehicles in the region given the accumulation is derived as $v_r(n_r) = W_r(n_r)/n_r$. Note that these production-accumulation / speed-accumulation MFD functions are measured at moments in time, e.g., an accumulation of 2000 vehicles in a

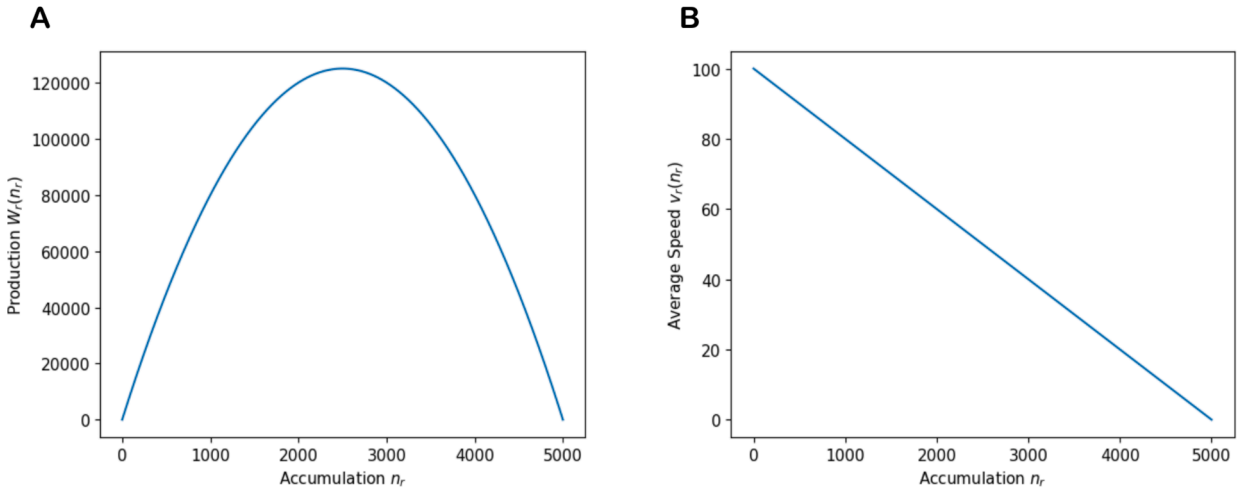

Fig. 1. Example shapes of MFD functions. **A:** Production-MFD ([veh] vs [veh.km/hr]). **B:** Speed-MFD ([veh] vs [km/hr]).

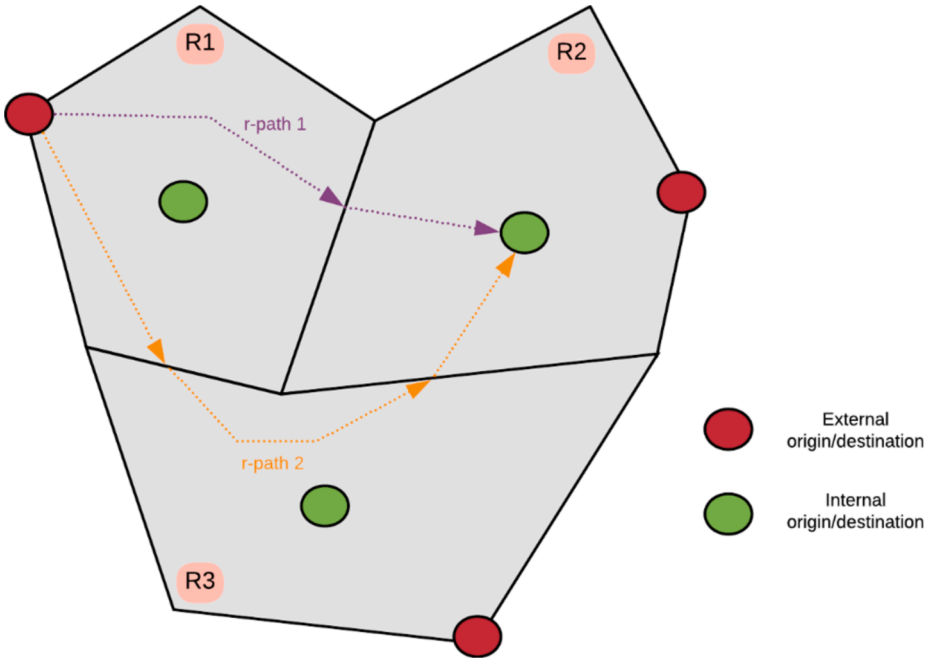

Fig. 2. Example area with a three-region partitioning, displaying the two r-paths for OD movement 1: $(1, 2, 1, 0)$.

region corresponds to them travelling at an average of 50 km/hr at that moment. The existence of this MFD relationship was initially proven by Geroliminis & Daganzo (2008) and later confirmed by other authors (Geroliminis & Sun, 2011; Ambühl & Menendez, 2016; Loder et al., 2017).

Fig. 1A-B display, as an example, a parabolic production-MFD function and corresponding linear speed-MFD function, respectively. As shown for the production-MFD function, a greater number of vehicles travelling in the region results in a greater total distance achieved, where the critical accumulation, n_r^{crit}, achieves maximum production. Too many vehicles in the region results in hyper-congestion however and vehicles cannot travel as far, eventually reaching gridlock at 'jamming accumulation' n_r^{jam} where $W_r\left(n_r^{jam}\right) = 0$. For the speed-MFD function, an increase in accumulation results in a decrease in average speed, up until the jamming accumulation where there is gridlock. Numerous functional forms have been proposed for the production-MFD function, e.g., a polynomial function (Kouvelas et al., 2017; Ramezani et al., 2015; Lamotte & Geroliminis, 2017; Amirgholy & Gao, 2017; Zhong et al., 2018b), exponential function (Amirgholy et al., 2017; Ampountolas et al., 2017; Geroliminis et al., 2014; Zheng & Geroliminis, 2016; Liu & Geroliminis, 2017), a multi-regime linear function (Mariotte et al., 2017; Gao & Gayah, 2018), parabolic function (Batista & Leclercq, 2019; Mariotte et al., 2020), or based on a smooth approximation of the min operator (Ambühl, 2020).

In the developed model in this study, the traffic conditions in each region are measured solely through the speed-MFD function. In general, the model is suitable for standard MFD functions, such as all those detailed above. However, the specification of the speed-MFD function is more flexible in that it is not constrained to satisfying the typical features of the associated production-MFD function $W_r(n_r) = n_r \bullet v_r(n_r)$. For example, there need not be a jamming accumulation n_r^{jam} such that $v_r\left(n_r^{jam}\right) = W_r\left(n_r^{jam}\right) = 0$. In Section 5.2 we fit different speed-MFD functional forms to data.

In the literature, there are two main regional representations. The first, adopted by Yildirimoglu & Geroliminis (2014) and Batista & Leclercq (2021), is the simplest where the system is represented in terms of regions. A regional OD movement is defined as a movement from an origin region to destination region, and a regional path is defined as a sequence of regions from the origin to destination regions. The second, adopted by Mariotte et al. (2020), is more detailed, where the system is represented in terms of macroscopic nodes. A macroscopic node can represent an internal origin/destination, external origin/destination, or region border transfer. A regional OD movement is defined as a movement from an internal or external origin/destination macroscopic node to another, and a regional path is defined as a sequence of macroscopic nodes. This system allows for one to treat external entry/exit points to the area at external region borders separately from internal origins/destinations. And, it allows for one to represent different internal region border crossing points separately.

In this study, we adopt a regional representation that can be seen as a compromise between these two representations. We treat entry/exit points to the area at external region borders separately, but do not represent the system in terms of macroscopic nodes. We allow for each pair of origin and destination regions to have multiple regional OD movements, from an internal or external origin to an internal or external destination. Thus, each regional OD movement is defined by its origin region, destination region, whether its origin is internal or external, and whether its destination is internal or external. Define M as the set of all regional OD movements. For simplicity, we index each regional OD movement, where regional OD movement $m \in M$ corresponds to a specification of

(r^O, r^D, μ^O, μ^D), where r^O and r^D are the origin and destination regions, respectively, and μ^O and μ^D are internal/external origin and destination indicators, respectively. I.e., μ^O is 0 if the origin is from an internal origin of the region and 1 if from an external origin, and μ^D is 0 if the destination is to an internal destination and 1 if to an external destination. For example, suppose in Fig. 2 that regional OD movement $m = 1$ corresponds to going from the external origin of region 1 to the internal destination of region 2, then this corresponds to specification $(1, 2, 1, 0)$. Note that a regional OD movement may have the same origin and destination region, representing traffic originating and destinating within the same region (internally or externally).

A *regional path* (also referred to as r-path) is defined as an ordered sequence of regions travelled in when travelling a regional OD movement. Fig. 2 demonstrates the two regional paths for OD movement 1: r-path 1: R1 → R2, r-path 2: R1 → R3 → R2. For each OD movement $m \in M$ there is a choice set P_m of regional paths, which are assumed to be fixed, and constant throughout time. OD movement $m \in M$ has N_m r-paths, and N is the total number of r-paths: $N = \sum_{m \in M} N_m$. $R_{m,p}$ is the set of regions in r-path $p \in P_m$. Due to the possibility of entering and exiting a region more than once along a regional path, a region may occur multiple times in the sequence of regions. As we will track how flow propagates along a r-path, it is important to distinguish between each occurrence of a region. Therefore, each occurrence of a region in an r-path is represented separately in the set $R_{m,p}$. Note that in theory there should be less uncertainty in regional path choice set generation, since regional paths are less specific about travellers' movements than the actual routes they take.

The model in this paper is a discrete-time dynamic traffic model. We suppose that the total runtime period (e.g., a day or morning/afternoon) is split into equal-sized *time-slices* of duration ε. There are no restrictions on how fine-grained or coarse-grained the time-slices can be, but the more fine-grained the time-slice granularity is, the greater the anticipated realism. Supposing that the time-slices are indexed, let τ denote the indexed time-slice (starting from $\tau = 0$), and let Ψ denote the set of all indexed time-slices. If t_0 is the initial real time of the runtime period, time-slice τ represents the actual time interval $[t_0 + \tau \bullet \varepsilon, t_0 + (\tau + 1) \bullet \varepsilon]$.

The travel demand for OD movement $m \in M$ departing during time-slice $\tau \in \Psi$ is denoted d_m^τ. The travel demand is split then among the available r-paths (according to the regional path choice model, see Section 6.2.2), so that the r-path flow departing during time-slice τ travelling r-path $p \in P_m$ of OD movement m is $f_{m,p}^\tau$. $\boldsymbol{f}_m^\tau$ is the vector of all r-path flows travelling on OD movement m departing during time-slice τ, and $\boldsymbol{f}$ is the vector (of length $N \times |\Psi|$) of all r-path flows travelling all OD movements departing at all time-slices. F denotes the set of all demand-feasible non-negative r-path flow vector solutions for all time-slices $\tau \in \Psi$:

$$F = \left\{ \boldsymbol{f} \in \mathbb{R}_{\geq 0}^{N \times |\Psi|} : \sum_{p \in P_m} f_{m,p}^\tau = d_m^\tau, \forall m \in M, \forall \tau \in \Psi \right\}.$$

Unlike in traditional link-network traffic assignment where the length travelled along a link is the same regardless of which OD movement / route is being travelled, the lengths travelled in a region (*regional trip lengths*) are not the same for each OD movement / regional path. This is because each regional path is associated with a different set of underlying link-routes on the actual network, which may travel different distances through the region (Yildirimoglu & Geroliminis, 2014; Batista et al., 2021a; Batista & Leclercq, 2019; Batista et al., 2021c). Since each regional path is associated with a set of underlying link-routes, where each link-route may travel a different distance through each region of the r-path, some multi-region MFD traffic models have operated with discrete distributions for the regional trip lengths (Batista & Leclercq, 2019). However, although this better captures length heterogeneity and has been shown to have a significant influence on the emulated traffic dynamics (Batista & Leclercq, 2019), in this study, like in many others (e.g., Loder et al., 2022), we operate with the mean regional trip length from the discrete distribution, as this is likely to provide nicer convergence properties for the SUE solution algorithm. Moreover, operating with perceived discrete distributions may result in non-continuous and non-existence of SUE solutions, and may mean the equilibrium is only defined on an interval (see Watling et al. (2015)). Note also that, as will be introduced in Section 5.1, the case study in this paper has separate motorway regions, where the distances travelled along these when travelling the same regional path are often the same. A large proportion of the traffic travels on motorways, and therefore the fact we do not account for the regional trip lengths being distributed is less of an issue in this case study.

Due to for example drivers taking more detoured routes during more congested peak times, the mean regional trip lengths may also be time-dependent (Yildirimoglu & Geroliminis, 2014; Batista et al., 2021b). In this study we operate with mean regional trip lengths that are time-independent, but the model is readily capable to account for such, if one can identify these in the set-up stage.[3] Possibilities for extending the model to make the regional trip lengths consistent with the dynamic traffic conditions are discussed as future research in Section 8.

Denote therefore $l_{m,p,r}$ as the mean regional trip length of region r when travelling r-path $p \in P_m$, constant for all time-slices. The total mean regional trip length of r-path $p \in P_m$ is $L_{m,p} = \sum_{r \in R_{m,p}} l_{m,p,r}$. Note that the regional trip length in this study corresponds to a distance travelled in region r at this stage of the regional path. It is not necessarily the distance to cross the entire region. This is because in this study a region can be travelled in more than once when travelling along a regional path. This is particularly relevant for our real-life case study where there are cases where a link-route enters and exits a motorway within the same underlying region (see Section 5). So, a region may be travelled in multiple times along a regional path, but its regional trip length each time will be different, representing it travelling a different portion of the region. For the remainder of the paper, however, for simplicity we shall consistently refer

[3] In our generation of regional paths and regional trip lengths in the real-life case study in this paper (see Section 5.4), we explored whether conducting shortest path searches based on time-dependent congested link travel times from an underlying network equilibrium model led to different regional paths / regional trip lengths for different times of day, but we found only very small variations.

to regional paths as crossing regions, to avoid what is a minor point complicating the discussion.

Lastly, for a given accumulation n_r in region r (at a given moment in time), corresponding to an average MFD speed $v_r(n_r)$ in the region, and given mean regional trip length $l_{m,p,r}$, the mean travel time $t_{m,p,r}$ to cross region r when travelling r-path $p \in P_m$ is:

$$t_{m,p,r}(n_r) = \frac{l_{m,p,r}}{v_r(n_r)}.$$

$l_{m,p,r}$ is the mean regional trip length and $t_{m,p,r}$ is the mean region travel time, but henceforth for simplicity we shall just refer to $l_{m,p,r}$ as the regional trip length and $t_{m,p,r}$ as the region travel time.

For a table of the main nomenclature used in this paper, see Appendix A.

3. Traffic propagation model

Embedded within the dynamic multi-region MFD SUE model is a traffic propagation model based on utilising features of a Space-Time Graph (STG).

The general assumptions of the traffic propagation model are as follows:

- The total runtime duration is divided into discrete equal-sized time-slices.
- The travel demand at each time-slice departs uniformly and continuously during the time-slice.
- Throughout each time-slice, all drivers are assumed to be experiencing the same speed in a region.

For a thorough walk-through of the features of the model with explanatory illustrations we direct the reader to Appendix B. To demonstrate the model, Fig. 3 displays on a STG the propagation of a vehicle flow travelling a 5-region r-path departing during time-slice 0.[4] The constant region travel times throughout each time-slice are given in the top left corner of each quadrant for each region/time-slice. Given these region travel times, the vehicles departing at the beginning and end of time-slice 0 are tracked from origin to destination on the STG, as depicted in the figure. The entire r-path flow at any moment in time will be contained in space between the first and last departing vehicles. The *occupying STG area* of r-path flow is the area of a region/time-slice quadrant of the STG that is occupied by any vehicle of the r-path flow during the time-slice. In Fig. 3 these areas are shaded in blue, clearly determined by the first and last departing vehicle trajectories. As will be explained below, occupying STG areas of r-path flows are used to calculate region accumulation levels. These feed back to determine average vehicle speeds in a region during a time-slice (through the speed-MFD function), and thereby region travel times. The traffic propagation model is thus expressed as a fixed-point problem in terms of region travel times.

There are two key features of the model:

i) The constant average speed of vehicles in a region during a time-slice is calculated by inserting the average accumulation in the region during the time-slice into the speed-MFD function.
ii) The average contributing accumulation in a region during a time-slice from a given r-path flow, is calculated by proportioning the r-path flow between the regions in the r-path according to its proportional occupying STG area for that time-slice, weighted by regional trip length.

Regarding i), since MFDs operate in terms of estimating the space-mean speed of vehicles in a region given an accumulation level at a given moment in time, to obtain the average speed of vehicles in a region during a time-slice, one would ideally take a large number of draws of accumulation levels at different moments in time throughout the time-slice (summing the accumulation contributions from all r-path flows), input each of these accumulation levels into the speed-MFD function to determine the speeds at these moments in time, and then take an average. However, doing this is complex, has the potential to be computationally burdensome, and may be inaccurate, depending on the number of draws.

We therefore adopt a more computationally efficient and rigorous approach. We instead use the occupying areas of the r-path flow in each region at each time-slice in the STG, to work out the average accumulation in a region over the time-slice (see regarding ii) below). This average accumulation level is then inputted into the speed-MFD function to approximate the average speed in the region during the time-slice.[5] The more fine-grained the time-slice grain is, the better the approximation. For example, accumulation levels are likely to vary less at a time-slice grain of 15 min compared to 1 h. As we show in Section 7.3 though, the overall results are relatively insensitive to the time-slice grain.

Regarding ii), as shown in Fig. 3, the propagation of the entire regional path flow departing at each time-slice is contained within the trajectories of the first/last vehicles departing at the beginning/end of the time-slice. At any given moment in time, regional path flow will be spread across the region(s) between where the first and last departing vehicles are. The flow is spread across the regions between where the first and last vehicles are according to the occupied regional trip lengths of the regions at that moment of time, as

[4] Note that every regional path has its own STG, for its own sequence of regions.

[5] Note that when adopting a linear speed-MFD function (e.g., as adopted by Batista & Leclercq (2019) & Mariotte et al. (2020)), this works out to be equivalent to taking an infinite number of draws of MFD speed values and taking an average (i.e. the ideal model described).

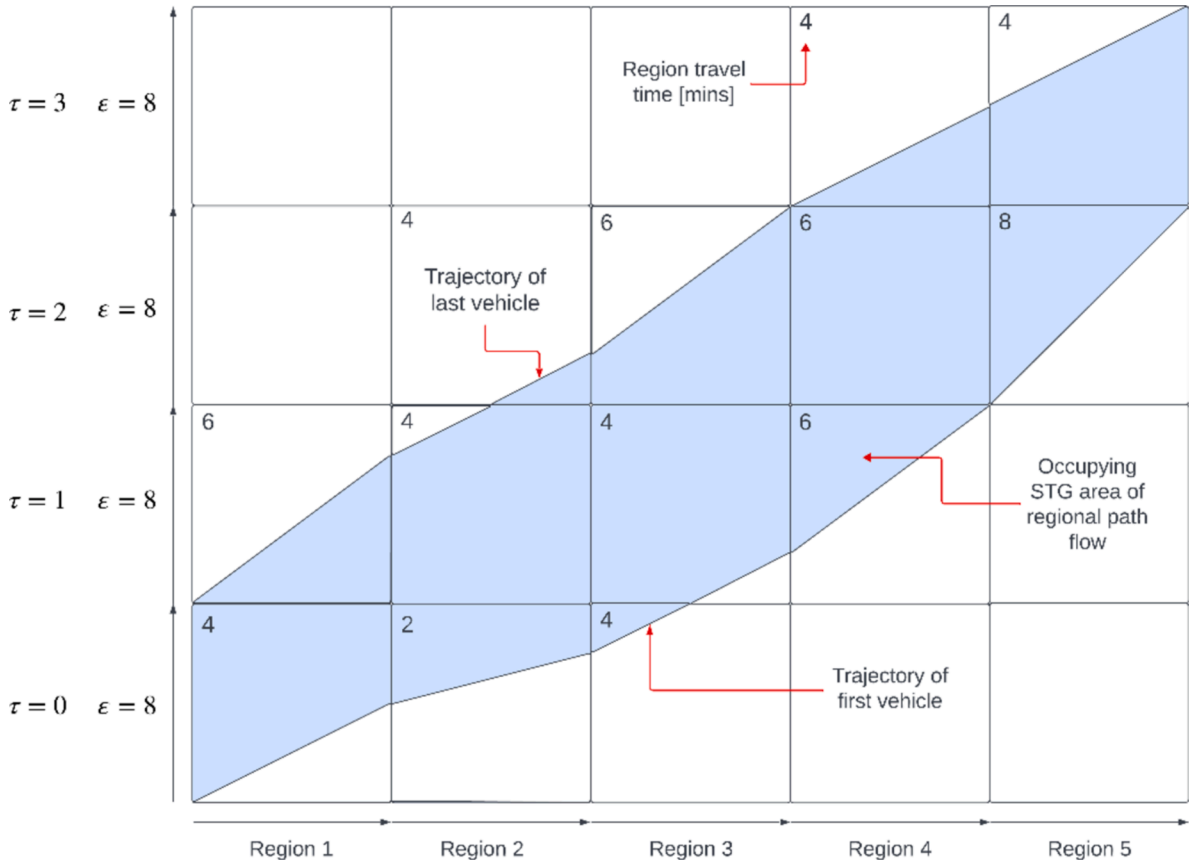

Fig. 3. Example of a flow trajectory on a space–time graph, for a regional path with 5 regions. Spatial X-axis is proportion of region completed (Note that a region can be travelled in multiple times along a regional path, travelling different portions of the region each time.) and temporal Y-axis is proportion of time-slice completed.

depicted in Fig. 4. Taking an infinite number of draws of the occupied lengths at every moment of time during a time-slice, one can consequently work out the region accumulations at every moment in time and take an average to obtain the average accumulation level. This can neatly be done though by using the occupying areas of the r-path flow: the contributing average accumulation in each of an r-path's regions during a time-slice, is calculated by proportioning the r-path flow between the regions in the r-path according to their proportional occupying STG area for that time-slice, weighted by regional trip length, as depicted in Fig. 5.

The model is formulated as follows. From the general assumptions above, it is assumed that during time-slice τ, all drivers who occupy region r experience the same speed, and thus the time it takes to cross region r when travelling r-path $p \in P_m$ is constant throughout τ. $t^{\tau}_{m,p,r}$ thus denotes the travel time to cross region r when entering the region during time-slice τ when travelling r-path $p \in P_m$ (we shall show how this is calculated later in (4)). Denote $\boldsymbol{t}$ as the vector of all r-path region travel times at all time slices. For a given vector of all r-path flows departing at all time-slices, $\boldsymbol{f}$, the traffic propagation model determines the consequent r-path region travel times $\boldsymbol{t}$.

As per i) above, the assumed constant average speed of vehicles in a region during a time-slice is calculated by inserting the average accumulation in the region during the time-slice into the speed-MFD function. The average speed in region r during time-slice τ, $\overline{v}^{\tau}_{r}$, is thus computed as follows:

$$\overline{v}^{\tau}_{r}(\boldsymbol{t},\boldsymbol{f}) = v_r\left(\overline{n}^{\tau}_{r}(\boldsymbol{t},\boldsymbol{f})\right), \tag{1}$$

where v_r is the speed-MFD function for region r, and $\overline{n}^{\tau}_{r}$ is the average accumulation in region r during time-slice τ, for a given r-path region travel time vector $\boldsymbol{t}$ and r-path flow vector $\boldsymbol{f}$. $\overline{n}^{\tau}_{r}$ is calculated by summing up all the average accumulations contributed by each r-path flow traversing the region:

$$\overline{n}^{\tau}_{r}(\boldsymbol{t},\boldsymbol{f}) = \sum_{m\in M}\sum_{p\in P_m}\sum_{\tau'\in\Psi^{\leq\tau}} \overline{n}^{\tau'\to\tau}_{m,p,r}(\boldsymbol{t},\boldsymbol{f}), \tag{2}$$

where $\Psi^{\leq\tau}$ is the set of time-slices preceding and including time-slice τ, and $\overline{n}^{\tau'\to\tau}_{m,p,r}$ is the average accumulation in region r during time-slice τ from the flow travelling r-path $p \in P_m$ departing during time-slice τ', given $\boldsymbol{t}$ and $\boldsymbol{f}$. As per ii) above, $\overline{n}^{\tau'\to\tau}_{m,p,r}$ is calculated by

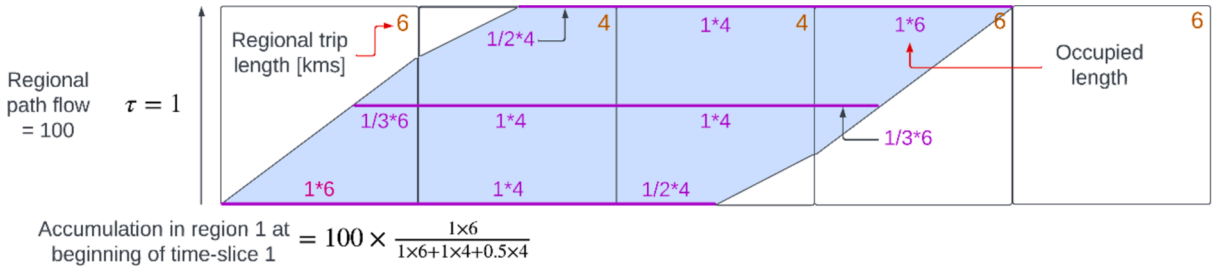

Fig. 4. Demonstration of occupying region lengths of regional path flow at different moments in time and calculation of accumulation.

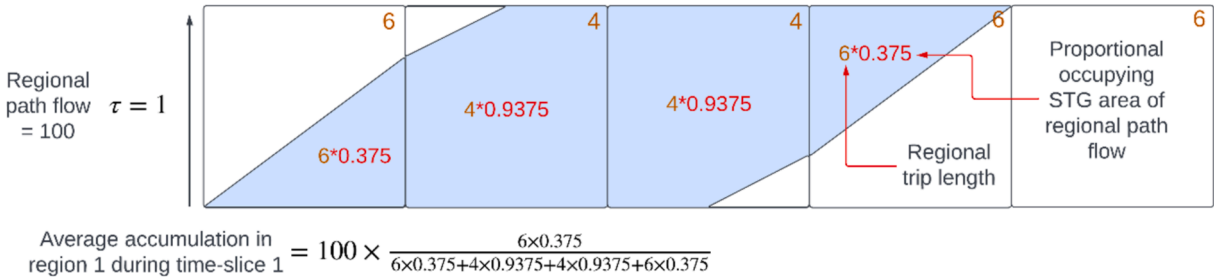

Fig. 5. Demonstration of proportional occupying STG areas of regional path flow weighted by regional trip length and calculation of average accumulation levels.

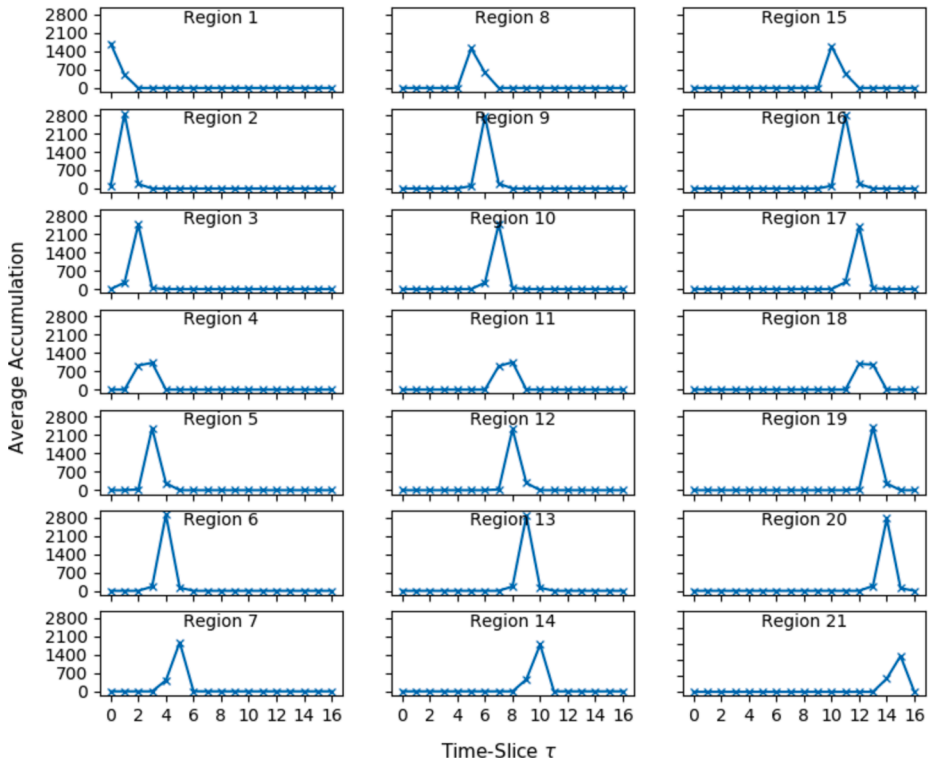

Fig. 6. 21-region line regional system: average accumulation in each region during each time-slice.

proportioning the r-path flow between the regions in the r-path according to its proportional occupying STG area for that time-slice, weighted by regional trip length:

$$\overline{n}^{\tau' \to \tau}_{m,p,r}(\boldsymbol{t},\boldsymbol{f}) = \frac{l_{m,p,r} A^{\tau' \to \tau}_{m,p,r}(\boldsymbol{t})}{\sum_{k \in R_{m,p}} l_{m,p,k} A^{\tau' \to \tau}_{m,p,k}(\boldsymbol{t})} \bullet f^{\tau'}_{m,p}, \tag{3}$$

where $l_{m,p,r}$ is the regional trip length of region r when travelling r-path $p \in P_m$ during time-slice τ, and $A^{\tau' \to \tau}_{m,p,r} \in [0,1]$ is the proportional occupying STG area of region r time-slice τ, of the flow departing during time-slice τ' travelling r-path $p \in P_m$. Fig. 5 for example displays the proportional occupying STG areas of regions 1–4 at time-slice 1 of the flow departing during time-slice $\tau' = 0$ travelling r-path 1 of OD movement 1: $A^{0\to1}_{1,1,1} = 0.375$, $A^{0\to1}_{1,1,2} = 0.9375$, $A^{0\to1}_{1,1,3} = 0.9375$, and $A^{0\to1}_{1,1,4} = 0.375$.

Computing the proportional occupying STG areas requires tracking the trajectories of the first and last vehicles departing at the beginning/end of each departing time-slice. However, describing the part of the model formulation for tracking trajectories and consequently computing areas cannot be done concisely, as for example there are 25 possibilities for the area, computed by calculating simple areas of triangles and trapeziums. Therefore, in order to maintain a concise main body of paper, we direct the reader to Appendix C for details on this.

Now, r-path region travel times depend on average region speeds. However, as shown (1), the average region speeds depend on the average region accumulations, which in turn depend on how the flow propagates given the r-path region travel times. The r-path region travel times are therefore a solution to a fixed-point problem. For a given r-path flow vector $\boldsymbol{f}$, the r-path region travel times are a solution to the fixed-point problem $\boldsymbol{t} = \boldsymbol{H}(\boldsymbol{t},\boldsymbol{f})$, where $H^{\tau}_{m,p,r}$ for region r travelling r-path $p \in P_m$ departing during time-slice τ is:

$$H^{\tau}_{m,p,r}(\boldsymbol{t},\boldsymbol{f}) = \frac{l_{m,p,r}}{\overline{v}^{\tau}_{r}(\boldsymbol{t},\boldsymbol{f})}, \tag{4}$$

where $l_{m,p,r}$ is the regional trip length and $\overline{v}^{\tau}_{r}$ is the average speed in region r during time-slice τ given in (1), given $\boldsymbol{t}$ and $\boldsymbol{f}$.

To demonstrate the traffic propagation model, consider a regional system where there are 21 regions in a line. There is 1 OD movement and 1 regional path from region 1 to region 21. Each region has regional trip length 10 and the speed-MFD function for each region r is: $v_r(n_r) = -0.02n_r + 100$. Fig. 1B plots this speed-MFD function. As shown, it is strictly decreasing with accumulation, has free-flow speed of 100, and the critical and jam accumulations are 2500 and 5000, respectively. The free-flow travel time of each region is thus 0.1. There are 17 time-slices (i.e. $\tau = 0$ to $\tau = 16$). We shall track how a demand surge of $d^0 = f^0 = 3600$ vehicles at time-slice $\tau = 0$ propagates through the regional system, where the demand at all other time-slices is 0. The time-slice duration is $\varepsilon = 0.2$. Upon solution of the traffic propagation model for the given r-path flow, Fig. 6 displays the average accumulation in each region for

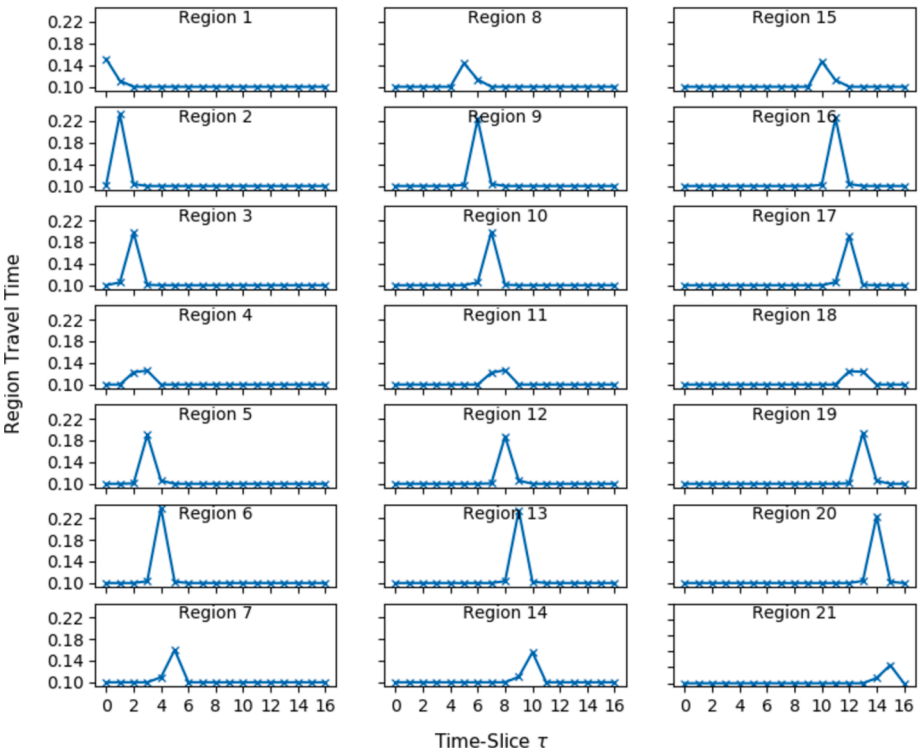

Fig. 7. 21-region line regional system: travel time of each region at each time-slice.

time-slice 0 to 16. Fig. 7 displays the travel time of each region for time-slice 0 to 16. As shown, the r-path flow propagates from origin to destination, traversing each region before reaching region 21 at time-slice 14 and destinating fully by time-slice 16. The connection between region travel time and accumulation levels is clear to see between the two figures. Clearly, congestion causes congestion, where there is a direct feedback between accumulation and speed.

The proposed traffic propagation model satisfies desirable traffic flow theory properties such as First In, First Out (FIFO) and causality. According to Carey et al. (2014), there are different characterisations of FIFO that can be defined for road traffic link-networks. These are all built around the following general definition, which has also been used by Huang et al. (2024) to investigate FIFO for MFD models (see Definition 3.1 in that paper):

FIFO condition for link-networks: Let t_1 and t_2 be any two times such that $t_1 < t_2$. Then, FIFO holds if and only if:

$$t_1 + h(t_1) < t_2 + h(t_2),$$

where $h(t_1)$ and $h(t_2)$ are the link travel times for vehicles entering the link at times t_1 and t_2, respectively.

Although it is not stated as it is natural in the case of links, it is assumed that all vehicles travel the same distance to traverse a link. In region traffic modelling, however, vehicles travel different distances to traverse a region, depending on the regional path they are travelling. Thus, it is possible for a vehicle travelling one regional path to enter a region before a vehicle travelling on another, and to exit later. This does not mean though that any overtaking on links in the region has occurred. The FIFO condition is only relevant for regional paths that travel the same distance through a region. Thus, we modify the FIFO condition for region-based traffic models:

FIFO condition for regional-networks: Let t_1 and t_2 be any two times such that $t_1 < t_2$. Then, FIFO holds if and only if, for vehicles travelling the same distance through a region:

$$t_1 + h(t_1) < t_2 + h(t_2),$$

where $h(t_1)$ and $h(t_2)$ are the region travel times for vehicles entering the region at times t_1 and t_2, respectively.

FIFO is ensured with our proposed traffic propagation model as all vehicles are assumed to travel the same speed in a region throughout each time-slice. Therefore, if any two vehicles travel the same distance through a region, the vehicle entering first will exit first. This is evident from the STG traffic propagation in Fig. 3: the first departing vehicle is always first to exit. Relating to the link-network FIFO condition, if two vehicles are on the same link in a region, because they are always assumed to be travelling the same speed, the vehicle behind can never overtake.

Regarding causality, Carey (2004a,b) defines strict causality and partial causality as follows:

- Strict causality: the speed, and hence travel time, of a vehicle is affected by the behaviour (usually speed) of vehicles ahead but not by vehicles behind.
- Partial causality: the speed and travel time of a vehicle is affected by vehicles ahead and also by vehicles behind.

Since the constant speed at which vehicles are assumed to be travelling through a region during a time-slice is dependent on the average accumulation in the region during the time-slice, the speed of vehicles during that time-slice is affected by vehicles both behind and ahead in time in the region (during that time-slice). Therefore, within each time-slice, there is only partial causality. Between time-slices, however, vehicle speeds are only influenced by vehicles (accumulation levels) ahead in succeeding time-slices, and therefore strict causality is ensured across time-slices. Thus, by making the time-slice grain more fine-grained, one can decrease the extent to which strict causality is violated.

Note that as Huang et al. (2024) find, the accumulation-based and trip-based MFD models uphold the FIFO condition, while the time-delay MFD model only upholds the FIFO condition under three sufficient conditions. And, the time-delay model upholds strict causality, while the accumulation-based and trip-based MFD models only uphold partial causality.

Summarising, the main desirable properties of the traffic propagation model we propose are as follows:

- Vehicles are tracked from origin to destination region in space and time, capturing the propagation of traffic.
- Congestion causes congestion, where there is a direct feedback between accumulation and speed.
- Traffic propagation is based on experienced travel times.
- Flow conservation is maintained.
- FIFO is ensured.
- There is partial causality within each time-slice and strict causality across time-slices.
- There are no restrictions to how fine or coarse the time-slice granularity should be.

4. Dynamic multi-region MFD stochastic user equilibrium

In this section, we embed the traffic propagation model developed in Section 3 within a Dynamic MR-MFD-SUE (D-MR-MFD-SUE) model. There are two versions of the model: in version 1 the regional path choice is based on the r-path region travel times at the current departing time-slice (i.e. instantaneous travel times), and in version 2 the regional path choice is based on r-path region travel times actually experienced at the time of travel (i.e. experienced travel times).

4.1. Instantaneous model

In this section, we introduce the Instantaneous D-MR-MFD-SUE (ID-MR-MFD-SUE) model, otherwise referred to as the ID model, where regional path choice is based on instantaneous r-path region travel times at the current departing time-slice. Literature discussing instantaneous dynamic link-network traffic assignment include Boyce et al. (2001), Wismans et al. (2011), and Wu et al. (2024).

For a given r-path flow vector $\boldsymbol{f}$, the traffic flow propagation model in Section 3 determines the consequent r-path region travel times $\boldsymbol{t}(\boldsymbol{f})$. The ID model assumes that the r-path region travel times the r-path choice is based on when departing during time-slice τ are the current travel times at time-slice τ: $t^{\tau}_{m,p,r}$, where the total (current) travel time of r-path $p \in P_m$ at time-slice τ is: $T^{\tau}_{m,p}(\boldsymbol{t}(\boldsymbol{f})) = \sum_{r \in R_{m,p}} t^{\tau}_{m,p,r}(\boldsymbol{f})$. Thus, for a given vector of all r-path region travel times, $\boldsymbol{t}(\boldsymbol{f})$, for a given r-path flow vector, the choice probability of r-path $p \in P_m$ at time-slice $\tau \in \Psi$, $Q^{\tau}_{m,p}(\boldsymbol{t}(\boldsymbol{f}))$, is computed according to the relevant r-path choice model (see Section 6.2.2), based upon region travel times at τ. Denote $\boldsymbol{Q}^{\tau}_{m}$ as the vector of r-path choice probabilities for OD movement $m \in M$. ID-MR-MFD-SUE conditions are formulated as follows:

ID-MR-MFD-SUE: A r-path flow vector $\boldsymbol{f}^{*} \in F$, of all r-path flows at all departing time-slices $\tau \in \Psi$, is a ID-MR-MFD-SUE solution if and only if the r-path flow vector for OD movement m at time-slice $\tau \in \Psi$, $\boldsymbol{f}^{\tau,*}_{m}$, is a solution to the fixed-point problem

$$\boldsymbol{f}^{\tau}_{m} = \boldsymbol{D}^{\tau}_{m} \boldsymbol{Q}^{\tau}_{m}(\boldsymbol{t}^{*}(\boldsymbol{f})), \qquad \forall m \in M, \forall \tau \in \Psi, \tag{5}$$

where $\boldsymbol{D}^{\tau}_{m}$ is the $N_m \times N_m$ diagonal matrix of the travel demand for OD movement m at time-slice τ (i.e. with d^{τ}_{m} on each diagonal element), $Q^{\tau}_{m,p}$ is the choice probability for r-path $p \in P_m$ at time-slice $\tau \in \Psi$, given $\boldsymbol{t}^{*}$ which is a r-path region travel time solution in $\boldsymbol{t}$ to the fixed-point problem $\boldsymbol{t} = \boldsymbol{H}(\boldsymbol{t}, \boldsymbol{f})$, where $H^{\tau}_{m,p,r}(\boldsymbol{t}, \boldsymbol{f})$ is as in (4) for region r traversing r-path $p \in P_m$ departing at time-slice τ, given the r-path flow vector $\boldsymbol{f}$.

Note that in this study, congestion capacities and receiving capacities of regions are not considered in the traffic equilibrium, and thus there are no restrictions in the management of the outflow/inflow between adjacent regions. We assume that gridlock accumulation levels are never experienced (congestion capacities), and that there are no capacity constraints at region borders (receiving capacities). In our real-life case study, we did not experience any (realistic) accumulation levels that may cause gridlock in a region, nor do we have any bottlenecks at region borders. That being said, it is possible to extend the model to account for capacity constraints and the management of outflow/inflow between adjacent regions, which we discuss as future research in Section 8.

4.2. Experienced model

In this section, we introduce the Experienced Dynamic MR-MFD-SUE (ED-MR-MFD-SUE) model, otherwise referred to as the ED model, where regional path choice is based on experienced r-path region travel times actually experienced, i.e. the travel times at the

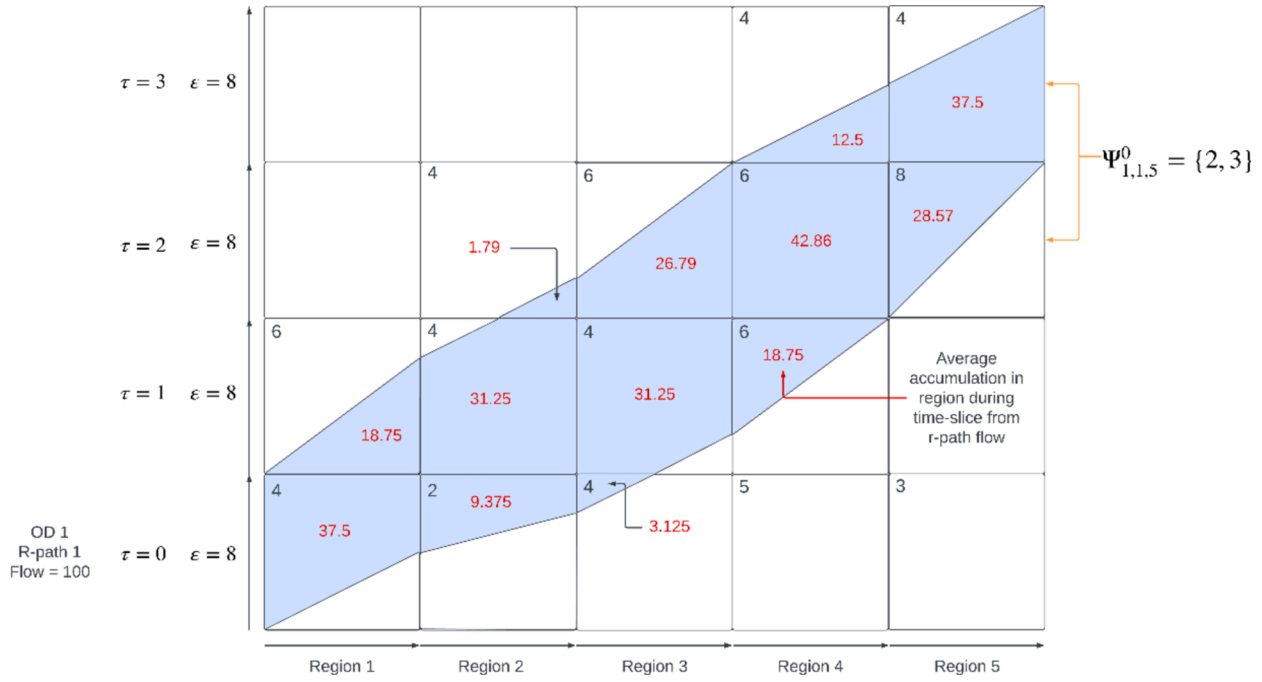

Fig. 8. Illustrating average contributing accumulations from the r-path flow in the regions during each time-slice.

time-slice the region is being traversed. Literature discussing experienced dynamic link-network traffic assignment include Janson (1991a,b), Ameli et al. (2020), and Lentzakis et al. (2023).

One of the key assumptions of the traffic propagation model is that the demand departs continuously and uniformly during the departing time-slice. As such, the demand experiences different travel times depending on when it departs during the time-slice. It is assumed though that the demand at each departing time-slice has the same regional path choice. We therefore suppose that this regional path choice is based upon the *average* experienced travel time from the flow departing at different times. The average experienced travel time of region r travelling r-path $p \in P_m$ departing during time-slice τ, $\bar{t}^{\tau}_{m,p,r}$, is calculated as follows:

$$\bar{t}^{\tau}_{m,p,r}(\boldsymbol{t},\boldsymbol{f}) = \sum\nolimits_{\tau' \in \Psi^{\tau}_{m,p,r}} \frac{\overline{n}^{\tau\to\tau'}_{m,p,r}(\boldsymbol{t},\boldsymbol{f})}{\sum_{\tau'' \in \Psi^{\tau}_{m,p,r}} \overline{n}^{\tau\to\tau''}_{m,p,r}(\boldsymbol{t},\boldsymbol{f})} \bullet t^{\tau'}_{m,p,r}, \tag{6}$$

where $\Psi^{\tau}_{m,p,r}$ is the set of *active time-slices* that some time is spent in traversing region r by any vehicle departing during time-slice τ travelling r-path $p \in P_m$ (see Fig. 8 for a demonstration). So, the average travel time of region r is a weighted average of the region travel times in succeeding time-slices the flow travels the region in, i.e. $t^{\tau'}_{m,p,r}$ for $\tau' \in \Psi^{\tau}_{m,p,r}$, where the weighting for succeeding time-slice τ' is its average contributing accumulation $\overline{n}^{\tau\to\tau'}_{m,p,r}$. The total average experienced travel time of r-path $p \in P_m$ when departing during time-slice τ is $\overline{T}^{\tau}_{m,p}(\bar{\boldsymbol{t}}(\boldsymbol{t},\boldsymbol{f})) = \sum_{r \in R_{m,p}} \bar{t}^{\tau}_{m,p,r}(\boldsymbol{t},\boldsymbol{f})$.

For a given r-path flow vector $\boldsymbol{f}$, and thereby vector of region travel times from the traffic flow propagation model, $\boldsymbol{t}(\boldsymbol{f})$, the vector of all average experienced region travel times is $\bar{\boldsymbol{t}}(\boldsymbol{t}(\boldsymbol{f}),\boldsymbol{f})$. Thus, for a given $\bar{\boldsymbol{t}}(\boldsymbol{t}(\boldsymbol{f}),\boldsymbol{f})$, the choice probability of r-path $p \in P_m$ at time-slice $\tau \in \Psi$, $Q^{\tau}_{m,p}(\bar{\boldsymbol{t}}(\boldsymbol{t}(\boldsymbol{f}),\boldsymbol{f}))$, is computed according to the relevant r-path choice model (see Section 6.2.2). ED-MR-MFD-SUE conditions are formulated as follows:

ED-MR-MFD-SUE: A r-path flow vector $\boldsymbol{f}^{*} \in F$, of all r-path flows at all departing time-slices $\tau \in \Psi$, is a ED-MR-MFD-SUE solution if and only if the r-path flow vector for OD movement m at time-slice $\tau \in \Psi$, $\boldsymbol{f}^{\tau,*}_{m}$, is a solution to the fixed-point problem

$$\boldsymbol{f}^{\tau}_{m} = \boldsymbol{D}^{\tau}_{m}\boldsymbol{Q}^{\tau}_{m}(\bar{\boldsymbol{t}}(\boldsymbol{t}^{*}(\boldsymbol{f}),\boldsymbol{f})), \quad \forall m \in \boldsymbol{M}, \forall \tau \in \Psi, \tag{7}$$

where $Q^{\tau}_{m,p}$ is the choice probability for r-path $p \in P_m$ at time-slice $\tau \in \Psi$, given $\boldsymbol{t}^{*}$ which is a r-path region travel time solution in $\boldsymbol{t}$ to the fixed-point problem $\boldsymbol{t} = \boldsymbol{H}(\boldsymbol{t},\boldsymbol{f})$, where $H^{\tau}_{m,p,r}(\boldsymbol{t},\boldsymbol{f})$ is as in (4) for region r traversing r-path $p \in P_m$ departing at time-slice τ, given the r-path flow vector $\boldsymbol{f}$.

4.3. Illustrative example

To demonstrate the difference between the ID and ED models in terms of the travel times used for the r-path choice, consider the STG in Fig. 8 which displays the average accumulations in the regions during each time-slice, given the r-path flow is $f^{0}_{1,1} = 100$ for the flow departing during time-slice 0 travelling OD 1 r-path 1. For the ID model, the r-path region travel times used for the r-path choice are the travel times at the time-slice of departure: $t^{0}_{1,1,1} = 4$, $t^{0}_{1,1,2} = 2$, $t^{0}_{1,1,3} = 4$, $t^{0}_{1,1,4} = 5$, & $t^{0}_{1,1,5} = 3$, for regions 1–5, respectively. For the ED model, however, the r-path region travel times used for the r-path choice are the average experienced travel times experienced, calculated from (6) for regions 1–5 as follows:

$$\bar{t}^{0}_{1,1,1} = \sum\nolimits_{\tau' \in \{0,1\}} \frac{\overline{n}^{0\to\tau'}_{1,1,1}}{\sum_{\tau'' \in \{0,1\}} \overline{n}^{0\to\tau''}_{1,1,1}} \bullet t^{\tau'}_{1,1,1} = \frac{37.5}{37.5+18.75} \bullet 4 + \frac{18.75}{37.5+18.75} \bullet 6 = 4.67,$$

$$\bar{t}^{0}_{1,1,2} = \sum\nolimits_{\tau' \in \{0,1,2\}} \frac{\overline{n}^{0\to\tau'}_{1,1,2}}{\sum_{\tau'' \in \{0,1,2\}} \overline{n}^{0\to\tau''}_{1,1,2}} \bullet t^{\tau'}_{1,1,2}$$

$$= \frac{9.375}{9.375+31.25+1.79} \bullet 2 + \frac{31.25}{9.375+31.25+1.79} \bullet 4 + \frac{1.79}{9.375+31.25+1.79} \bullet 4 = 3.56,$$

$$\bar{t}^{0}_{1,1,3} = \sum\nolimits_{\tau' \in \{0,1,2\}} \frac{\overline{n}^{0\to\tau'}_{1,1,3}}{\sum_{\tau'' \in \{0,1,2\}} \overline{n}^{0\to\tau''}_{1,1,3}} \bullet t^{\tau'}_{1,1,3}$$

$$= \frac{3.125}{3.125+31.25+26.79} \bullet 4 + \frac{31.25}{3.125+31.25+26.79} \bullet 4 + \frac{26.79}{3.125+31.25+26.79} \bullet 6 = 4.88,$$

$$\bar{t}^{0}_{1,1,4} = \sum\nolimits_{\tau' \in \{1,2,3\}} \frac{\overline{n}^{0\to\tau'}_{1,1,4}}{\sum_{\tau'' \in \{1,2,3\}} \overline{n}^{0\to\tau''}_{1,1,4}} \bullet t^{\tau'}_{1,1,4}$$

$$= \frac{18.75}{18.75+42.86+12.5} \bullet 6 + \frac{42.86}{18.75+42.86+12.5} \bullet 6 + \frac{12.5}{18.75+42.86+12.5} \bullet 4 = 5.12,$$

$$\bar{t}^{0}_{1,1,5} = \sum_{\tau' \in \{2,3\}} \frac{\bar{n}^{0\to\tau'}_{1,1,5}}{\sum_{\tau'' \in \{2,3\}} \bar{n}^{0\to\tau''}_{1,1,5}} \bullet t^{\tau'}_{1,1,5}$$

$$= \frac{28.57}{28.57 + 37.5} \bullet 4 + \frac{37.5}{28.57 + 37.5} \bullet 8 = 5.73.$$

Thus, there may be some considerable differences between the region travel times used for the r-path choice between the ID and ED models.

To further demonstrate the difference between ID and ED r-path choice travel times, consider again the 21-region regional system detailed in Section 3. For ID, r-path choice is based on the region travel times at the departing time-slice, which in this case is time-slice 0. As shown in Fig. 6 & Fig. 7, during time-slice 0 only regions 1 & 2 are traversed by the flow and therefore have non-free-flow travel times. However, as the r-path flow propagates along the regional path, the r-path flow will contribute to the region accumulations it will experience as it travels, which will mean free-flow speeds will not be experienced in regions after 1 & 2. The ED model is able to capture this as it tracks the region travel times actually experienced at the point of travel.

4.4. Solution method

Here we propose a method for solving the ID and ED models, where for the ED model there is an additional step for calculating the average experienced region travel times for the r-path choice. Pseudo-code for the solution method is given in Algorithm 1, and Fig. 9 presents a schematic diagram illustrating the method. As evident from (5) and (7), the ID and ED models are a fixed-point problem

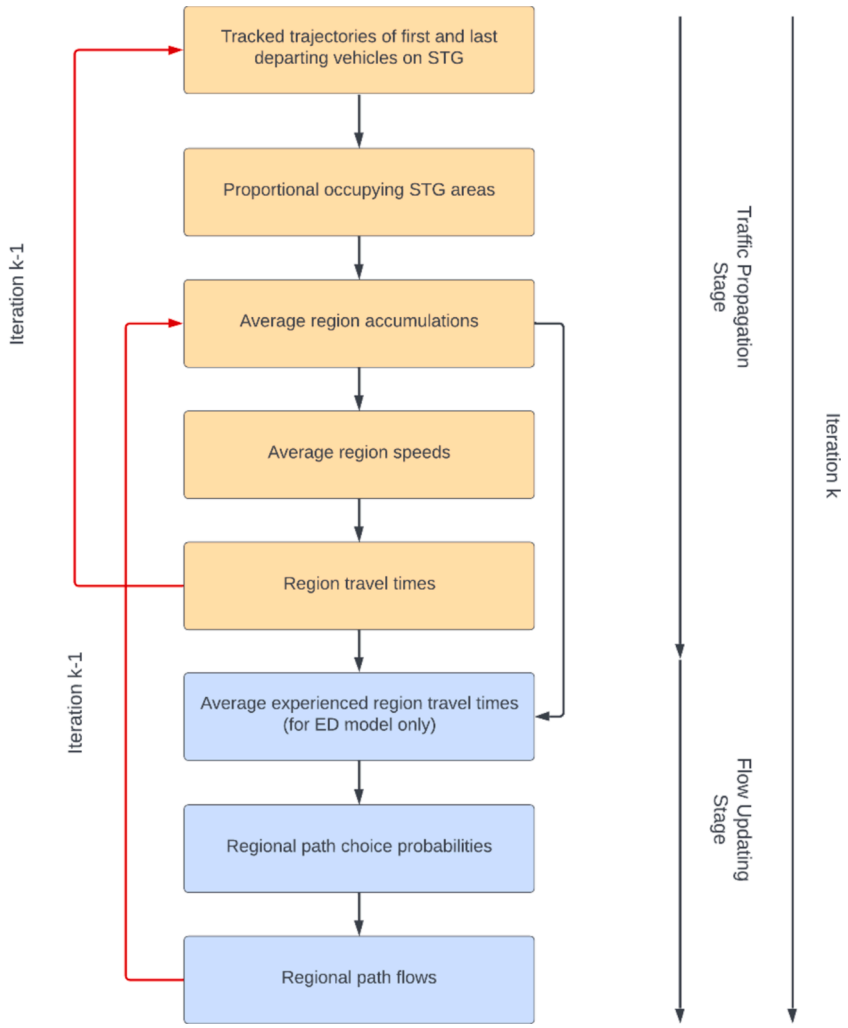

Fig. 9. Schematic diagram illustrating the proposed solution method for solving ID & ED MR-MFD-SUE.

embedded within another fixed-point problem. This gives rise in our algorithm to an inner-loop involving r-path region travel times $\boldsymbol{t}$, and an outer-loop involving the r-path flows $\boldsymbol{f}$. As shown in Algorithm 1 and Fig. 9, there is thus a Traffic Propagation Stage to update the r-path region travel times given the current r-path flows, and then a Flow Updating Stage to update r-path flows given the updated r-path region travel times from the traffic propagation. One solution method could be to fully solve at every outer iteration the inner traffic propagation fixed-point problem in (4) for each set of updated r-path flows. For example, in the schematic diagram in Fig. 9, at master iteration k one could perform a series of inner-loops between tracking trajectories of first departing vehicles and computing region travel times, for fixed r-path flows. However, tracking vehicle trajectories is the most computation time consuming part, and thus in the method we propose we try to minimise this. As illustrated in Fig. 9, we instead propose that, at each master iteration k, just one loop / run-through of the traffic propagation steps is performed updating the region travel times, which feed into updating the r-path flows.

Note that Algorithm 1 does not propose solving ID/ED MR-MFD-SUE with a rolling horizon (i.e. sequentially solving one time-slice at a time), as this is not possible to do for the ED model, since the region travel times in succeeding time-slices are required to compute experienced regional path travel times. It is possible, however, for one to solve the ID model with a rolling horizon, and it is an open question whether this would be less complex / more computationally efficient.

Algorithm 1. Pseudo-code for solving ID & ED MR-MFD-SUE.

Step 0: *Initialisation*. Initialise the r-path region travel time vector $\boldsymbol{t}^{(0)}$ and r-path flow vector $\boldsymbol{f}^{(0)}$ for iteration $k = 0$. Set $k = 1$.
For iteration k:

Traffic Propagation Stage

Step 1: *Track trajectories of first departing vehicles*. Given the r-path region travel time vector $\boldsymbol{t}^{(k-1)}$ from iteration $k-1$, for each r-path for each OD movement, track the trajectories of the first vehicle departing at the beginning of each time-slice $\tau \in \Psi$, plus the trajectory of the last vehicle departing at the end of the last departing time-slice in Ψ (see Appendix C.1).

Step 2: *Compute proportional occupying STG areas*. Given the tracked vehicle trajectories in the previous step, calculate the proportional occupying STG areas (see Appendix C.2).

Step 3: *Compute average region accumulations*. Given the r-path region travel time vector $\boldsymbol{t}^{(k-1)}$ and r-path flow vector $\boldsymbol{f}^{(k-1)}$ from iteration $k-1$, and the proportional occupying STG areas computed in the previous step, compute the average contributing accumulations from each r-path flow, and thereby the total average region accumulations (see equations (3) and (2)).

Step 4: *Compute average region speeds*. Given the average region accumulations computed in the previous step, compute the average region speeds (see equation (1)).

Step 5: *Update r-path region travel times*. Given the average region speeds computed in the previous step, update the r-path region travel time vector $\boldsymbol{t}^{(k)}$ for iteration k (see equation (4)).

Flow Updating Stage

Step 6 (for ED model only): *Compute average experienced region travel times*. Given the updated r-path region travel times $\boldsymbol{t}^{(k)}$ for iteration k, and the average region accumulations computed in Step 3, compute the average experienced region travel times (see equation (6)).

Step 7: *Compute r-path choice probabilities*. Given the r-path choice region travel times ($\boldsymbol{t}^{(k)}$ for the ID model and $\bar{\boldsymbol{t}}(\boldsymbol{t}^{(k)})$ for the ED model), compute the r-path choice probabilities (see e.g., equations (12) and (13)).

Step 8: *Update r-path flows*. Given the r-path choice probabilities computed in the previous step, compute auxiliary r-path flows and perform some averaging scheme to update the r-path flow vector $\boldsymbol{f}^{(k)}$ for iteration k.

Step 9: *Check for convergence*. If convergence criteria are met (see e.g., equations (8) and (9)), stop. Otherwise, set $k = k+1$ and continue to next iteration.

For the experiments in the case study in this paper, we used a Self-Regulated Averaging (SRA) step-size scheme (Liu et al., 2009) for the flow-averaging step (Step 8). The SRA is designed to significantly speed-up the convergence of the Method of Successive Averages and has been shown to perform well for link-network traffic equilibrium in e.g., Yang et al. (2013), Xu & Chen (2013), Kitthamkesorn & Chen (2013, 2014), Chen et al. (2014), Yao et al. (2014). The SRA updates the step-size in each iteration according to the development of the 'residual error' (the difference between the current flow vector and the auxiliary flow vector) across the current and previous iteration. The SRA step-size η_s at iteration s is defined as:

$$\eta_s = \frac{1}{\upsilon_s},\ \upsilon_s = \begin{cases} \upsilon_{s-1} + g_1 & \text{if} \|\boldsymbol{f}^{(s-1)} - \bar{\boldsymbol{f}}^{(s)}\| \geq \|\boldsymbol{f}^{(s-2)} - \bar{\boldsymbol{f}}^{(s-1)}\| \\ \upsilon_{s-1} + g_2 & \text{otherwise} \end{cases},$$

where $g_1 > 1$ and $0 < g_2 < 1$. For the numerical experiments throughout this paper, we set $g_1 = 1.9$ and $g_2 = 0.01$.

To measure convergence of Algorithm 1, one is required to measure both the convergence of the r-path flows $\boldsymbol{f}^{(k)}$ as well as the r-path region travel times $\boldsymbol{t}^{(k)}$. Although other convergence measures were considered, such as a SUE version of the Gap measure in Sbayti et al. (2007) and Batista & Leclercq (2019), for the experiments in this paper, we have chosen to adopt a Root Mean Squared Error (RMSE) measure, which has been regularly adopted to measure convergence in numerous link-network SUE studies (see e.g., Zhou et al. (2012), Kitthamkesorn & Chen (2014), Duncan et al. (2023), Rasmussen et al. (2024)). Moreover, in order to compare convergence between the two fixed-point variables, and ensure they are both equally converged, we adopted a Normalised RMSE measure.

For measuring convergence of the regional path flows, we measure the NRMSE between the final r-path flows and auxiliary r-path flows at iteration s of Algorithm 1:

$$NRMSE_{flow}^{(s)} = \frac{\sqrt{\frac{1}{N}\sum_{m\in M}\sum_{p\in P_m}\left(f_{m,p}^{(s)} - \bar{f}_{m,p}^{(s)}\right)^2}}{\hat{f}^{(s)}}, \tag{8}$$

where $f_{m,p}^{(s)}$ and $\bar{f}_{m,p}^{(s)}$ are the final r-path flow and auxiliary r-path flow, respectively, for r-path $p \in P_m$ at iteration s, N is the total number of r-paths, and $\hat{f}^{(s)}$ is the average r-path flow value at iteration s. Note that since this NRMSE measure is based on the difference between the current regional path flows and the auxiliary regional path flows (not the previous iteration flows), the NRMSE measure is a gap measure that provides a quality indicator of how far the current network conditions are from the SUE conditions.

For measuring convergence of the r-path region travel times, we measure the NRMSE between the iteration s and iteration $s-1$ r-path region travel times:

Fig. 10. Area of case study.

$$NRMSE_{tt}^{(s)} = \frac{\sqrt{\frac{1}{N_{reg}}\sum_{m\in M}\sum_{p\in P_m}\sum_{r\in R_{m,p}}\left(t_{m,p,r}^{(s)} - t_{m,p,r}^{(s-1)}\right)^2}}{\widehat{t}^{(s)}}, \tag{9}$$

where $t_{m,p,r}^{(s)}$ is the travel time of region r travelling r-path $p \in P_m$ at iteration s, $N_{reg} = \sum_{m\in M}\sum_{p\in P_m}\sum_{r\in R_{m,p}} 1$ is the total number of region travel times, and $\widehat{t}^{(s)}$ is the average region travel time at iteration s.

The r-path flows and region travel times are said to have converged sufficiently if $NRMSE_{flow}^{(n)} < 10^{-\zeta_1}$ and $NRMSE_{tt}^{(n)} < 10^{-\zeta_2}$, where ζ_1 and ζ_2 are predetermined convergence parameters. For all experiments, we set $\zeta_1 = \zeta_2 = 2$, which we found to provide reasonable levels of convergence.

For the numerical experiments in this paper, Algorithm 1 was implemented in Python. The code can be made available upon

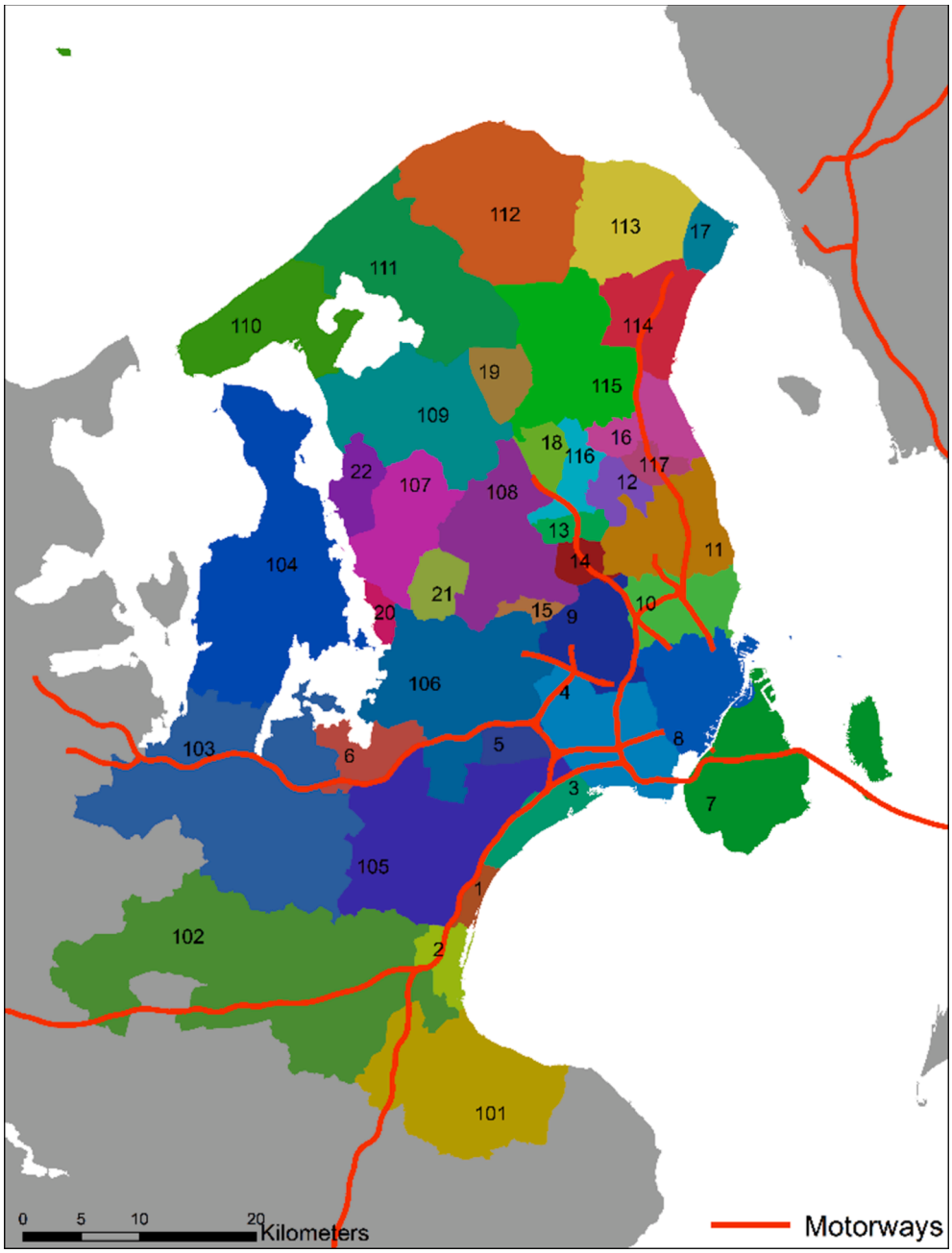

Fig. 11. Underlying region partitioning and superimposed motorway network.

request.

5. Set-up of case study multi-region MFD system

In this section, we shall discuss the set-up of the multi-region MFD system in our large-scale case study of Zealand, Denmark and detail how we calibrated the speed-MFD functions.

5.1. Region partitioning

The first thing to note is that the case study area is much larger than any studied so far. To the best of our knowledge the city of Lyon studied in Mariotte et al. (2020) has been the largest case study with a maximum of 10 regions, all of which are within the city urban area. As depicted in Fig. 10, the area of Zealand in our case study is much larger, consisting of urban area cities/towns of e.g., Copenhagen, Roskilde, Hillerød, and Helsingør, as well as rural areas between the cities/towns. There is also a motorway network superimposed upon the rural and urban areas, as well as external entry/exit points (port zones) to the area, for example the Helsingør ferry to Sweden and connections to other parts of Denmark. Previous works have all been concerned with single urban areas, where the motorways are considered as part of the urban MFD. A key feature of the multi-region MFD setup in this case study is that there are underlying urban and rural regions and superimposed motorway regions that are considered separately. Traffic conditions on the motorway have the potential to be considerably different to the conditions in surrounding areas, particularly in rural areas, and so we deemed it prudent to consider the motorways separately.

Inspired by how Mariotte et al. (2020) partitioned Lyon into regions, we also partitioned our underlying regions through a trial-and-error approach aiming to satisfy a set of features. Similar to as done in Mariotte et al. (2020), each underlying region was partitioned by grouping together several neighbouring administrative zones, obtained from the Danish national model (called GMM zones (Rich & Hansen, 2016)). There were 269 GMM zones, which were grouped together initially using logic and local understanding, using for example natural borders from the network topology (e.g., bodies of water), and aiming to aggregate areas of homogeneous traffic conditions (e.g., separating known urban and rural areas). We also aimed to maintain as compact shapes as possible, but in some cases the topology of the administrative zones made this difficult. This is less of a problem in our study though as we do not assume a region can only be traversed once when travelling a regional path. After the initial region partitioning, we then refined the zone groupings through trial-and-error aiming to lower the scatter of the MFDs (see Section 5.2). Due the large span of the study area where there are different urban areas connected by rural areas, it was necessary to partition the area into a large number of underlying regions to best capture areas of homogeneous traffic conditions. Fig. 11 displays the final underlying region partitioning, where there were 39 regions in total.

For the motorway regions, given that a large proportion of traffic travels on motorways, we deemed it advantageous to partition the motorway network fairly disaggregately, aiming to capture traffic propagation/homogeneity in a more detailed manner. We began by partitioning superimposed motorway regions according to the underlying regions, i.e. using the region borders of the underlying regions to also partition the motorway regions, to improve the consistency and detail of the regional paths. We then partitioned the motorway regions further by direction and at junctions, as it was our intuition that this would better capture traffic homogeneity. The motorway partitioning is exemplified in Fig. 12 for underlying region 4, where there are 8 superimposed motorway regions. This resulted in a total of 96 motorway regions, meaning that there were 135 regions in total.

The motorway regions were partitioned according to direction as, for example, the motorway carriageway heading towards Greater Copenhagen is likely to be more congested in the morning peak, and the reverse in the evening. Moreover, a criticism of multi-region MFD traffic models has been their lack of 'directionality' (Raadsen et al., 2020). Thus, by considering each carriageway of a motorway separately, directionality for the motorway regions is accounted for, where a large proportion of traffic travels. It is our belief that treating the motorways separately, and in a detailed manner, is a uniquely attractive feature of this case study. We could, however, have partitioned the motorway regions less disaggregately, or not at all, to simplify the multi-region system, and one may do this if one wishes for a simpler system, but we believe the partitioning to be at a suitably detailed level.

Note that in this study the motorway regions are treated like any other region in the dynamic multi-region MFD SUE model. The only difference is that a different speed-MFD functional form is fitted for the motorway regions to capture the different speed reduction properties (see the following section). If one wishes, one could model the traffic propagation along the motorway regions differently, for example through a point queue model as done by Wang & Gayah (2021) or an asymmetrical cell transition model (Haddad et al., 2013).

5.2. Speed-MFD functions

In this section we detail how the speed-MFD functions were calibrated for each region. The proposed D-MR-MFD-SUE model operates solely with the speed-MFD function, i.e. the production-MFD functions are implicit but not utilised, and thus our focus was on calibrating speed-MFD functions. These are calibrated using a combination of probe vehicle data and vehicle count data, the latter being used to estimate the penetration rate of the probe vehicles.

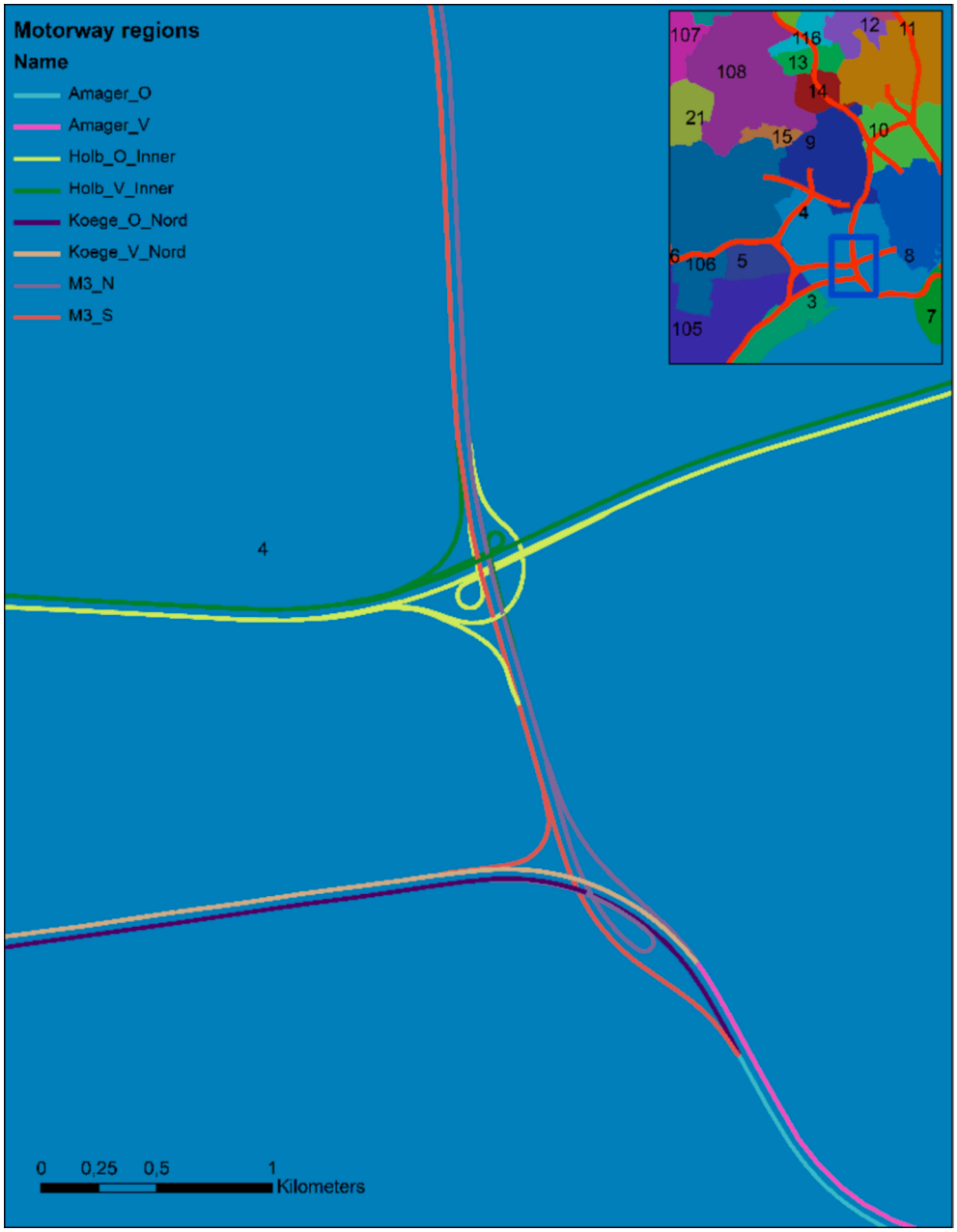

Fig. 12. Example of superimposed motorway region partitioning.

For each region $r \in R$, a speed-MFD functional form (see further below) was fitted to a set of accumulation-speed datapoints K_r. Each datapoint $\kappa \in K_r$ corresponds to a different 15-minute time-period[6] during the month of August 2021. The datapoint (n_r^κ, v_r^κ) consists of n_r^κ: the average accumulation in region r during time-period κ, and v_r^κ: the average speed of vehicles in region r during time-period κ. To obtain these datapoints, two datasets were used. The first dataset consisted of link-map-matched GPS points of cars obtained from COWI Ltd (https://www.cowi.dk) throughout August 2021. COWI Ltd continuously collect real-time information from cars in Denmark, and the fleet-size is very large (August 2021: 200,000 + vehicles in Denmark). The second dataset consisted of loop detector vehicle counts collected by the Danish road directorate (https://mastra.vd.dk).

Motivated by how Mariotte et al. (2020) calculated average speed in their calibration of MFD functions (see equation (17) in that

[6] It is important to note that these time-periods of aggregate accumulation/speed in a region used for calibrating the speed-MFD functions do not correspond in any way to the 'time-slices' in which the discrete-time dynamic traffic model operates with.

paper), the observed average speed in region r during time-period $\kappa \in \mathrm{K}_r$ was calculated in this study as follows:

$$v_r^\kappa = \frac{TDT_r^\kappa}{TTT_r^\kappa} = \frac{\sum_{y \in Y_r^\kappa} D_{r,y}^\kappa}{\sum_{y \in Y_r^\kappa} T_{r,y}^\kappa},$$

where TDT_r^κ and TTT_r^κ are the total distance travelled (in [veh.kms]) and total time travelled (in [veh.hrs]) by the GPS units in region r during time-period κ, Y_r^κ is the set of GPS units that were observed travelling in region r at any moment during time-period κ, $D_{r,y}^\kappa$ is the distance travelled by GPS unit $y \in Y_r^\kappa$ in region r during time-period κ, and $T_{r,y}^\kappa$ is the time travelled by GPS unit $y \in Y_r^\kappa$ in region r during time-period κ.

Motivated by how Du et al. (2016) calculated average density of vehicles in their calibration of MFD functions (see equation (4) in that paper), the observed average accumulation in region r during time-period $\kappa \in \mathrm{K}_r$, imputed by growthing up observed GPS data by a penetration rate, was calculated in this study as follows:

$$n_r^\kappa = \frac{TTT_r^\kappa}{\delta \bullet \Gamma},$$

where TTT_r^κ is the total time travelled in region r during time period κ by the GPS units in [veh.hrs], δ is the time-period duration equal to 0.25 [hrs], and Γ is a unitless penetration rate. The penetration rate was obtained by comparing the vehicle count from loop detector data to the vehicle count from GPS data in corresponding locations over corresponding time-periods. Fig. 13 displays the locations of the loop detectors, 2077 in total, including separate locations for each direction of the carriageway. In order to avoid the sensitivity in penetration rate that comes from comparing small counts (e.g., if compared over 15-minute intervals), we compared total counts over the course of a day, for each of the 31 days of August 2021. Counts were only compared when at least 1000 loop detector counts were observed at the location during that day. Fig. 14 displays the distribution of the individual penetration rates. As one can see, the distribution is right-skewed. We thus chose to use the median penetration rate, which was $\Gamma = 0.0384$.

Before fitting the speed-MFD functions, the accumulation-speed datapoints were cleaned to remove noise. The datapoints were partitioned into 20 bins according to accumulation. For each bin with more than 10 datapoints, the mean speed and standard deviation of the datapoints were obtained. All datapoints with speed greater than 1.96 times the standard deviation away from the mean were removed. Fig. 15 demonstrates the cleaning of the accumulation-speed datapoints.

Upon inspection of the accumulation-speed datapoints for each region, the underlying urban/rural regions were observed to have different trends to the motorway regions. For both the underlying and motorway regions, we experimented with different fundamental diagram functional forms, such as the 'linear' function (Greenshields et al., 1935), the 'Smulders' function (Smulders, 1990), the 'de Romph' function (de Romph, 1994), and different 'exponential and power' functions (del Castillo, 2012; Kessels, 2019).

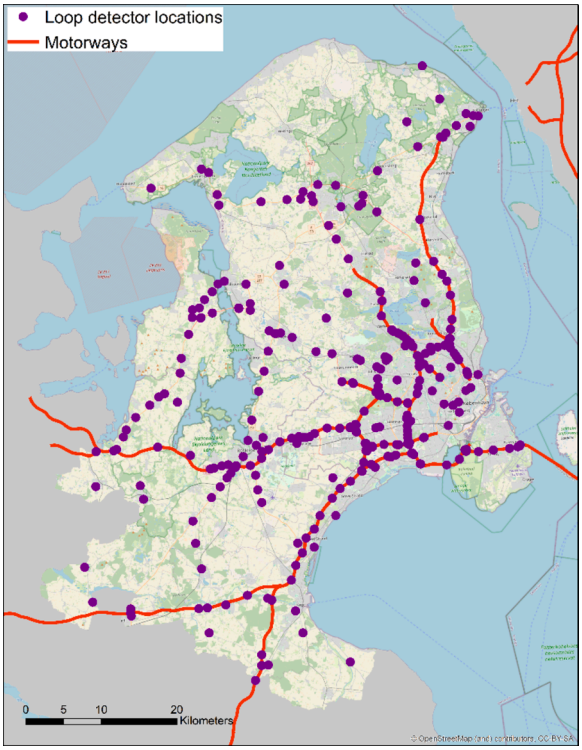

Fig. 13. Locations of the loop detectors.

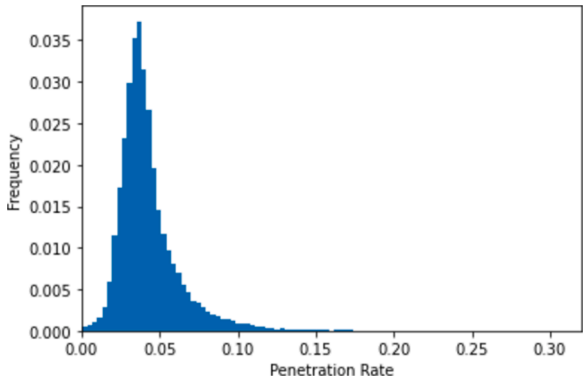

Fig. 14. Distribution of the individual penetration rates from each location/day.

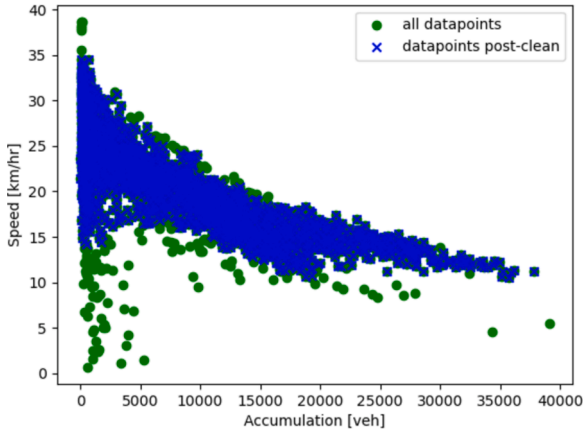

Fig. 15. Example of cleaning of accumulation-speed datapoints.

For the underlying urban/rural regions, we decided to fit an exponential functional form. This is as follows for an accumulation state n_r:

$$v_r(n_r) = (a-h)e^{-bn_r} + h,$$

where $a > 0$ gives the free-flow region speed, $b > 0$ determines the curve of the speed function, and h is the minimum speed. These function parameters were fitted to accumulation-speed datapoints through non-linear least squares regression, via the scipy.optimize.curve_fit package in Python. For regions where h could not be well-fitted by the datapoints, we set the minimum speed to $h = 5$ ([km/hr]) as this appeared to give the best fit overall. As examples, Fig. 16 plots the (cleaned) accumulation-speed datapoints for regions 8, 6, 7, and 117 (i.e. the areas of Greater Copenhagen, Roskilde, Amager, and to the north of DTU, respectively), and the fitted speed-MFD functions. As shown, the trend of the datapoints is that speed decreases as accumulation increases. There appears generally to be no systematic bias in the residuals, i.e. there is generally scatter above and below the fitted curve.

For the motorway regions, we decided to fit a piecewise-exponential speed-MFD functional form. This is as follows for an accumulation state n_r:

$$v_r(n_r) = \begin{cases} (a-h)e^{-bn_r} + h & if\ n_r \le n_r^{crit} \\ (a-h)e^{-bn_r^{crit}} e^{-c\left(n_r - n_r^{crit}\right)} + h & if\ n_r > n_r^{crit} \end{cases},$$

where $a > 0$ gives the free-flow region speed, $n_r^{crit} > 0$ is the critical accumulation, $b > 0$ and $c > 0$ determine the curves of the speed function pre- and post-critical accumulation, respectively, and h is the minimum speed. These function parameters were also fitted to accumulation-speed datapoints through non-linear least squares regression, via the scipy.optimize.curve_fit and numpy.piecewise packages in Python. For regions where h could not be well-fitted by the datapoints, we set the minimum speed to $h = 10$ ([km/hr]) for these motorway regions. As examples, Fig. 17A-D plots the accumulation-speed MFD datapoints for four motorway regions and the fitted speed-MFD functions. As shown, the trend of the datapoints is that speed decreases steadily as accumulation increases, up until a point where there is a sudden decrease in speed which then plateaus out. Again, there appears to be no systematic bias in the residuals.

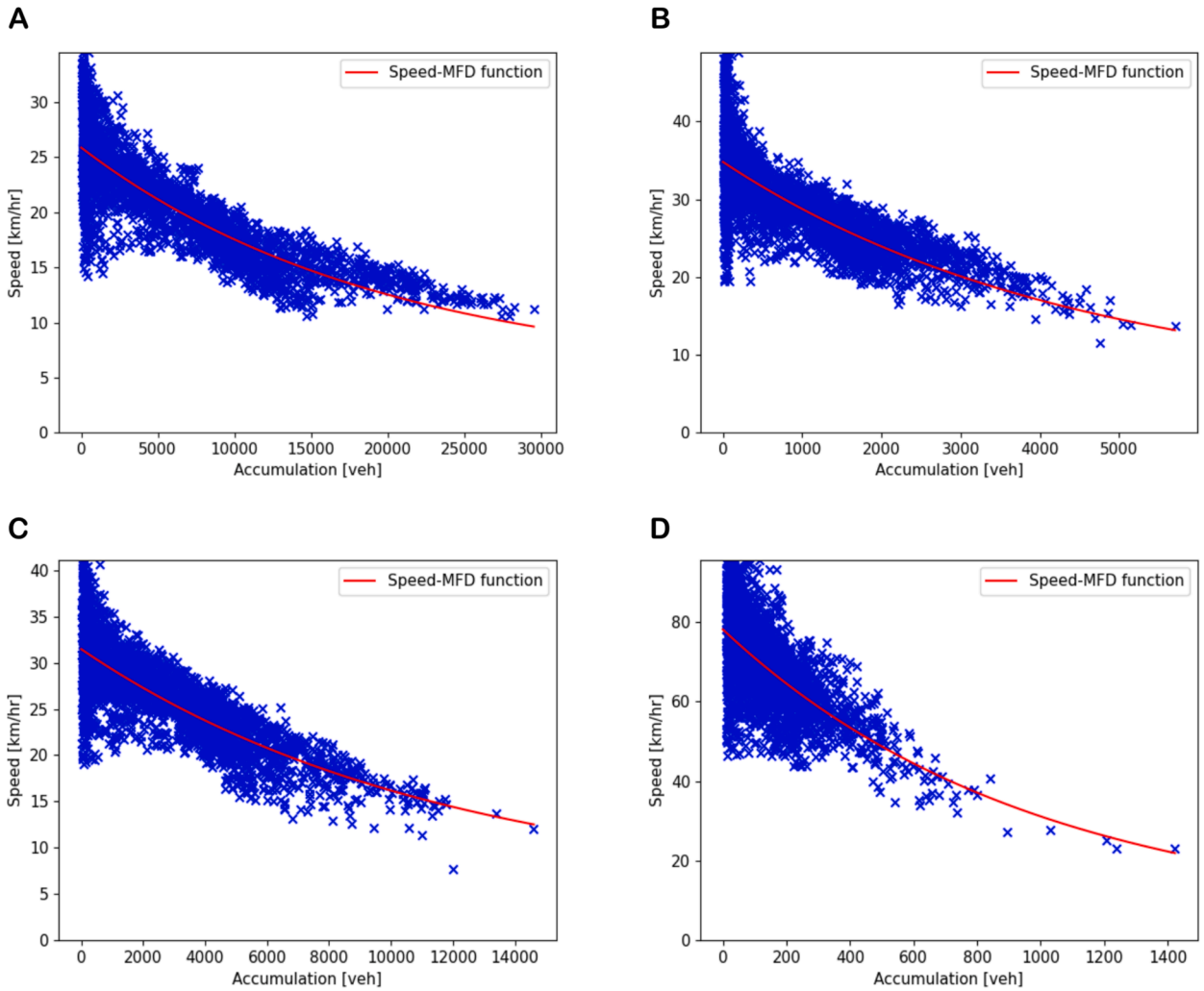

Fig. 16. Examples of four fitted exponential speed-MFD functions. **A**: Region 8 – Greater Copenhagen. **B**: Region 6 – Roskilde. **C**: Region 7 – Amager. **D**: Region 117 – Rural area north of DTU.

5.3. Regional OD movements and travel demand

As described in Section 5.1, the underlying regions in this case study were partitioned by grouping together several GMM zones. As depicted in Fig. 10, there are also external entry/exit points to the study area at external region borders. These are termed port zones, which are each treated as a separate zone (in addition to the LTM zones). Travel demands for the zone-zone OD movements were obtained from a calibrated disaggregate traffic model (Rasmussen et al., 2021), which gives demands for 10 Time of Day (TOD) periods, given with their time of day covered in Table 1. As can be seen, the finest granularity we have available is 1 h. Note that not every zone-zone OD movement has travel demand.

As described in Section 2, each pair of origin and destination regions may have multiple regional OD movements, depending on whether there are any external entry/exit points. In this case study, the set of regional OD movements M was identified as follows:

> Set the initial set of regional OD movements as $M = \varnothing$.

> For each pair of origin and destination regions r^O and r^D:

> Check whether any non-port-zone zone in r^O has a non-zero demand at any TOD period to a non-port-zone zone in r^D. If so, add $(r^O, r^D, 0, 0)$ to M.

> If r^O has an external origin, check whether any of the port zones in r^O have a non-zero demand at any TOD period to any non-port-zone zone in r^D. If so, add $(r^O, r^D, 1, 0)$ to M.

> If r^D has an external destination, check whether any non-port-zone zone in r^O has a non-zero demand at any TOD period to any of the port zones in r^D. If so, add $(r^O, r^D, 0, 1)$ to M.

> If r^O has an external origin and r^D has an external destination, check whether any of the port zones in r^O have a non-zero demand

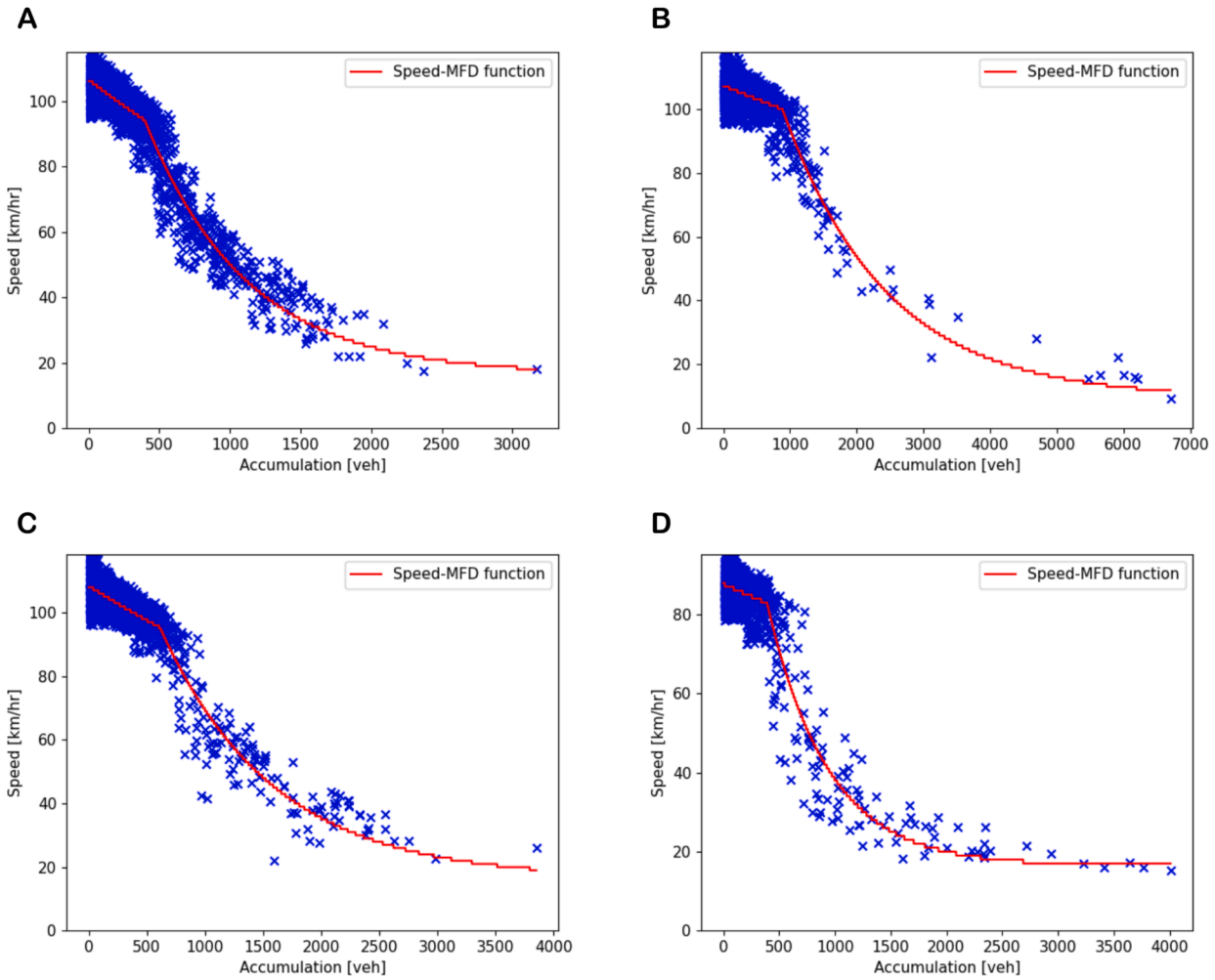

Fig. 17. Examples of four fitted piecewise-exponential speed-MFD functions. **A**: Region 10 motorway 'M3_N'. **B**: Region 11 motorway 'Hels_N'. **C**: Region 4 motorway 'M3_N'. **D**: Region 10 motorway 'Hels_S'.

at any TOD period to any of the port zones in r^D. If so, add $(r^O, r^D, 1, 1)$ to M.

The result of the above was that there were in total 1898 regional OD movements, which are fixed across time, but not always with travel demand across the day.

As noted above, the zone-zone travel demands were obtained for 10 different TOD periods. In this paper we implement the discrete-time dynamic multi-region MFD SUE model with time-slice durations of 1-hour, 30-minutes, and 15-minutes. For each of these time-slice grains, the zone-zone travel demands for each time-slice were obtained by splitting up the demand for the associated TOD period. For example, the demand for 30-minute time-slice 8:30–9:00am was obtained by halving the demand for the 8-9am TOD period. The travel demand d_m^τ for regional OD movement $m \in M$ departing during time-slice τ, was thus obtained by summing up the time-slice τ travel demands from the zone-zone OD movements associated with regional OD movement m. Fig. 18 plots the total travel demand across the OD movements at each hour of the day, i.e. hour of the day 5 corresponds to 04:00–05:00. As shown, there is a morning demand peak and an afternoon demand peak, as one would expect.

5.4. Regional path choice sets and regional trip lengths

The D-MR-MFD-SUE model developed in this paper requires that the regional path choice sets and regional trip lengths (distances travelled through a region) are fixed as inputs to the system, obtained in pre-processing. In this study we assume that both the regional path choice sets and regional trip lengths are constant across time. To generate them we adopted a similar approach to Yildirimoglu & Geroliminis (2014). Shortest path searches were conducted between zone-zone OD movements on the underlying link-network, based on different link travel costs, to identify a set of link-routes for each regional OD movement. Then, by tracing along each link-route to determine the order of regions the link-route travels through, the regional path of each link-route was obtained. The lengths of the links were used to determine the regional trip lengths of each region in each regional path. Then, to obtain reasonably-sized regional path

Table 1
TOD covered by each TOD period.

TOD Period	1	2	3	4	5	6	7	8	9	10
TOD Covered	21:00–05:00	05:00–06:00	06:00–07:00	07:00–08:00	08:00–09:00	09:00–15:00	15:00–16:00	16:00–17:00	17:00–18:00	18:00–21:00

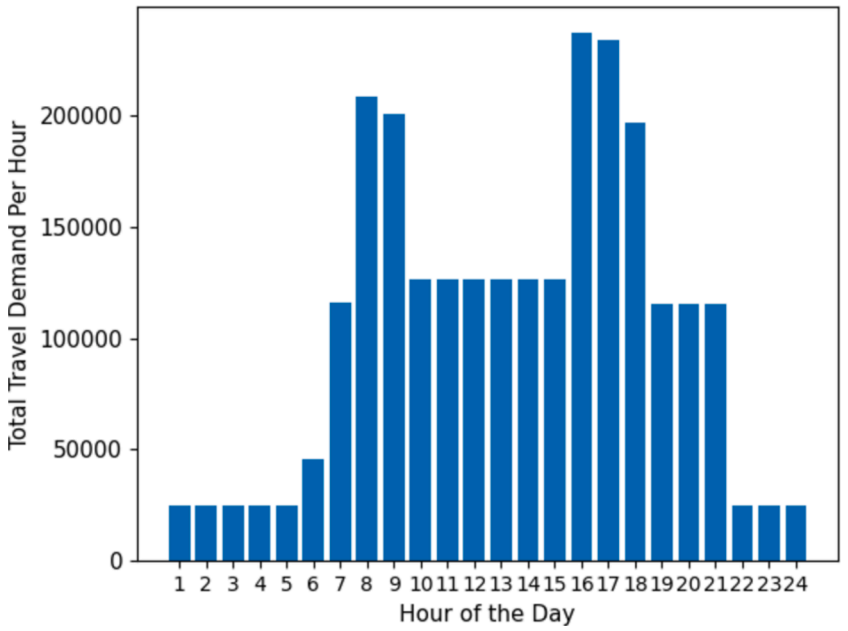

Fig. 18. Total travel demand across regional OD movements at each hour of the day.

choice sets, the choice sets were trimmed, in a manner maximising the variation in r-paths. The entire process is outlined in Algorithm 2 and yielded a total of 29,873 regional paths.

Algorithm 2. Process for generating regional paths and determining regional trip lengths.

Step 1: *Conduct shortest path searches based on link length.*
- **Step 1.1**: For regional OD movements with less than 100 zone-zone OD movements, conduct a shortest path search for each zone-zone OD movement based on link length.
- **Step 1.2**: For regional OD movements with more than 100 zone-zone OD movements, randomly draw 100 zone-zone OD movements from the set and conduct shortest path searches based on link length.

Step 2: *Conduct shortest path searches based on link free-flow travel time.*
- **Step 2.1**: For regional OD movements with less than 100 zone-zone OD movements, conduct a shortest path search for each zone-zone OD movement based on link free-flow travel time.
- **Step 2.2**: For regional OD movements with more than 100 zone-zone OD movements, randomly draw 100 zone-zone OD movements from the set and conduct shortest path searches based on link free-flow travel time.

Step 3: *Conduct shortest path searches based on randomly perturbed link free-flow travel time.*
- **Step 3.1**: Stochastically draw 20 settings of the link travel times, by randomly perturbing free-flow travel time as follows for link a: $tt_a = fftt_a + \xi_a$, where ξ_a is a random variable assuming an exponential distribution with scale (mean / standard deviation) $0.3 \bullet fftt_a$.
- **Step 3.2**: For each of the 20 settings of randomly perturbed link free-flow travel times: For all regional OD movements, randomly draw 100 zone-zone OD movements and conduct shortest path searches.

Step 4: *Determine regional paths and regional trip lengths.*
- **Step 4.1**: For each regional OD movement, determine the regional path choice set by tracing through each generated link-route to identify corresponding regional paths, and then identifying the set of unique regional paths. Concurrently, using the link lengths, determine the regional trip lengths of each region in each regional path of each link-route. Regional trip lengths from different link-routes leading to the same regional path are averaged to obtain the typical/average regional trip lengths of each regional path.

Step 5: *Trim regional path choice sets.*
- **Step 5.1**: For regional OD movements with more than 20 regional paths, repeat the following 200 times:
  - **Step 5.1.1**: Randomly draw 20 regional paths.
  - **Step 5.1.2**: Calculate the overlap in regional trip length between each pair of regional paths i,j:

$$overlap_{i,j} = \frac{\sum_{r \in R_i \cap R_j} \min(l_{i,r}, l_{j,r})}{\sqrt{\sum_{r \in R_i} l_{i,r}} \bullet \sqrt{\sum_{r \in R_j} l_{j,r}}}.$$

  - **Step 5.1.3**: Compute average overlap between regional paths for that OD movement.
- **Step 5.2**: For each regional OD movement, from the 200 sampled regional path choice sets, select the choice set with the lowest average overlap.

6. Estimation of model parameters

In this section, we provide a MLE procedure for consistently estimating parameters or regional path choice models within the ID & ED models, with tracked r-path observations. This procedure is then used to estimate model parameters in the real-life case study.

Before we proceed, however, we shall first discuss why we believe it is important to treat regional path choice with stochasticity, and thus, since stochastic choice models have parameters, why it is important that these are estimated. We begin by establishing what we interpret regional path choice to represent. From a true origin in the origin region to a true destination in the destination region, there is a choice set of link-routes on the actual network a driver may take. For a given region partitioning of the area, with each node of the network assigned to a region, each link-route has an associated regional path from origin region to destination region. Although drivers' actual decisions are between link-routes based on link-route travel costs, by aggregating the costs of the set of link-routes associated with each regional path, one can approximate a cost for travelling each regional path, and thus predict how drivers will distribute themselves between the regional paths based on these costs. Therefore, while regional paths are not physical, and drivers do not cognitively choose between regional paths, regional path choice aims to aggregately capture actual link-route decisions.

Now, most existing multi-region MFD traffic equilibrium models adopt a DUE model for the traffic equilibrium (see Section 1), neglecting any stochasticity. There are numerous reasons, however, why we believe regional path choice should be treated with stochasticity. There are the usual choice modelling reasons, for example: i) not every driver may have perfect knowledge of the link-route travel costs (and thereby the aggregate regional path costs), ii) there may be some attributes motivating link-route choice (and thereby regional path choice) not captured by the modeller, iii) there may be some heterogeneity in the preferences of drivers. And, there are reasons attributed to how actual link-route choices are represented as aggregate regional path choices, such as uncertainties in the determination of regional path costs from aggregating associated link-route costs (e.g., average, minimum, or median cost), and uncertainties in the partitioning of regions which affects the composition of the regional paths.

Thus, assuming that there is some stochasticity in the regional path choice, and assuming random utility theory, the regional path travel costs have random error terms. By making an assumption on the distribution of these error terms, one obtains the stochastic regional path choice model, which will have model parameters requiring to be fitted data. In Section 6.2.2 we shall discuss, for the case study, which distribution we assume for the error terms, the regional path choice model this forms, what we interpret the model parameters to be capturing, and why it is important these parameters are estimated.

6.1. Likelihood formulation and estimation procedure

Suppose that the details of the multi-region MFD system are known, i.e. the region partitioning, speed-MFD functions, regional OD movements, regional OD travel demands, regional path choice sets, and regional trip lengths are all known. Suppose that we have available a set of Z observed regional paths, where the observation data is contained in a vector $\boldsymbol{y}$ of size Z where element z of $\boldsymbol{y}$ details the OD movement, regional path taken, and departing time-slice of the observation.

The Likelihood, L, for an observation data vector $\boldsymbol{y}$ is:

$$L(\boldsymbol{\psi}|\boldsymbol{y}) = \prod_{\tau\in\Psi}\prod_{m\in M}\prod_{p\in P_m}\left(Q^{\tau}_{m,p}(\boldsymbol{f}^{*}(\boldsymbol{\psi}))\right)^{\phi^{\tau}_{m,p}(\boldsymbol{y})} = \prod_{\tau\in\Psi}\prod_{m\in M}\prod_{p\in P_m}\left(\frac{f^{\tau,*}_{m,p}(\boldsymbol{\psi})}{d^{\tau}_{m}}\right)^{\phi^{\tau}_{m,p}(\boldsymbol{y})}, \tag{10}$$

where $\boldsymbol{\psi}$ is the vector of model parameters, $\phi^{\tau}_{m,p}(\boldsymbol{y})$ is the number of observations that take r-path $p \in P_m$ of OD movement m when departing during time-slice τ, $\boldsymbol{f}^{*}(\boldsymbol{\psi})$ is the ID/ED MR-MFD-SUE r-path flow solution given $\boldsymbol{\psi}$, and $Q^{\tau}_{m,p}(\boldsymbol{f}^{*}(\boldsymbol{\psi}))$ is the choice probability for r-path $p \in P_m$ when departing at time-slice τ given $\boldsymbol{f}^{*}$ given $\boldsymbol{\psi}$. As shown in the first part of (10), for a given setting of the parameters, ID/ED MR-MFD-SUE is solved, and the Likelihood is a function of the r-path choice probabilities given the ID/ED MR-MFD-SUE solution. The second part of (10) is derived from the fact that at equilibrium the r-path choice probabilities and route flow proportions are equal.

The Log-Likelihood function, LL, to be maximised is:

$$LL(\boldsymbol{\psi}|\boldsymbol{y}) = \ln\left(\prod_{\tau\in\Psi}\prod_{m\in M}\prod_{p\in P_m}\left(\frac{f^{\tau,*}_{m,p}(\boldsymbol{\psi})}{d^{\tau}_{m}}\right)^{\phi^{\tau}_{m,p}(\boldsymbol{y})}\right) = \sum_{\tau\in\Psi}\sum_{m\in M}\sum_{p\in P_m}\phi^{\tau}_{m,p}(\boldsymbol{y})\ln\left(\frac{f^{\tau,*}_{m,p}(\boldsymbol{\psi})}{d^{\tau}_{m}}\right), \tag{11}$$

where $f^{\tau,*}_{m,p}(\boldsymbol{\psi})$ is the ID/ED MR-MFD-SUE r-path flow solution for r-path $p \in P_m$ when departing at time-slice τ given the vector of model parameters $\boldsymbol{\psi}$.

Standard MLE procedures can be used to estimate the parameters of underlying regional path choice models within ID/ED MR-MFD-SUE for a given multi-region MFD system. Using a standard iterative estimation procedure, model parameters can be found that maximise the Log-Likelihood function as formulated in (11) above for a given set of data. The key difference from usual MLE procedures is the re-solving of ID/ED MR-MFD-SUE for every parameter setting tested, to ensure consistency, meaning that we are effectively solving a bi-level optimisation or mathematical problem with equilibrium constraints. Algorithm 3 outlines pseudo-code for

the estimation procedure.

Algorithm 3: Pseudo-code for estimating parameters of underlying regional path choice models within ID/ED MR-MFD-SUE.

Step 1: Initialisation. Define an initial set of parameter values $\boldsymbol{\psi}^{(1)}$ for MLE, and set $k = 1$.

Step 2: Re-solve ID/ED MR-MFD-SUE and compute LL. Given the set of parameter values $\boldsymbol{\psi}^{(k)}$ for iteration k, re-solve ID/ED MR-MFD-SUE according to the relevant r-path choice model. Given the equilibrated r-path choice probabilities / flows, calculate the Log-Likelihood $LL^{(k)}(\boldsymbol{\psi}^{(k)}|\boldsymbol{y})$ as in (11) for iteration k.

Step 3: Compute new set of parameters. Based on $LL^{(s)}$ and the associated parameters $\boldsymbol{\psi}^{(s)}$ for all $s \leq k$, compute a new set of parameters $\boldsymbol{\psi}^{(k+1)}$ to test in the following iteration.

Step 4: Stopping criteria. If $\left|LL^{(k)} - LL^{(k-1)}\right| < \zeta$ stop. Otherwise, set $k = k+1$ and return to Step 2.

In general, Step 3 could apply procedures from standard numerical optimisation methods to identify the parameters to evaluate in the next iteration. For the experiments in this paper, we utilised the L-BFGS-B bound-constraint, quasi-Newton minimisation algorithm (Byrd et al., 1995) for Steps 2–4 of Algorithm 3 (where we minimise $-LL$).

Although not reported here, the above estimation procedure was tested in simulation estimation experiments (following a similar process as conducted in Duncan et al. (2020,2021)), where it was tested whether assumed true parameters could be reproduced. After a series of different experiments, with different settings of the assumed true parameters, it was found that these parameters could generally be reproduced, with no evidence of bias. Moreover, unique solutions were always found, regardless of the initial conditions. This validated the procedure for successfully estimating parameters of underlying regional path choice models within ID/ED MR-MFD-SUE.

6.2. Case study

6.2.1. Observed regional path data

The tracked regional path observation data in the case study was obtained from GPS trajectories also from COWI Ltd (https://www.cowi.dk). GPS trajectories were collected for the entire of August 2021, but, aiming to capture typical weekday traffic conditions, we discarded data for weekends and during the first week of August as there was little traffic post summer holiday. We discarded the following observations: i) observations originating and destinating in the same underlying region, ii) observations originating and destinating in adjacent underlying regions, and iii) observations less than 10 km. The aim of these data processing steps was to select observations in which there is sufficient variation in the attributes of the alternatives, and to exclude observations where the origin/destination region travel costs are a large proportion of the total regional path costs. This is especially relevant when basing regional path choice on regional path travel costs excluding origin/destination region costs (see Section 6.2.3 below).

Each trajectory provided a sequence of GPS coordinates and timestamps. By associating GPS coordinates with regions and considering the departing timestamp, an OD movement, regional path, and departing time-slice were associated with each GPS trajectory. If the regional path did not match exactly to any of those generated (see Section 5.4), the trajectory was associated to the generated regional path with the greatest overlap in length (see the overlap measure in Step 5.1.2 in Algorithm 2). Only trajectories with overlap measures greater than 0.8 (i.e. share 80 % of each other's length) were kept. The result was that there were a total of 434,860 observed regional paths. The above information was used to compute the $\phi^{\tau}_{m,p}(\boldsymbol{y})$ values in (11) for all regional paths $p \in P_m$, OD movements $m \in M$, and departing time-slices $\tau \in \Psi$.

A wide range of regional paths were observed for each regional OD movement, i.e. there is plenty of heterogeneity in the data. Fig. 19A plots the distribution of the percentages of regional paths of each OD movement that are used by at least one observation (excluding OD movements with no observations (16 % of ODs)). As shown, there is good coverage, where many OD movements have 100 % coverage, and the average coverage is 55 %. To illustrate the heterogeneity in the data further, Fig. 20 and Fig. 21 display for regional OD movements Helsingør to Amager (17 → 7) and Roskilde to DTU (6 → 11), three example GPS trajectories overlayed upon the regions used by regional paths for that OD.

Fig. 22A displays the distribution of the lengths of the r-path observations. As shown, the share of observations decreases with length, but there are some observations that span great lengths. Fig. 22B displays the distribution of the departing times of the r-path observations. As shown, there are more observations during the peak hours of the day, with the trend resembling the travel demand profile in Fig. 18.

Fig. 23 displays the distribution of the percentage differences between the lengths of the observed regional paths and matched generated regional paths. A positive percentage means the observed r-path length is longer than the matched r-path length. The mean percentage difference is 0.36 % and the standard deviation 14.4 %. This indicates that overall the observed regional paths have been matched well to a generated regional path.

6.2.2. Regional path choice

For the reasons discussed at the beginning of Section 6, we assume that regional path choice has stochasticity, and that this stochasticity is modelled through random utility theory. Like in link-network route choice, the deterministic utility of a regional path is equal to negative regional path travel cost. As discussed at the beginning of Section 6, regional path travel cost is obtained by aggregating the travel costs of a set of link-routes associated with the regional path. Adding random error terms to these travel costs, and assuming these are independently and identically distributed Gumbel, then the consequent regional path choice model is Multinomial Logit (MNL).

Let $C^{\tau}_{m,p}$ be the travel cost of regional path $p \in P_m$ when departing during time-slice τ. The MNL probability of choosing r-path $p \in$

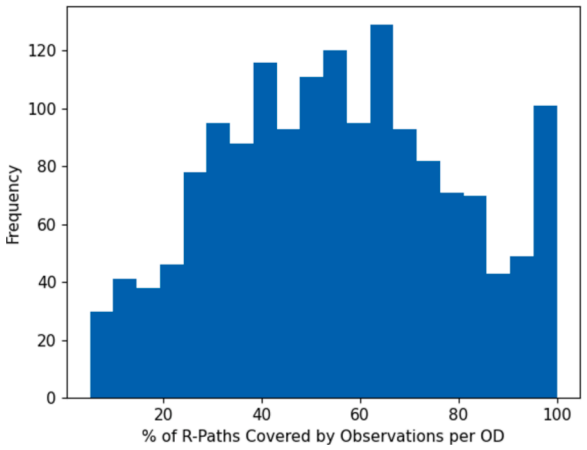

Fig. 19. Distribution of the percentage of regional paths of each OD movement used by at least one observation.

P_m when departing during time-slice τ is:

$$Q^{\tau}_{m,p} = \frac{\exp\left(-\theta C^{\tau}_{m,p}\right)}{\sum_{j \in P_m} \exp\left(-\theta C^{\tau}_{m,j}\right)}, \tag{12}$$

where $\theta > 0$ is the Logit scaling parameter measuring the level of stochasticity, i.e. the extent of the modelling errors / driver knowledge uncertainties. For example, if a low value of θ is estimated, many observed regional paths have large modelled costs, indicating large modelling errors / driver knowledge uncertainties. It is thus important that this parameter is calibrated to observed behaviour to capture the amount of stochasticity present.

For the region travel cost function we consider two attributes: congested travel time (instantaneous/experienced) and mean trip length. Thus, for the ID model, the travel cost of region r when travelling r-path $p \in P_m$ and departing during time-slice τ is:

$$c^{\tau}_{m,p,r} = \alpha_{tt} \bullet t^{\tau}_{m,p,r} + \alpha_{l} \bullet l_{m,p,r},$$

where $t^{\tau}_{m,p,r}$ is the instantaneous travel time (in [mins]) of region r when travelling regional path $p \in P_m$ and departing during time-slice τ, $l_{m,p,r}$ is the regional trip length (in [kms]) of region r when travelling regional path $p \in P_m$, and α_{tt} & α_{l} are the taste coefficients for travel time and length, respectively. For the ED model we replace $t^{\tau}_{m,p,r}$ with $\bar{t}^{\tau}_{m,p,r}$: the average experienced travel time of region r when travelling r-path $p \in P_m$ and departing during time-slice τ (see Section 4.2). The total travel cost of regional path $p \in P_m$ is calculated by summing up the costs of its regions: $C^{\tau}_{m,p} = \sum_{r \in R_{m,p}} c^{\tau}_{m,p,r}$.

Now, the deficiency of the MNL model in its inability to capture correlations between alternatives is well known. As Batista & Leclercq (2019) note, this presents clear limitations in handling the strong correlation between regional paths travelling in the same region, and found that it has the potential to significantly change the traffic patterns in regions. Therefore, to capture regional path correlations in this study, we heed the advice of Yildirimoglu & Geroliminis (2014) and adapt and adopt the C-Logit (CL) model (Cascetta et al., 1996). The C-Logit model captures regional path correlations by including heuristic correction terms within the probability relation to penalise r-paths for sharing travel costs with other r-paths. The CL probability of choosing r-path $p \in P_m$ when departing during time-slice τ is therefore:

$$Q^{\tau}_{m,p} = \frac{\left(\sigma^{\tau}_{m,p}\right)^{-\nu} \exp\left(-\theta C^{\tau}_{m,p}\right)}{\sum_{j \in P_m} \left(\sigma^{\tau}_{m,j}\right)^{-\nu} \exp\left(-\theta C^{\tau}_{m,j}\right)}, \tag{13}$$

where $\sigma^{\tau}_{m,p} > 1$ is the commonality factor for regional path $p \in P_m$ when departing during time-slice τ and $\nu \geq 0$ is the commonality scaling parameter. When $\nu = 0$, CL is equal to MNL, and larger values of ν move CL away from MNL.

In link-route choice, since the travel cost of a link is the same for all travellers, the commonality factor captures the shared cost between overlapping routes through summing the cost of each shared link. In regional path choice, however, the travel cost of a region is different for each regional path, and therefore the commonality factor captures the shared cost between overlapping regional paths through summing the shared cost in each shared region. The r-paths not similar in any way to any other r-path have commonality factors equal to 1 (similar only to itself) and no penalisation is incurred. The r-paths that are more similar to other r-paths (in terms of shared travel cost) have greater commonality factors and incur greater penalisation. The commonality factor is as follows for regional path $p \in P_m$ when departing during time-slice τ:

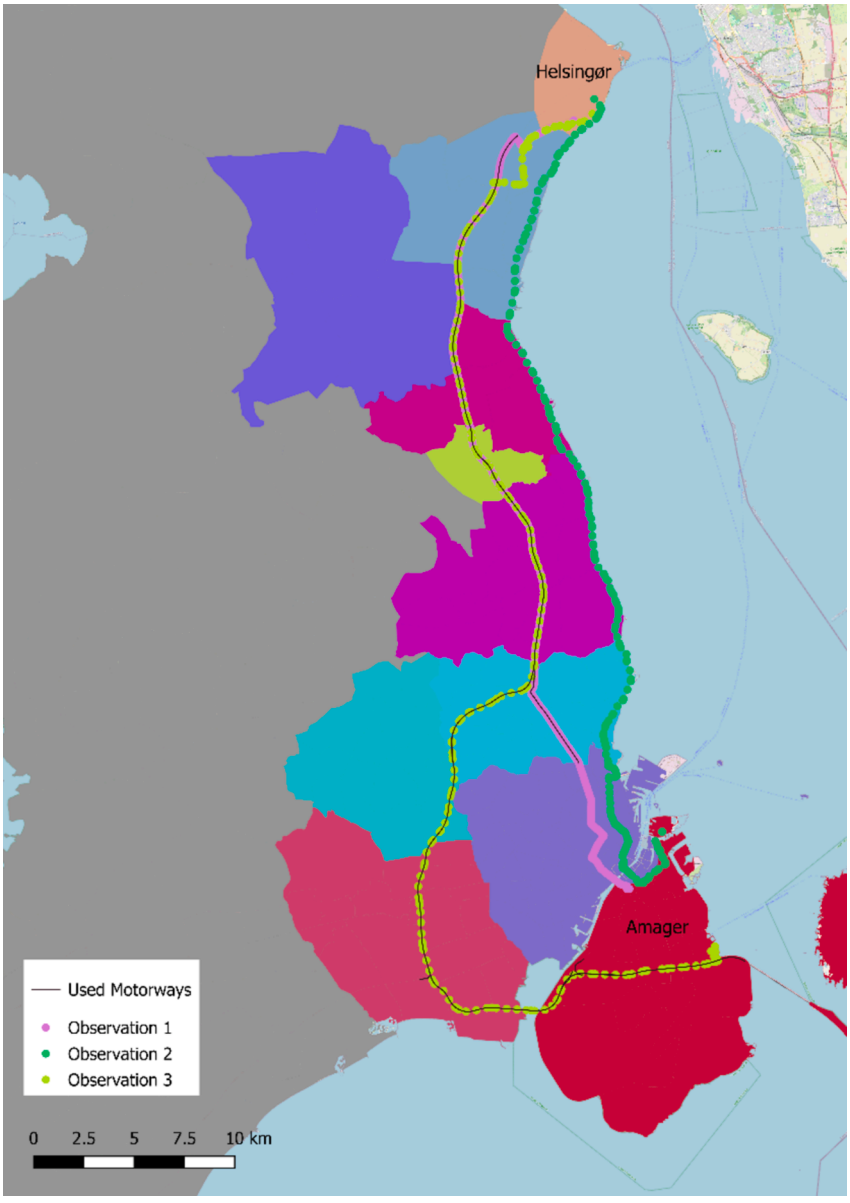

Fig. 20. Examples of three GPS trajectories travelling OD movement Helsingør to Amager (17 → 7), overlayed upon the regions used by regional paths for that OD.

$$\sigma^{\tau}_{m,p} = \sum_{k \in P_m} \frac{\sum_{r \in R_{m,p} \cap R_{m,k}} \min\left(c^{\tau}_{m,p,r}, c^{\tau}_{m,k,r}\right)}{\sqrt{C^{\tau}_{m,p}} \bullet \sqrt{C^{\tau}_{m,k}}},$$

where $\min\left(c^{\tau}_{m,p,r}, c^{\tau}_{m,k,r}\right)$ is the shared travel cost between r-paths p and k in region r, and thus $\sum_{r \in R_{m,p} \cap R_{m,k}} \min\left(c^{\tau}_{m,p,r}, c^{\tau}_{m,k,r}\right)$ is the total shared travel cost between r-paths p and k.[7]

A distinct difference between traditional route choice on link networks and regional path choice on regional networks, led us to test

[7] Batista & Leclercq (2019) argue that the correlation between two regional paths occurs due to the MFD assumption of homogeneous traffic conditions inside a region, i.e. that all vehicles travelling inside a region are assumed to have the same speed. It is therefore acknowledged that C-Logit might not be able to fully capture all correlations between aggregate dynamic regional path choices, though the estimation results provide encouragement that some correlation is being captured.

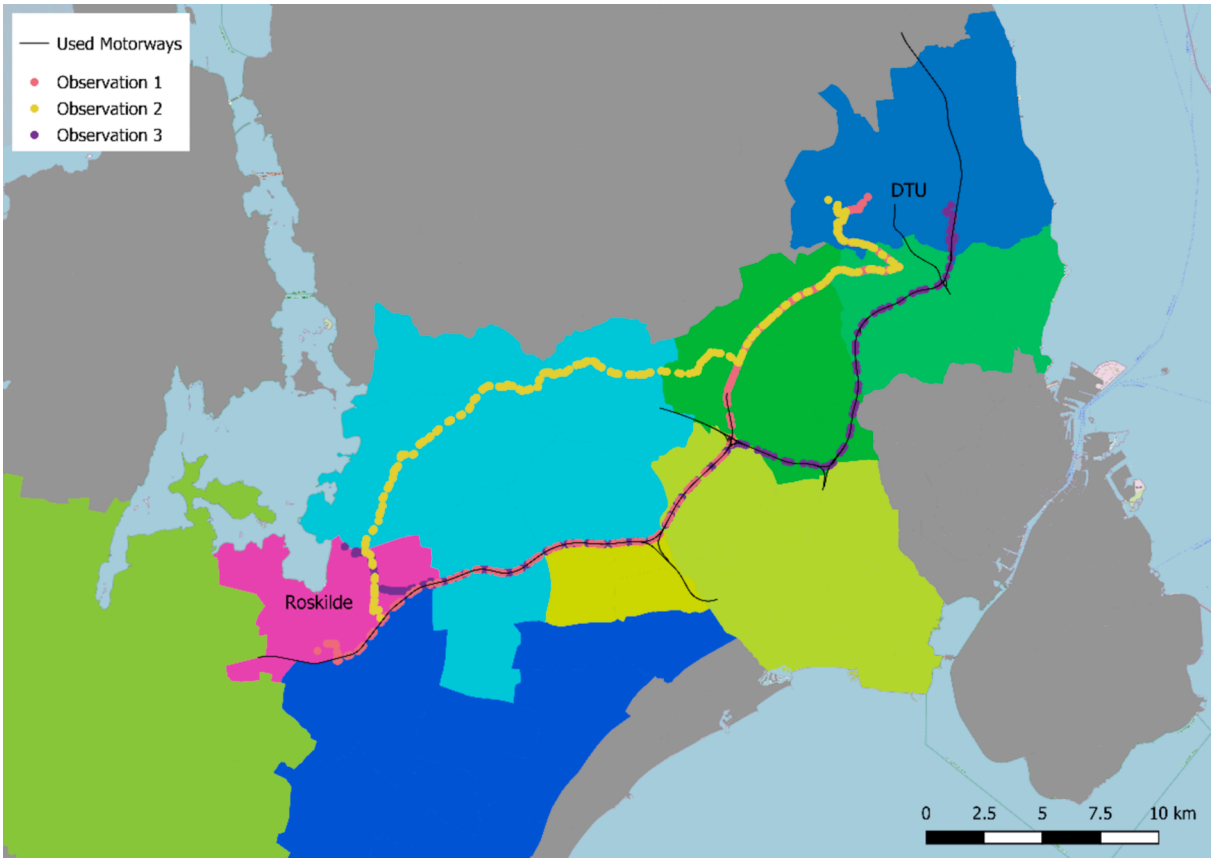

Fig. 21. Examples of three GPS trajectories travelling OD movement Roskilde to DTU (6 → 11), overlayed upon the regions used by regional paths for that OD.

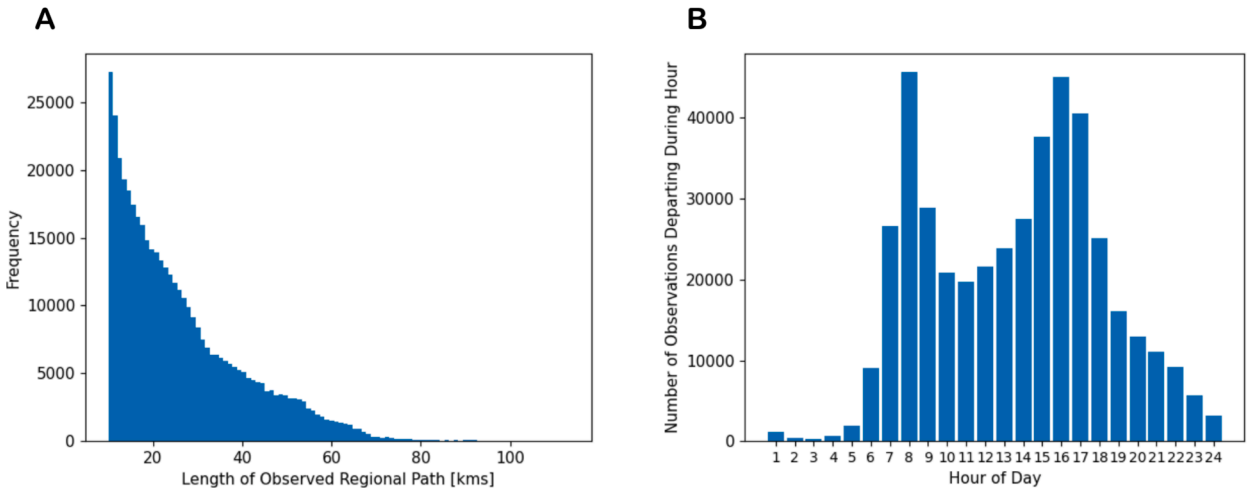

Fig. 22. Distributions of the lengths (**A**) and departing times (**B**) of the regional path observations.

also an alternative specification of regional path travel cost, where travel cost in the origin/destination regions is excluded. This is explained as follows.

In traditional route choice, travel demand typically departs from a zone centroid node, connected to the network through one or more connector links, each representing an average travel cost egressing/accessing true origins/destinations in the zone. Usually though, the travel cost of a connector link is relatively small compared to the total travel costs of routes, and thus, if there are multiple

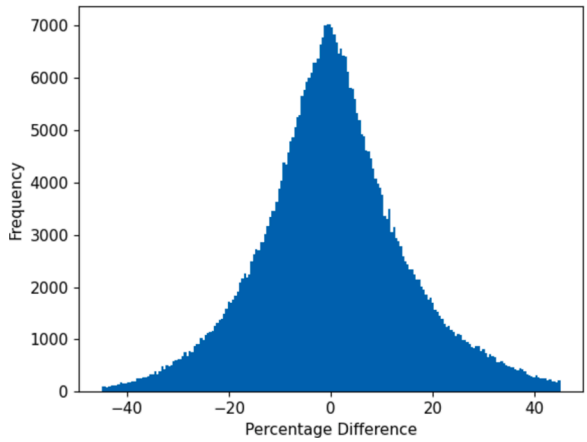

Fig. 23. Distribution of the percentage differences between the lengths of the observed regional paths and the lengths of the matched generated regional paths. (Observed minus matched).

connector links for one zone, the travel costs of the connector links have a low impact on route choice probabilities. In regional path choice, however, due to the large spans of the underlying origin/destination regions, travel costs egressing/accessing these regions[8] are more substantial compared to total regional path travel costs. Thus, if one were to base regional path choice on total travel costs including costs spent egressing/accessing origin/destination regions, these egress/access costs could potentially have a large influence upon regional path choice probability. However, given that it is not known where in the origin/destination regions the accumulated regional OD movement travel demand is originating/destinating, the regional path choice we are trying to capture is the regional path choice from a general point within the origin/destination regions. If the egress/access costs are highly influential upon regional path choice, we hypothesise that this may misrepresent regional path choice behaviour.

To demonstrate, consider Fig. 24 where there are three underlying regions R1-3 and two superimposed motorway regions M1-2 connecting R1 to R3 through R2. The regional OD movement under consideration is R1 to R3 where there are two corresponding zone-zone OD movements on the underlying link network Z1 to Z2 and Z3 to Z4. There are two regional paths, one corresponding to each of the zone-zone OD movements going via the two motorways: r-path 1: R1 → M1(R1) → M1(R2) → M1(R3) → R3, r-path 2: R1 → M2(R1) → M2(R2) → M2(R3) → R3. Now, if we were to base regional path choice on total r-path travel costs (travel time and length), clearly from Fig. 24 the egress/access costs for r-path 1 in R1 and R3 will be longer than for r-path 2, and thus the MNL r-path choice probability of r-path 1 will be lower than for r-path 2. However, given the travel costs of r-paths 1 & 2 in the non-origin/destination regions (i.e. in M1(R2) and M2(R2)) are likely to be similar, from a general point in R1 to a general point in R2, it appears difficult to choose between r-paths 1 & 2, thus suggesting equal choice probabilities.

In the following subsection we therefore test the hypothesis that choice behaviour can more realistically be captured by basing regional path choice on regional path travel costs excluding costs in origin and destination regions. Note that for the CL model this entails also excluding shared travel costs in the origin and destination regions in the calculation of the commonality factors.

For the parameter estimation, there are four parameters to estimate: $\psi = (\theta, \nu, \alpha_{tt}, \alpha_l)$. However, to ensure identification we shall normalise the taste coefficients relative to travel time, i.e. set $\alpha_{tt} = 1$ so that α_l is the estimated preference relative to travel time (i.e. $\alpha_l = \frac{\alpha_l}{\alpha_{tt}}$). The parameter bounds of the L-BFGS-B algorithm were set as $\widetilde{\theta} \in [0.001, 2]$, $\widetilde{\nu} \in [0, 2]$, and $\widetilde{\alpha}_l \in [0.001, 2]$. After experimenting with different initial conditions in Step 1 of Algorithm 3, we did not find any cases of multiple estimate solutions, nor any solutions at any boundary.

6.2.3. Estimation results

We begin by testing the hypothesis made in Section 6.2.2 that, at least in this case study, choice behaviour may be more realistically captured by basing regional path choice on regional path travel costs excluding costs in the origin and destination regions. Table 2 displays results from estimating the ED model including and excluding origin/destination region costs, with a time-slice grain of 30 min and with the CL regional path choice model. As can be seen, excluding origin/destination region costs provides considerably better fit to the data.[9] This implies the regional path choice probabilities better capture behaviour with these regional path travel costs. Furthermore, when including origin/destination region costs, the estimated commonality scaling parameter ν is estimated to be 0 (the lower limit set), resulting in the CL model collapsing to the MNL model, thereby not capturing any regional path correlations. When excluding origin/destination region costs, however, ν is estimated greater than zero, thus capturing correlations. Noticeably also, the

[8] This includes costs spent in the underlying origin/destination regions and costs spent on motorways that superimpose these regions.

[9] Note that when including regional path GPS observations with the same or adjacent OD regions and with total lengths less than 10km in the dataset (see Section 6.2.1), basing regional path choice on regional path costs excluding OD region travel cost also provides considerably better fit to the data, and more realistic parameter estimates.

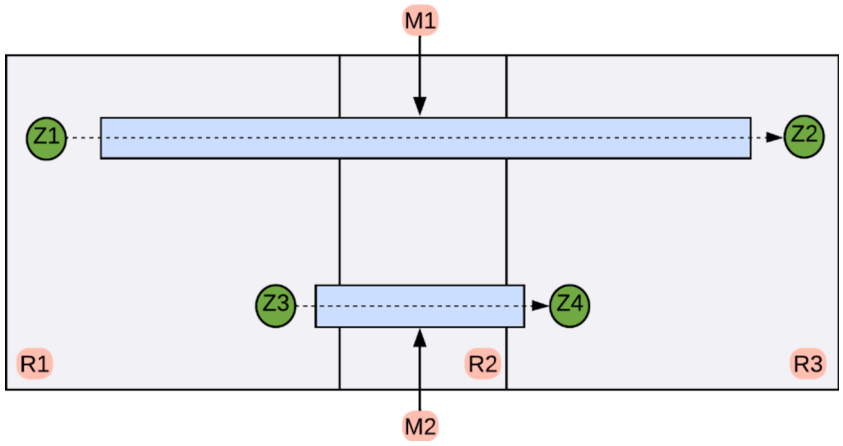

Fig. 24. Demonstrating regional path choice with and without including travel cost in origin and destination regions.

Table 2
Estimation results testing whether to base regional path choice on regional path travel costs including or excluding travel costs in origin and destination regions.

Including/Excluding	$\widehat{\theta}$	$\widehat{\nu}$	$\widehat{\alpha}_l$	Log-Likelihood
Including	0.0626	0	0.0296	−1172979
Excluding	0.1363	0.2165	0.3355	−1080062

Table 3
Estimation results basing regional path choice on regional path travel costs excluding costs in the origin and destination regions.

Dynamic Model	Time-Slice Grain	$\widehat{\theta}$	$\widehat{\nu}$	$\widehat{\alpha}_l$	Log-Likelihood
ID	1 h	0.1378	0.2238	0.3019	−1080816
ED	1 h	0.1385	0.2221	0.2900	−1080444
ID	30 mins	0.1367	0.2162	0.3390	−1080199
ED	30 mins	0.1363	0.2165	0.3355	−1080062
ID	15 mins	0.1349	0.2024	0.3949	−1079531
ED	15 mins	0.1342	0.2034	0.3949	−1079433

estimated $\widehat{\theta}$ parameter is smaller for including than excluding, which accords with the demonstration in Fig. 24, with the lower θ values making the r-path choice probabilities more even-split for regional OD movements in which the access/egress costs have negatively influenced regional path choice. For the remainder of the paper, we shall therefore base regional path choice on regional path travel costs excluding costs in the origin/destination regions.

We shall next compare results from estimating the dynamic multi-region MFD SUE model under different specifications. Table 3 displays results from estimating the ID and ED models with different settings of the time-slice grain,[10] with CL regional path choice probabilities.

The first thing to note is that the ED model outperforms the ID model for each setting of the time-slice grain. This provides empirical evidence to support the hypothesis that regional path choice is more realistically based on experienced regional path travel times rather than instantaneous. This also suggests that there is some inertia or habitual effect present, i.e. drivers have some understanding of the regional path travel times they will experience.

One can also see that the commonality scaling parameter estimates $\widehat{\nu}$ are estimated greater than zero, implying that regional path correlations are being captured, and it is beneficial to do so. We compared estimation results for the CL model in Table 3 with those for the MNL model, and found that CL outperformed MNL in all cases. For example, when estimating the ED model with 30-min time-slices with MNL the Log-Likelihood value is −1081395, whereas it is −1080062 for CL.

The $\widehat{\theta}$ parameter estimates are not approximating infinity, nor approximating zero. This is demonstrated in Fig. 25B where the Log-Likelihood surface is plotted around the maximum. As can be seen, the Log-Likelihood value is concave around the maximum, with big decreases in Log-Likelihood value away from the maximum. This clear shows that model fit is sensitive to the value of θ, with a concave

[10] Note that this time-slice granularity refers to the granularity of the discrete-time dynamic traffic model. These time-slices do not correspond in any way to the time periods discussed in Section 5.2 regarding the calibration of the speed-MFD functions.

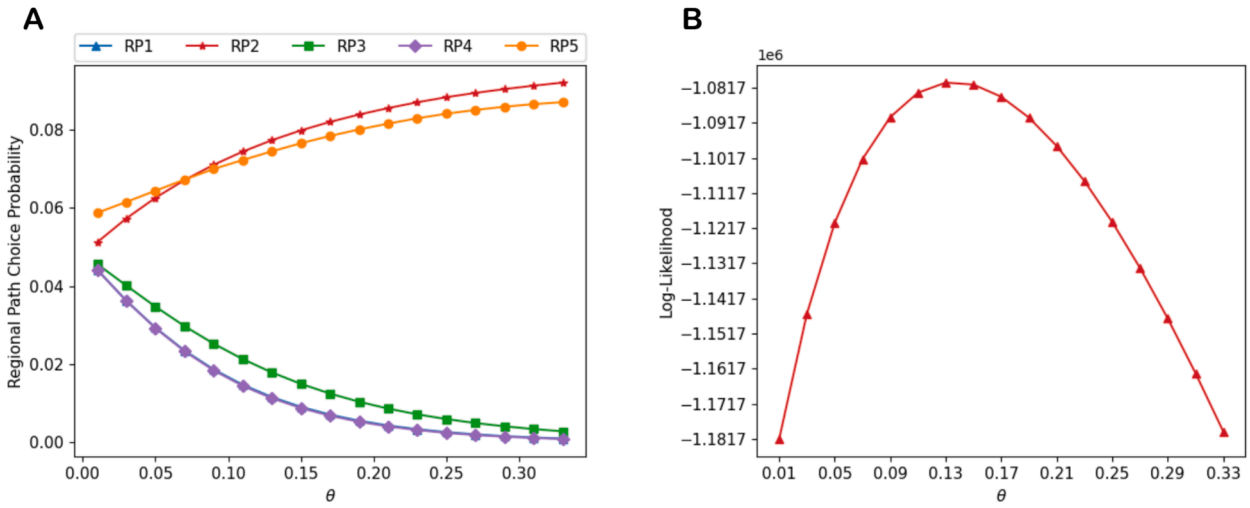

Fig. 25. **A:** Equilibrated regional path choice probabilities from the ED model (with 30 min time-slices) as the θ Logit scaling parameter is varied. **B:** Log-Likelihood as θ is varied around $\widehat{\theta} = 0.1363$.

shape, showing that we are far from both purely random choice ($\theta \to 0$) and deterministic choice ($\theta \to \infty$). This supports the claim that stochasticity should be included within the regional path choice, but shows that we are capturing regional path choices reasonably well.

The $\widehat{\alpha}_l$ parameter estimates of around 0.3–0.4 [min/km] imply that a driver is prepared to travel roughly 2.5–3.33 km further to save 1 min of travel time. Distance is though an influential parameter: when estimating the ED model with 30-min time-slices without the distance attribute (i.e. just travel time), the Log-Likelihood value is −1082828, compared to −1080062 with distance.

Overall, the stability of the estimates across different model specifications and time-slice grains indicates that the model is robust, which is not something that is obvious given the complexity of model components and requirement to solve a bi-level fixed-point problem. This is a general feature we have found with model with the STG traffic propagation.

7. Analysis of model outputs

In this section, we explore the outputs from the ID and ED models in the application of the case study. Unless specified otherwise, the ID and ED models are solved with CL using the calibrated parameter values in

7.1. Continuity

Here, we demonstrate that, for a given time-slice grain, equilibrated regional path choice probability outputs from the ID and ED models appear to be continuous in model parameters. Fig. 25A displays equilibrated regional path choice probabilities from the ED model with 30-min time-slices for a given OD movement / departing time-slice as the θ Logit scaling parameter is varied. Fig. 25B displays the Log-Likelihood in (11) as θ is varied. As shown, both outputs are continuous. As expected, the regional path choice probabilities disperse as θ increases as implied stochasticity levels decrease and/or drivers become less sensitive to differences in experienced regional path travel time. And, the Log-Likelihood surface is concave around the maximum, which from Table 3 is 0.1363.

7.2. Differences between ID and ED models

Fig. 26 displays for a regional path (with 16 regions) from regional OD movement 19 → 7 (Hillerød to Amager through central Copenhagen), the region travel times used for the regional path choice for the ID and ED models (with 15-min time-slices), when departing at different times throughout the day. As shown, in early regions of the regional path the instantaneous and experienced region travel times are similar, as one would expect. In latter regions, however, there is a clear difference. The trends of the region travel times are similar, but for the ED model the more heavily congested peak-hour travel times are shifted to earlier departing time-slices. This is because the traffic conditions actually experienced in the latter regions, which in this case are the central Copenhagen regions, will be skewed from the conditions when the driver departs. For example, if a driver departs at 7am, the current traffic conditions in the latter regions will be less congested than when the driver actually reaches those regions at 8am. Similarly, if a driver departs at 8am, the current traffic conditions in the latter regions will be more congested than when the driver reaches them at 9am.

Fig. 27A plots, for two regional paths travelling OD movement 19 → 7, the instantaneous and experienced regional path travel times when departing at different times across the day. Fig. 27B plots the regional path choice probabilities from the ID and ED models across the day. From Fig. 26, a driver knows that if they depart off-peak at 6am, they will experience the on-peak 7am traffic conditions in latter regions when they get there. Thus, the experienced travel times are greater when departing just before the peaks than the

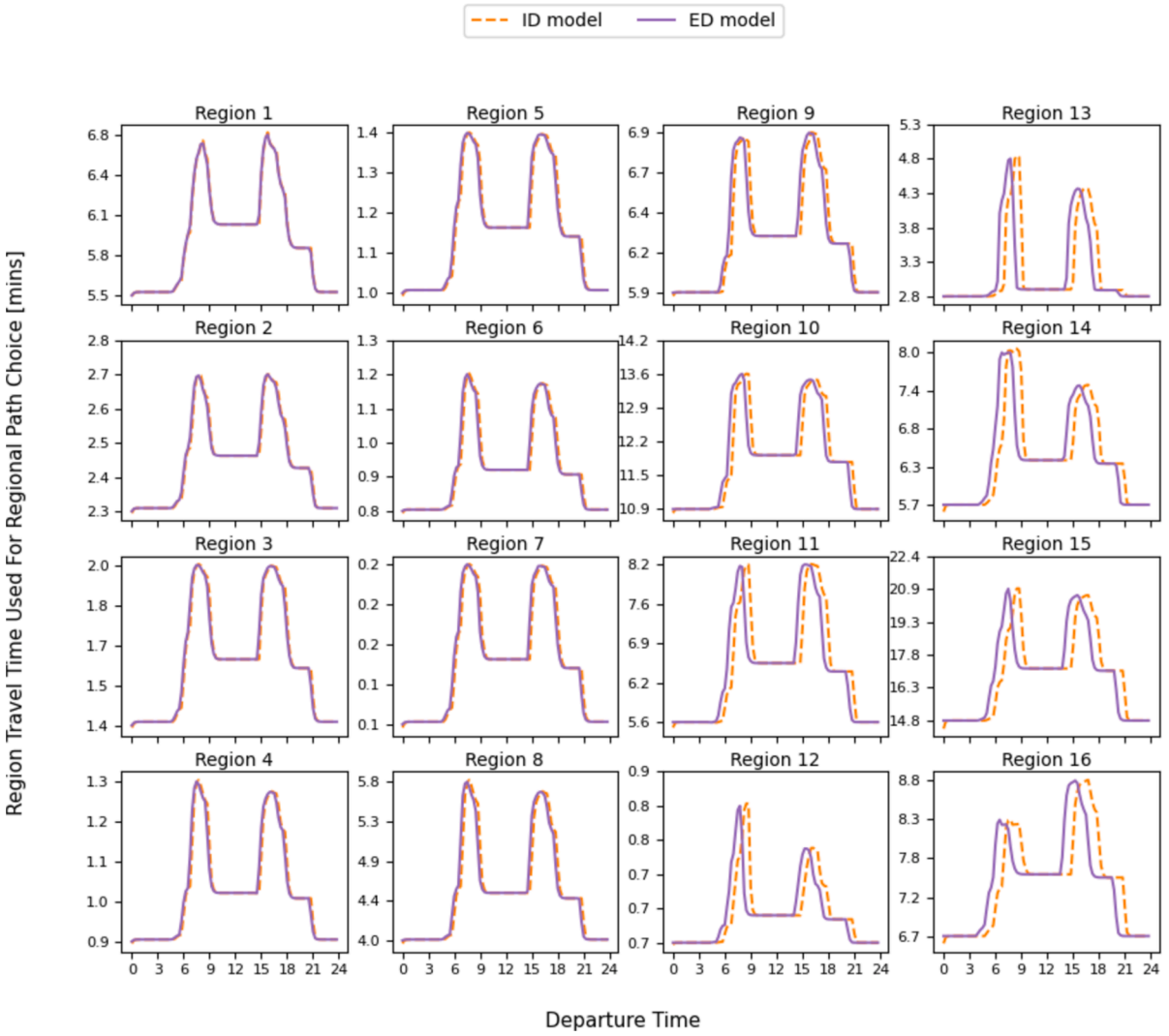

Fig. 26. Demonstrating the difference between the region travel times used for the regional path choice for the ID and ED models (15-min time-slices). Regional path (with 16 regions) from region 19 to region 7 (Hillerød to Amager through central Copenhagen).

instantaneous travel times, and lower when departing at the end of the peaks. This impacts regional path choice. To minimise their experienced travel times, drivers distribute themselves between the regional paths differently than if they were minimising instantaneous travel times. This is clearly shown in Fig. 27B, where drivers adjust regional paths earlier for the afternoon peak to minimise experienced travel times. This in turn impacts region accumulation levels. In general, our interest is on how user benefits can be evaluated over different policy scenarios, and for this purpose regional path choice probabilities and travel times are key. Basing the dynamic model on experienced travel times achieves internal consistency within the model, which provides greater behavioural realism (as the estimation results in Section 6.2.3 show).

Being able to operate with experienced travel times has numerous other benefits. Experienced travel times are vital if one were to extend the model to account for example for departure time choice, elastic demand / mode choice, and integration within policy scheme optimisation procedures, e.g. toll-price optimisation. It is clearly much more behaviourally realistic that travellers minimise travel costs actually experienced rather than instantaneous costs.

7.3. Sensitivity to time-slice grain

Next, we compare outputs from the discrete-time dynamic traffic model for different settings of the time-slice grain. Fig. 28A displays the accumulation levels in region 8 over the course of the day from the ED model with different time-slice grains. Fig. 28B displays the experienced travel time of a regional path travelling OD movement 11 → 7 when departing at different times across the day, from the ED model with different time-slice grains. As shown, the differences between the outputs for different grains are

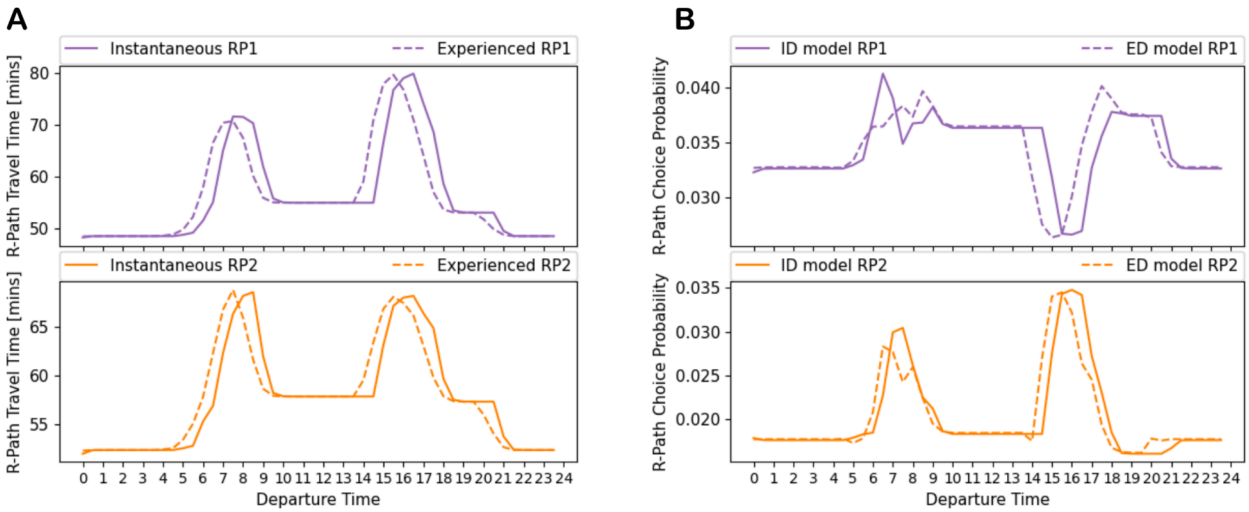

Fig. 27. **A:** Experienced and instantaneous travel times of two regional paths from region 19 to region 7 when departing at different times across the day. **B:** ID model and ED model choice probabilities for these regional paths when departing at different times across the day.

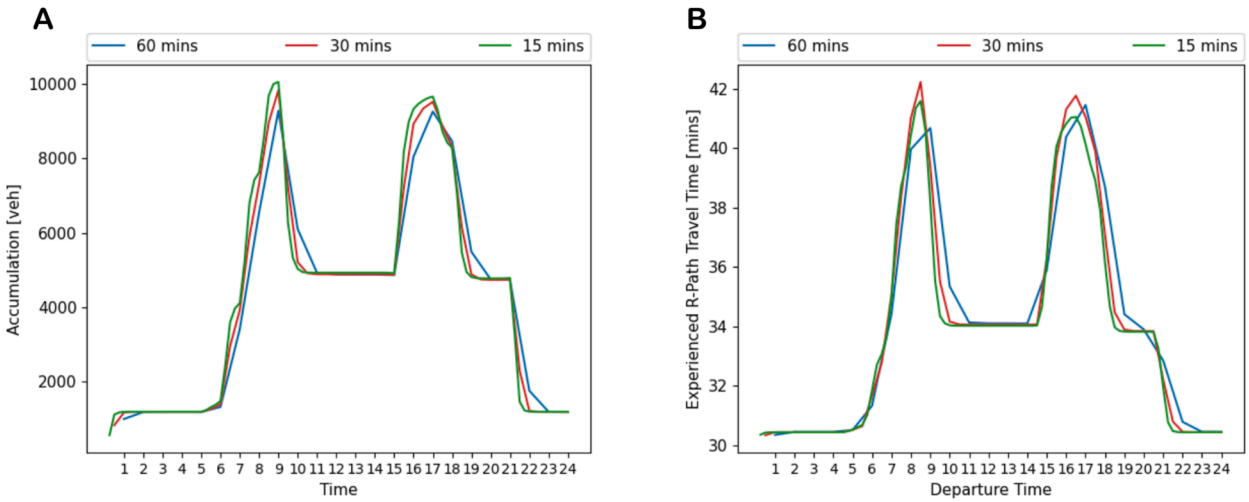

Fig. 28. Difference between the outputs from the ED model with different time-slice grains. **A:** Accumulation levels in region 8 over the course of the day. **B:** Experienced travel time of a regional path travelling OD movement 11 → 7 when departing at different times across the day.

relatively marginal.

7.4. Cross-comparison with data

Here, we compare travel times from the model with those from the observations (the GPS trajectory data used for the parameter estimation in Section 6.2). Fig. 29A-D displays, for four different regional OD movements, a cross-comparison between average observed and average modelled OD movement travel times when departing at different 30-minute time-slices across the day. The average observed regional OD movement travel times were obtained by averaging the travel times of all the observations travelling that OD movement and departing during that 30-minute time-slice. The modelled travel times were obtained according to a choice-probability-weighted-average of the regional path travel times for that OD movement when departing during that time-slice. As shown, the observed and modelled travel times are relatively similar across the day, and display similar patterns. Looking across all regional OD movements and departing time-slices, the average percentage difference between observed and modelled travel times was 4.7%, with a standard deviation of 19.9%. Fig. 30 displays the distribution (observed minus modelled). This indicates a good overall fit between the data and the model, and thus reasonable model outputs. This was furthermore supported by the manual inspection of many regional OD movements and comparing travel times with those from observations (as e.g., in Fig. 29A-D), from Google Maps, and from personal experiences.

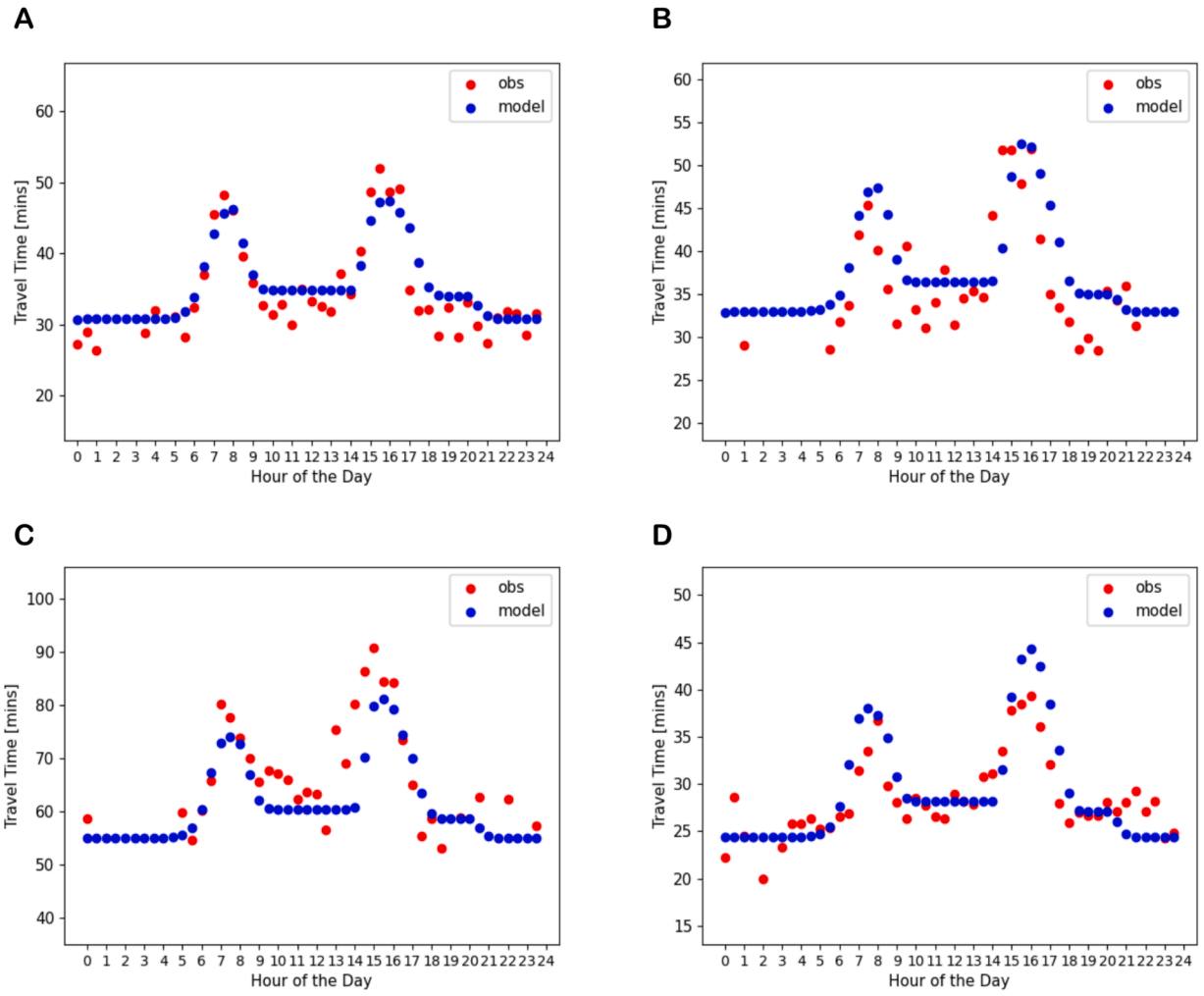

Fig. 29. Comparison between observed travel times and modelled travel times for different OD movements at different departure times throughout the day. **A:** Region 7 to Region 11. **B:** Region 11 to Region 6. **C:** Region 19 to Region 102 port zone. **D:** Region 9 to Region 7.

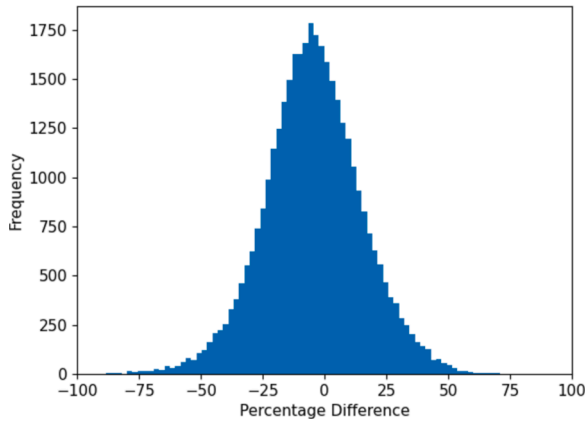

Fig. 30. Distribution of the percentage differences between average observed and average modelled travel times for different regional OD movements and departing time-slices (observed minus modelled).

8. Summary and future research

Multi-region Macroscopic Fundamental Diagram (MFD) traffic equilibrium models have been developed as a more easily calibratable, maintainable, and computationally efficient alternative to classical link-network traffic equilibrium models with full disaggregate network representation. This paper has developed a new dynamic multi-region MFD Stochastic User Equilibrium (SUE) modelling framework, where the traffic propagation dynamics are based on a new approach utilising features of a Space-Time Graph (STG). Vehicles are tracked on a STG based on region travel times, and accumulation levels are calculated based on occupying STG areas of flow. Accumulation levels feed back to determine region speeds and consequently region travel times. The STG-based traffic propagation model is thus expressed as a fixed-point problem. This traffic propagation model, for equilibrating region travel times, is embedded within an SUE fixed-point problem for equilibrating the regional path flows. Regional path choice can e based on either instantaneous region travel times at the time-slice of departure (Instantaneous Dynamic (ID) model), or the region travel times actually experienced at the time-slice of travel (Experienced Dynamic (ID) model). A solution algorithm has been proposed for solving the overall bi-level fixed-point problem, iterating between a Traffic Propagation Stage and a Flow Updating Stage.

The dynamic multi-region MFD SUE model has been applied in a real-life large-scale and detailed case study of Zealand, Denmark. The multi-region MFD system uniquely consists of underlying urban and rural regions and directional superimposed motorway regions, 135 regions in total, much larger than any previously. Speed-MFD functions for each region were calibrated using an enormous dataset of GPS records and loop detector vehicle counts. An exponential speed-MFD functional form was fitted for underlying regions and a piecewise-exponential form was fitted for motorway regions. The travel demands for each regional OD movement were obtained by aggregating inter-zonal travel demands from an underlying network model. Regional path choice sets and regional trip lengths were obtained by generating inter-zonal shortest path routes on the underlying network based on different link travel costs.

Parameters of the dynamic multi-region MFD SUE model were calibrated using a large dataset of 434,860 regional path observations. The model producing continuous choice probability outputs facilitated the development of a maximum likelihood estimation procedure for consistently estimating parameters of underlying regional path choice models within the dynamic multi-region MFD SUE model. To estimate the model parameters consistent with the equilibrium, this means solving a bi-level maximum likelihood problem subject to equilibrium constraints. The findings were that:

- The models could be successfully estimated through the procedure.
- The C-Logit (CL) model provided better fit to the data than the Multinomial Logit (MNL) model, supporting the hypothesis that it is important to consider correlations between overlapping regional paths.
- The ED model provided better fit to the data than the ID model, supporting the hypothesis that regional path choices are more realistically based on experienced travel times.
- Better fit to the data was found when excluding travel costs in the origin/destination regions.
- Observations did not just take the lowest costing modelled regional paths, supporting the claim that stochasticity should be considered when modelling regional path choice.
- Congested travel time was more influential upon regional path choice than distance.
- The parameter estimates were relative stable across different model specifications and time-slice grains, indicating that the model is robust.

Given the estimated models, numerical experiments were conducted showing that:

- For a given time-slice grain, the model produces continuous equilibrated regional path choice probability and thereby Log-Likelihood outputs.
- There are clear differences between the ID and ED models in terms of the travel times used for the regional path choice, which impacts regional path choice.
- Results are relatively insensitive to the time-slice grain.
- By comparing travel times from the model with those observed from GPS data, from Google Maps, and from personal experiences, the outputs of the model are reasonable.

Future research includes estimating the dynamic multi-region MFD SUE model with other regional path choice models. For example, considering additional travel cost attributes to congested travel time and distance, such as average number of opposing turns, reliability, etc. And/or, estimating other choice models to MNL and CL. For example, a Weibit-type model (Castillo et al., 2008) to account for heteroscedasticity of error terms, or a mixed logit model (McFadden & Train, 2000) to account for taste heterogeneity. Future research also includes exploring how to operate the dynamic multi-region MFD SUE model with discrete distributions for the regional trip lengths. Currently, the mean trip length is used, but as Batista & Leclercq (2019) find, capturing the variability in trip lengths has the potential to significantly impact the traffic dynamics. One could also explore making the regional trip lengths consistent with the traffic equilibrium, such as done by Yildirimoglu & Geroliminis (2014), Batista et al. (2021b). This could possibly be done by calibrating regional trip length functions, which for each region/r-path is some continuous, increasing function of the region accumulation given some parameters $\boldsymbol{\alpha}$: $l_{m,p,r}(n_r;\boldsymbol{\alpha})$. Future research could also explore more efficient methods for solving the ID and ED models. For example, as mentioned in Section 4.4, it is possible to solve the ID model with a rolling horizon, which has the potential to improve convergence. Lastly, as discussed in Section 4.1, congestion capacities and receiving capacities are currently not considered in the traffic equilibrium. Although this was not found to be an issue in our case study, future research includes exploring how to account for region capacities in the model, for example following the works of Yildirimoglu & Geroliminis (2014), Mariotte & Leclercq (2019), Mariotte et al. (2020), and Huang et al. (2020).

CRediT authorship contribution statement

Lawrence Christopher Duncan: Writing – review & editing, Writing – original draft, Visualization, Software, Methodology, Investigation, Funding acquisition, Formal analysis, Data curation, Conceptualization. **Thomas Kjær Rasmussen:** Writing – review & editing, Supervision, Software, Project administration, Methodology, Investigation, Funding acquisition, Data curation, Conceptualization. **David Paul Watling:** Writing – review & editing, Methodology. **Otto Anker Nielsen:** Conceptualization.

Declaration of competing interest

The authors declare that they have no known competing financial interests or personal relationships that could have appeared to influence the work reported in this paper.

Acknowledgements

We gratefully acknowledge the funding provided by the Independent Research Fund Denmark for the project “Optimal tolls for reaching emissions goals: A novel behaviourally realistic and national-scale applicable road transport modelling system” [Grant ID: 0217-00173B].

Appendix A. Nomenclature

Table 4 details the main nomenclature used in this paper.

Table 4
Nomenclature used in this paper.

Term	Description
Dynamic multi-region MFD SUE model	
R	Set of regions
n_r	Accumulation in region r
$W_r(n_r)$	Production-MFD function for region r given accumulation n_r
$v_r(n_r)$	Speed-MFD function for region r given accumulation n_r (space-mean speed)
r^O	Origin region
r^D	Destination region
μ^O	Internal/external origin indicator (0 if internal, 1 if external)
μ^D	Internal/external destination indicator (0 if internal, 1 if external)
M	Set of regional OD movements
P_m	Set of regional paths for OD movement m

(*continued on next page*)

Table 4 (*continued*)

Term	Description
N_m	Number of regional paths for OD movement m
N	Total number of regional paths
$R_{m,p}$	Set of regions in regional path p of OD movement m
Ψ	Set of indexed time-slices
ε	Time-slice duration
d_m^τ	Travel demand for OD movement m departing during time-slice τ
$f_{m,p}^\tau$	Vehicle flow departing during time-slice τ travelling regional path p of OD movement m
F	Set of all demand-feasible non-negative regional path flow vector solutions
$l_{m,p,r}$	Mean regional trip length of region r when travelling regional path p of OD movement m
$t_{m,p,r}^\tau$	Mean travel time to cross region r when entering the region during time-slice τ travelling regional path p of OD movement m
$\bar{v}_r^\tau$	Average speed in region r during time-slice τ (space- and time-mean speed)
$\overline{n}_r^\tau$	Average accumulation in region r during time-slice τ
$\overline{n}_{m,p,r}^{\tau' \to \tau}$	Average accumulation in region r during time-slice τ from the flow departing during time-slice τ' travelling regional path p of OD movement m
$A_{m,p,r}^{\tau' \to \tau}$	Area of the region r time-slice τ quadrant of the STG that is occupied by any vehicle travelling regional path p of OD movement m departing during time-slice τ' (proportional occupying STG area)
$H_{m,p,r}^\tau$	Region travel time fixed-point function
$T_{m,p}^\tau$	Total instantaneous travel time of regional path p of OD movement m when departing during time-slice τ
$Q_{m,p}^\tau$	Probability regional path p of OD movement m is chosen when departing during time-slice τ
$\boldsymbol{D}_m^\tau$	$N_m \times N_m$ diagonal matrix of the travel demand for OD movement m at time-slice τ (i.e. with d_m^τ on each diagonal element)
$\bar{t}_{m,p,r}^\tau$	Average travel time experienced to cross region r when departing during time-slice τ travelling regional path p of OD movement m
$\Psi_{m,p,r}^\tau$	Set of active time-slices that some time is spent in traversing region r by any vehicle departing during time-slice τ travelling regional path p of OD movement m
$\overline{T}_{m,p}^\tau$	Total average experienced travel time of regional path p of OD movement m when departing during time-slice τ
Calibration of speed-MFD functions	
K_r	Set of accumulation-speed datapoints for region r
n_r^κ	Average accumulation in region r during time-period κ
v_r^κ	Average speed of vehicles in region r during time-period κ
TDT_r^κ	Total distance travelled by GPS units in region r during time-period κ
TTT_r^κ	Total time travelled by GPS units in region r during time-period κ
Y_r^κ	Set of GPS units that were observed travelling in region r at any moment during time-period κ
$D_{r,y}^\kappa$	Distance travelled by GPS unit y in region r during time-period κ
$T_{r,y}^\kappa$	Time travelled by GPS unit y in region r during time-period κ
δ	Time-period duration
Γ	Penetration rate
a	Speed-MFD function free-flow region speed parameter
b, c	Speed-MFD function free curve parameters
h	Speed-MFD function minimum speed parameter
n_r^{crit}	Speed-MFD function critical accumulation parameter
Estimation of model parameters	
$\boldsymbol{y}$	Vector of regional path observation data
L	Likelihood function
LL	Log-Likelihood function
$\boldsymbol{\psi}$	Vector of model parameters
$\phi_{m,p}^\tau$	Number of observations that take regional path p of OD movement m when departing during time-slice τ
θ	Logit scaling parameter
α_l	Regional path choice taste preference parameter for length (relative to travel time)
ν	Commonality scaling parameter

Appendix B. Demonstration of traffic propagation model features

In this section we give a visual overview of the traffic propagation model, providing a thorough description of the model features. Fig. 31 displays a STG for a regional path with 5 regions. The x-axis represents 'space', i.e. the sequence of regions in the regional path, where x values within a region represent the proportion of the region completed. The y-axis represents 'time' which has been split into discrete equal-sized time-slices of duration ε, where y values within a time-slice represent the proportion of the time-slice completed. In the top left corner of each region at each time-slice, the constant travel time of the region throughout the time-slice is displayed.

Also displayed on the STG in Fig. 31 is the trajectory of the first vehicle departing at the beginning of time-slice 0, and the trajectory of the last vehicle departing at the end of time-slice 0 (which is the same as the trajectory of the first vehicle departing at the beginning of time-slice 1). Given the travel time for a region during a time-slice is constant, the trajectory of a vehicle in a region during a time-slice is a straight line, where the steepness of the line depends on the region travel time compared to the time-slice duration. For example, the travel time of region 1 at time-slice 0 is 4 min compared to the time-slice duration of 8, and thus the gradient of the line is $\frac{4}{8}$, meaning that a vehicle departing from / entering the region at the beginning of the time-slice will exit the region at $\frac{4}{8}$ ths of the way through the time-slice.

As shown, the propagation of the entire regional path flow departing at time-slice 0 is contained within the trajectories of the first/last vehicles departing at the beginning/end of time-slice 0. Clearly, at any given moment in time, each vehicle in the flow must either

not have departed yet, be in one of the r-path's regions, or have destinated. For moments in time where all of the flow has departed and none of the flow has destinated, i.e. in this example between the beginning of time-slice 1 and end of time-slice 2, the first departing vehicle of the flow will be some proportion of the way through a region, and the last departing vehicle will be some proportion of the way through a preceding region (or be a greater proportion of the way through that region). All the vehicles in the flow will be spread across the region(s) between where the first and last departing vehicles are. For example, at the end of time-slice 0, the first vehicle is half of the way through region 3 while the last vehicle is at the beginning of region 1. Therefore, the regional path flow must be spread between these points at that moment in time.

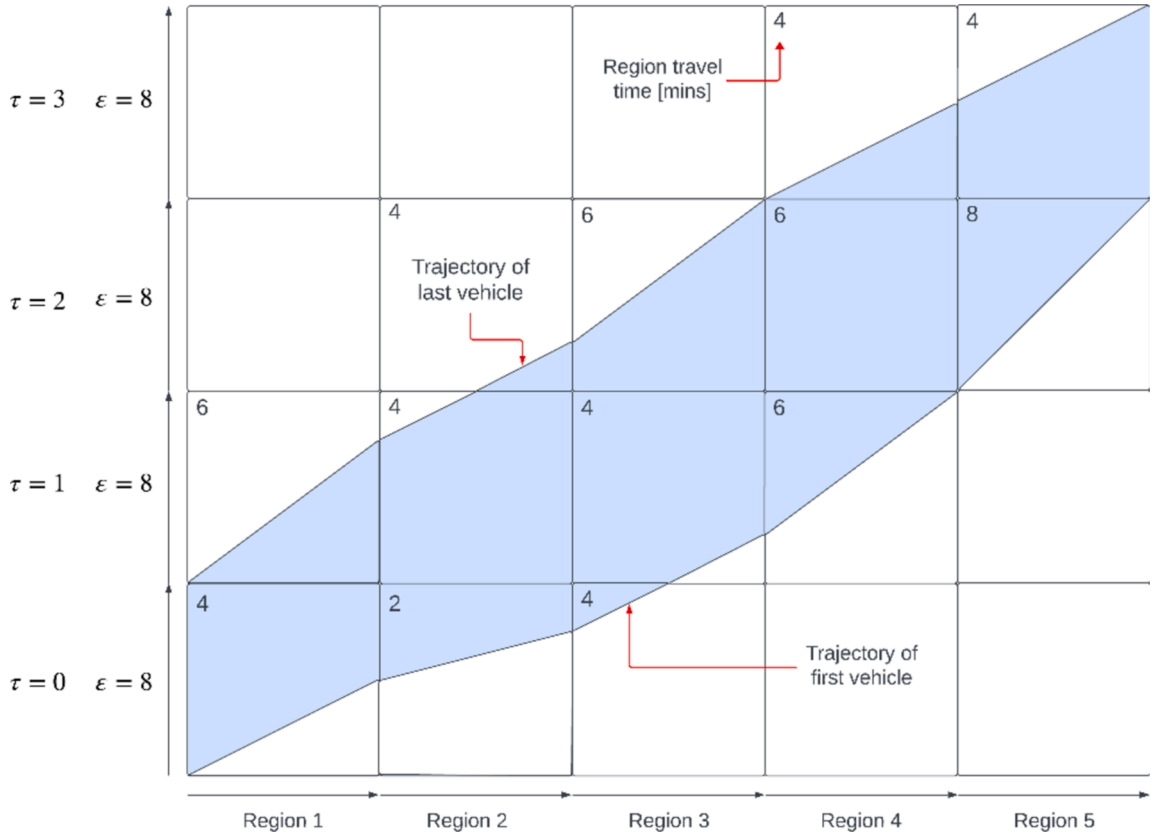

Fig. 31. Illustrating on a space time graph traffic propagation for a 5-region regional path.

Now, the assumption we make is that the flow is spread across the regions between where the first and last vehicles are according to the occupied regional trip lengths of the regions at that moment of time. The occupied regional trip length of a region is the length completed by the first vehicle but not yet completed by the last vehicle, at that moment in time. Fig. 32 displays at different moments in time the occupied lengths of the regions from the regional path flow. Displayed in the top right corner of each region at each time-slice is the constant regional trip length of the region. In this study, we assume the regional trip lengths are constant across time-slices, though this need not be the case. The region travel times have been omitted for clarity of display, these can be seen in Fig. 31.

As shown, at the end of time-slice 0, regions 1 & 2 have been completed by the first vehicle but not reached at all by the last vehicle. Region 3, however, has been half completed by the first vehicle. Thus, as displayed in Fig. 32, the occupied lengths of regions 1–3 at the end of time-slice 0 / beginning of time-slice 1 are $1 \times 6 = 6$, $1 \times 4 = 4$, and $\frac{1}{2} \times 4 = 2$, respectively. Splitting the r-path flow across the regions according to their occupied lengths, $\frac{6}{6+4+2} = \frac{1}{2}$ of the flow is in region 1, $\frac{4}{6+4+2} = \frac{1}{3}$ of the flow is in region 2, and $\frac{2}{6+4+2} = \frac{1}{6}$ of the flow is in region 3. At different moments in time, one can thus work out the contributing accumulations from this regional path flow in each of the regions.

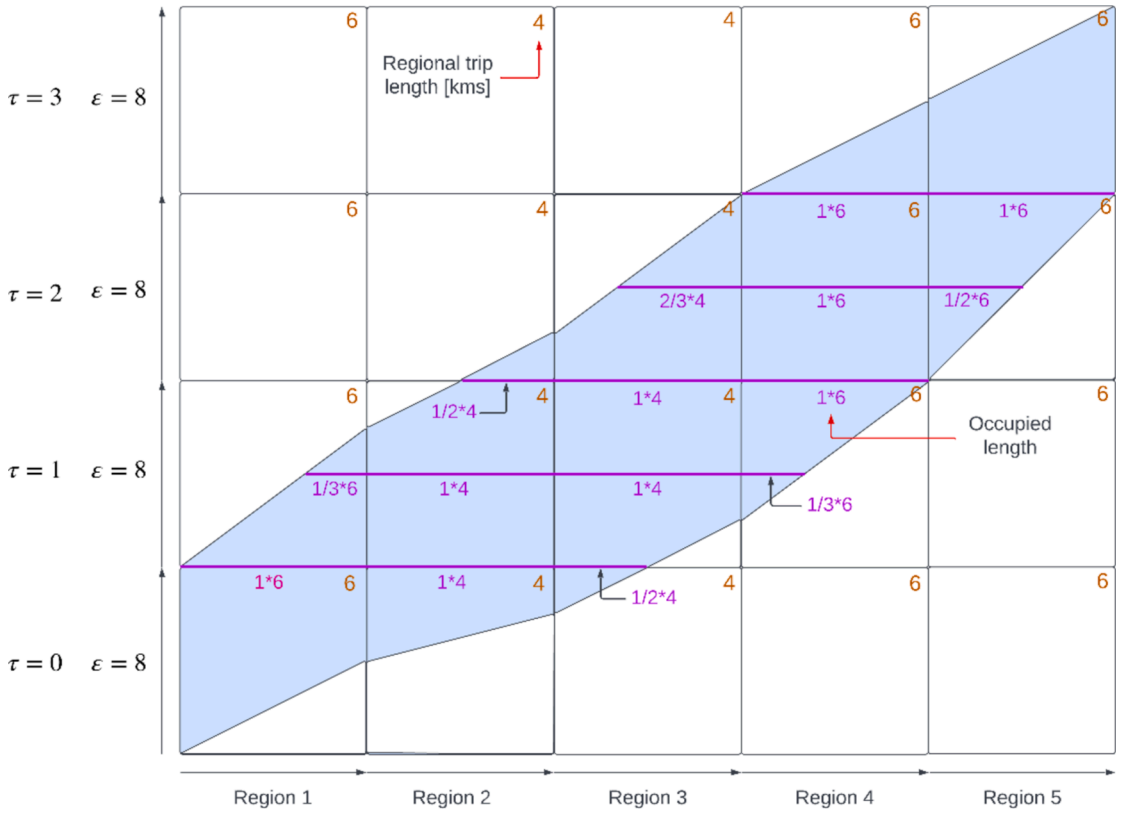

Fig. 32. Illustrating occupied lengths of regions from a regional path flow at different moments in time.

Since MFDs operate in terms of estimating the space-mean speed of vehicles in a region given an accumulation level at a given moment in time, to obtain the average speed of vehicles in a region during a time-slice, one would ideally take a large (or infinite) number of draws of accumulation levels at different moments in time throughout the time-slice (summing the accumulation contributions from all r-path flows), input these accumulation levels into the speed-MFD function to determine the speeds at these moments in time, and then take an average. However, taking a sufficient number of draws to get a reasonably accurate average would be very computationally burdensome. Taking draws of accumulation levels at moments in time not at the beginning or end of a time-slice is not straightforward, and one would have to do this for every departing flow for every regional path, many times. Moreover, it is possible to completely miss the contributing accumulation of a flow in a region, by the flow passing between two accumulation draws, as depicted in Fig. 33.

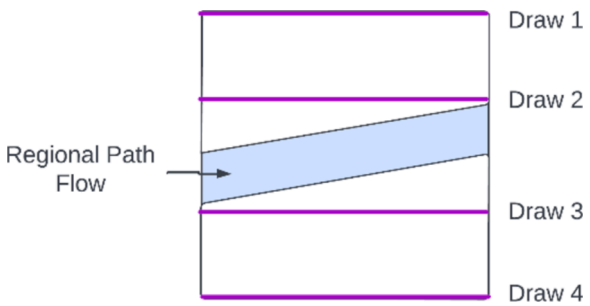

Fig. 33. Illustrating how a regional path flow can be completely missed when taking draws of accumulation levels.

We therefore adopt a more computationally efficient and rigorous approach. We instead neatly use the occupying areas of the r-path flow in each region at each time-slice in the STG, to work out the average accumulation in a region over the time-slice. This average accumulation level is then inputted into the speed-MFD function to approximate the average speed in the region during the time-slice. The more fine-grained the time-slice grain is, the better the approximation. For example, accumulation levels are likely to vary less at a time-slice grain of 5 min compared to 30 min.

Now, if one were to take an infinite number of draws of the occupied lengths at every moment of time during a time-slice, one could

consequently work out the region accumulations at every moment in time and take an average to obtain the average accumulation level. However, rather than taking an infinite number of draws of the occupied lengths, one can instead use the occupying areas of the r-path flow. A neat property of the STG is that, from the flow of an r-path, the contributing average accumulation in each of the r-path's regions during a time-slice, can be calculated by proportioning the r-path flow between the regions in the r-path according to its proportional occupying STG area for that time-slice, weighted by region length.

To demonstrate, Fig. 34 displays in red the proportional occupying STG areas of the r-path flow in the regions at time-slices 1 & 2, weighted by region length. Calculating the proportional occupying STG areas is a matter of calculating simple triangles and trapeziums. For example, the proportional occupying area of region 1 time-slice 1 is calculated by calculating the area of the bottom right triangle: $\frac{1\times 0.75}{2} = 0.375$, the area for region 3 time-slice 2 is calculated by calculating the area of the trapezium: $1 \times \frac{0.25+1}{2} = 0.625$, and the area for regions 2 & 3 time-slice 1 are calculated by taking out the areas of the top left / bottom right triangles: $1 \times 1 - \frac{0.5\times 0.25}{2} = 0.9375$.

Suppose that the flow travelling this r-path departing at time-slice 0 is 100. From this flow of vehicles, the contributing average accumulations in regions 1–4 during time-slice 1 are, respectively, as follows: $100 \times \frac{6\times 0.375}{6\times 0.375+4\times 0.9375+4\times 0.9375+6\times 0.375} = 18.75$, $100 \times \frac{4\times 0.9375}{6\times 0.375+4\times 0.9375+4\times 0.9375+6\times 0.375} = 31.25$, $100 \times \frac{4\times 0.9375}{6\times 0.375+4\times 0.9375+4\times 0.9375+6\times 0.375} = 31.25$, $100 \times \frac{6\times 0.375}{6\times 0.375+4\times 0.9375+4\times 0.9375+6\times 0.375} = 18.75$. So, on average, 18.75, 31.25, 31.25, & 18.75 vehicles were in regions 1–4 during time-slice 1, from the flow travelling this r-path departing at time-slice 0.

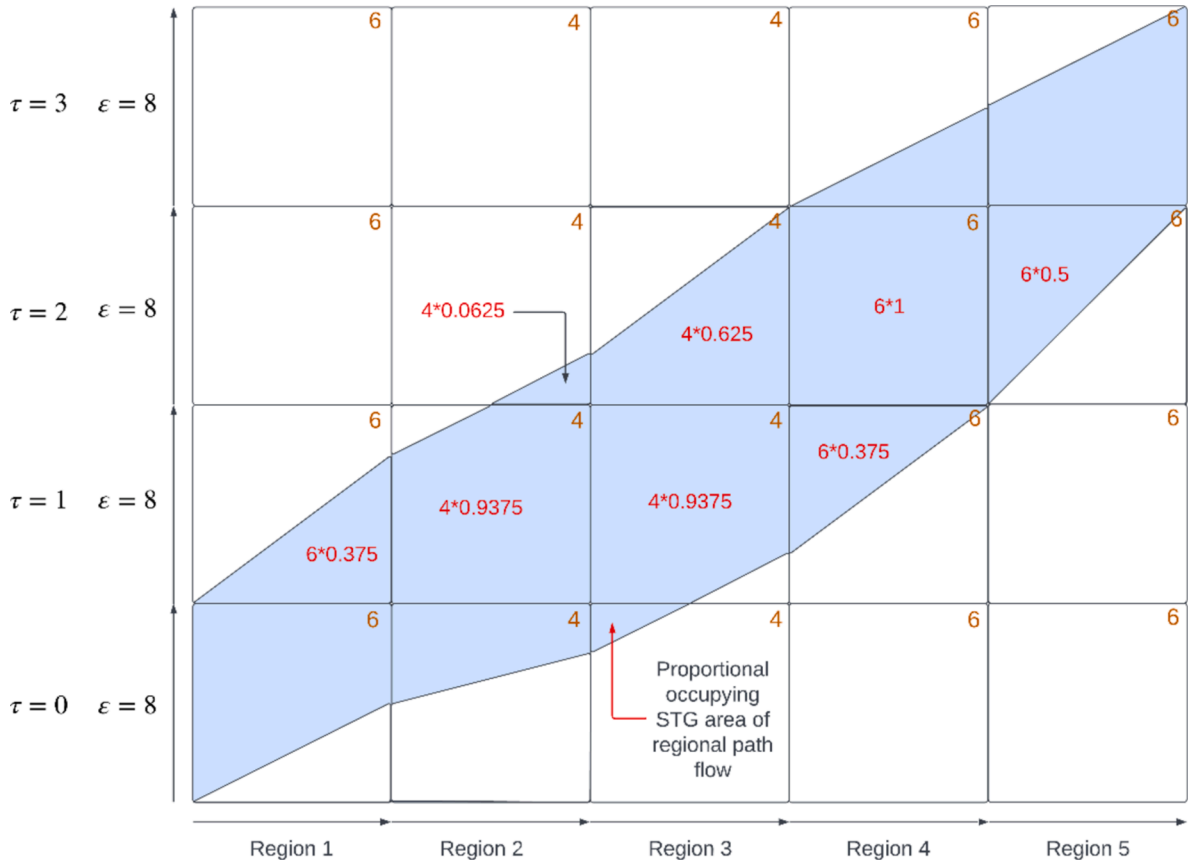

Fig. 34. Illustrating proportional occupying STG areas of r-path flow in regions, weighted by region length.

To be able to calculate the contributing average accumulations in the r-path's regions during time-slices in which flow departs/destinates (in this case time-slices 0 & 3), one extends the STG by adding pseudo-regions with the same properties of the first/last regions in the r-path. These represent origin/destination connectors. They could be represented as single connector regions with appropriately adapted regional trip lengths to fit the occupying flow within the region, but it is simpler to extend the graph with multiple pseudo-regions with the same region travel time as the first/last regions. Fig. 35 displays such extension of the STG for the 5-region r-path, as well as the proportional occupying STG areas for time-slices 0 & 3, weighted by region length.

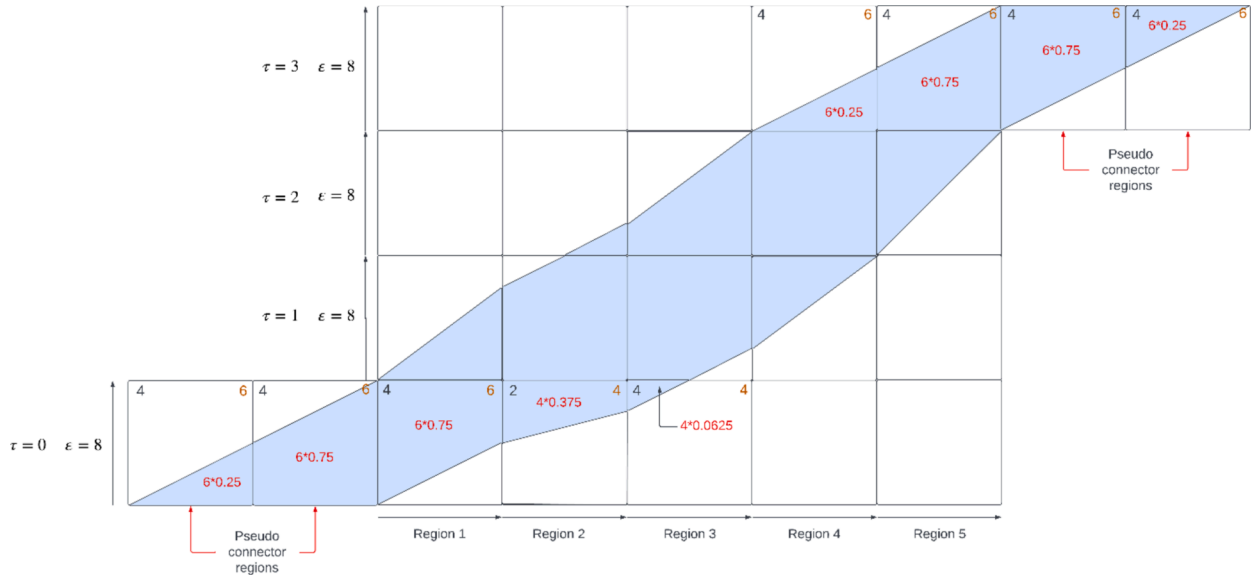

Fig. 35. Illustrating how the STG is extended with pseudo-regions to represent connectors be able to calculate average region accumulations during time-slices where flow departs/destinates.

To obtain the total average accumulation level in a region during a time-slice, one sums up the average accumulations from all r-path flows. This average accumulation level is then inserted into the speed-MFD function to obtain the average speed being travelled in the region during the time-slice. This average speed is then used to update the region travel times. Once updating all region travel times for all r-paths for all time-slices, the STG traffic propagation tracking is conducted again outputting new average region accumulation levels, and so on until an equilibrium is reached.

Appendix C. Calculating proportional occupying STG areas

In this section, we detail how to calculate proportional occupying STG areas in equation (3).

C.1. Tracking vehicle trajectories on STG

First, in order to be able to calculate the proportional occupying STG areas, one needs to track the trajectories of the first and last vehicles departing at the beginning/end of time-slice τ' travelling r-path $p \in P_m$, noting that the trajectory of the last vehicle departing at the end of time-slice τ' is the same as the trajectory of the first vehicle departing at the beginning time-slice $\tau' + 1$. To do this, we define the following:

- $r_{m,p}^{\tau' \to \tau}$ is the *transition region* that is traversed but not completed during τ, by the first vehicle that departs at the beginning of time-slice τ' travelling r-path $p \in P_m$.
- $\mu_{m,p,k}^{\tau' \to \tau}$ is the *first exit proportion* that gives the proportion into time-slice τ that the first vehicle departing at the beginning of time-slice τ' travelling r-path $p \in P_m$ exits region k.
- $\alpha_{m,p,k}^{\tau' \to \tau}$ is the *completed proportion* that gives the proportion of region k that is completed during time-slice τ, by the first vehicle that departs at the beginning of time-slice τ' travelling r-path $p \in P_m$.

These three concepts are demonstrated in Fig. 36, for the first vehicles departing at the beginning of time-slices 0 and 1, travelling r-path 1 of OD movement 1. As shown, region 3 is the transition region for the first vehicle departing at the beginning of time-slice 0, in which the region is traversed in during time-slice 0 but not completed before the end of the time-slice ($r_{1,1}^{0 \to 0} = 3$). The other transition regions are regions 2 and 3 for the first vehicle departing at the beginning of time-slice 1, traversed but not completed by the end of time-slices 1 and 2, respectively, ($r_{1,1}^{1 \to 1} = 2$, $r_{1,1}^{1 \to 2} = 3$).

For the first vehicle departing at the beginning of time-slice 0, the proportions into time-slice 0 it exits regions 1 & 2 are $\mu_{1,1,1}^{0 \to 0} = \frac{1}{2}$ and $\mu_{1,1,2}^{0 \to 0} = \frac{3}{4}$, respectively. The proportion into time-slice 1 it exits region 3 is $\mu_{1,1,3}^{0 \to 1} = \frac{1}{4}$. For the first vehicle departing at the beginning of time-slice 1, the proportions into time-slices 1 & 2 it exits regions 2 & 3 are $\mu_{1,1,1}^{1 \to 1} = \frac{3}{4}$ and $\mu_{1,1,2}^{1 \to 2} = \frac{1}{4}$, respectively.

For the first vehicle departing at the beginning of time-slice 0, the proportion of the transition region (region 3) that is completed

during time-slice 0 is $\alpha_{1,1,3}^{0\to0} = \frac{1}{2}$. For the first vehicle departing at the beginning of time-slice 1, the proportions of the transition regions (regions 2 & 3) that are completed during time-slices 1 & 2 are $\alpha_{1,1,2}^{1\to1} = \frac{1}{2}$ and $\alpha_{1,1,3}^{1\to2} = \frac{3}{4}$, respectively.

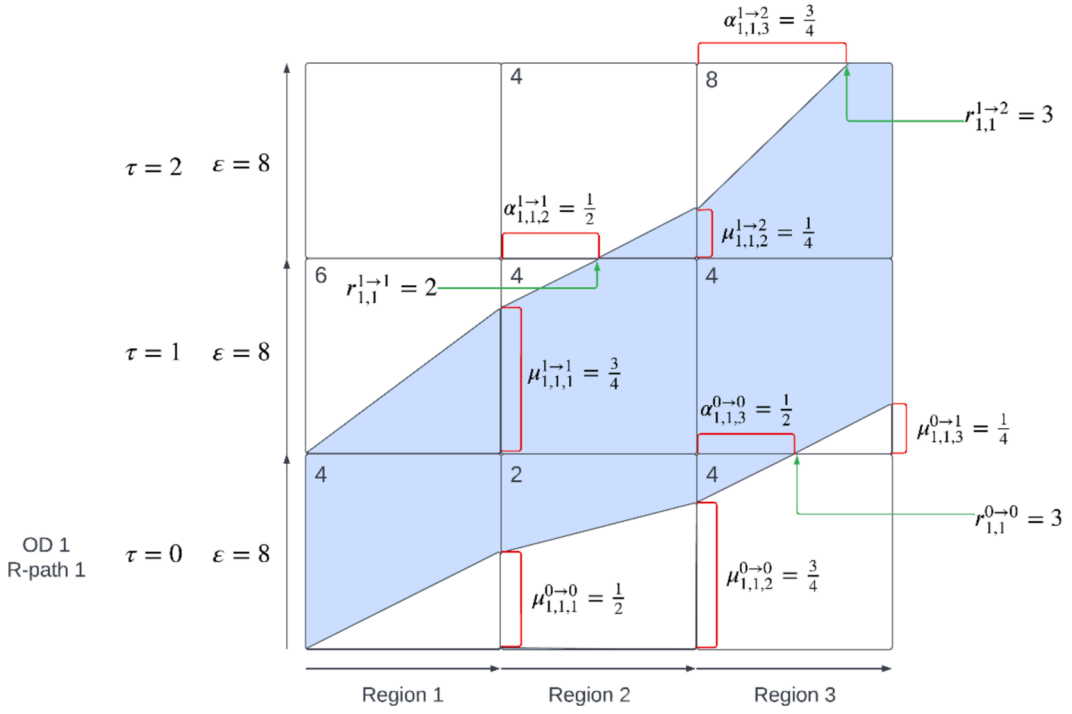

Fig. 36. Illustrating the concepts of transition region ($r_{m,p}^{\tau\to\tau'}$), first exit proportion ($\mu_{m,p,k}^{\tau\to\tau'}$), and completed proportion ($\alpha_{m,p,k}^{\tau\to\tau'}$), for tracking the trajectory of the first vehicle departing at the beginning of time-slice τ.

We now provide and demonstrate the formulas for calculating completed proportions and first exit proportions. First, define the following:

- $R_{m,p}^{r\leftrightarrow k}$ is the set of regions between and including regions r and k in r-path $p \in P_m$.
- $r_{m,p}^{\tau\to\tau',-}$ is the region immediately preceding region $r_{m,p}^{\tau\to\tau'}$ in r-path $p \in P_m$.
- $r_{m,p}^{\tau\to\tau',+}$ is the region immediately succeeding region $r_{m,p}^{\tau\to\tau'}$ in r-path $p \in P_m$.
- $r_{m,p}^{min}$ is the first region in r-path $p \in P_m$.

These are demonstrated in Fig. 37. Region 1 is the first region in the r-path ($r_{m,p}^{0} = 1$). Region 3 is the transition region ($r_{1,1}^{0\to0} = 3$), and regions 2&4 are the regions preceding and succeeding the transition region ($r_{1,1}^{0\to0,-} = 2$, $r_{1,1}^{0\to0,+} = 4$). The set of regions between regions 2&4 is $R_{1,1}^{2\leftrightarrow4} = \{2,3,4\}$.

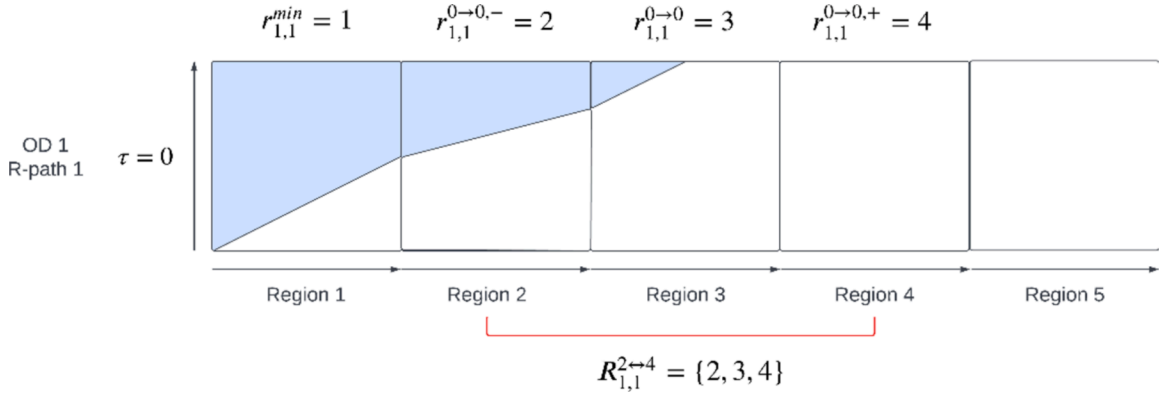

Fig. 37. Illustrating other notation for tracking the trajectory of the first vehicle departing at the beginning of time-slice τ.

We begin with formulating the completed proportions. Note that we are only interested in computing the completed proportions for transition regions.

Completed proportion: the proportion of region k that is completed during time-slice τ', by the first vehicle that departs at the beginning of time-slice τ travelling r-path $p \in P_m$, is calculated as follows:

$$\alpha^{\tau\to\tau'}_{m,p,k} = \begin{cases} \dfrac{\varepsilon - \sum_{s\in R^{r^{min}_{m,p}\leftrightarrow r^{\tau\to\tau',-}_{m,p}}_{m,p}} t^{\tau'}_{m,p,s}}{t^{\tau'}_{m,p,r^{\tau\to\tau'}_{m,p}}} & \text{if } \tau = \tau' \\ \dfrac{\varepsilon - t^{\tau'}_{m,p,r^{\tau\to\tau'}_{m,p}-1}\left(1-\alpha^{\tau\to\tau'-1}_{m,p,r^{\tau\to\tau'}_{m,p}-1}\right) - \sum_{s\in R^{r^{\tau\to\tau'}_{m,p}-1,+}_{m,p}\leftrightarrow r^{\tau\to\tau',-}_{m,p}} t^{\tau'}_{m,p,s}}{t^{\tau'}_{m,p,r^{\tau\to\tau'}_{m,p}}} & \text{otherwise} \end{cases}.$$

First, consider the case where $\tau = \tau'$. Fig. 38 demonstrates how a completed proportion is calculated in this case. Region $r^{min}_{1,1} = 1$ is the first region in the r-path and region $r^{0\to0,-}_{1,1} = 2$ is the region preceding the transition region ($r^{0\to0}_{1,1} = 3$). $R^{r^{min}_{1,1}\leftrightarrow r^{0\to0,-}_{1,1}}_{1,1}$ is thus the set of regions between and including regions 1 & 2: $R^{1\leftrightarrow2}_{1,1} = \{1,2\}$. $\sum_{s\in\{1,2\}} t^0_{1,1,s} = 4+2 = 6$ is thus the sum of the travel times of these regions. $\varepsilon - \sum_{s\in\{1,2\}} t^0_{1,1,s} = 8-6 = 2$ is the remaining travel time in the time-slice after the first departing vehicle has completed the preceding regions to the transition region, which is therefore the completed travel time of the transition region. 2 min of the transition region have been completed out of $t^0_{1,1} = 4$ minutes, and thus the completed proportion is $\alpha^{0\to0}_{1,1,3} = \frac{2}{4} = \frac{1}{2}$.

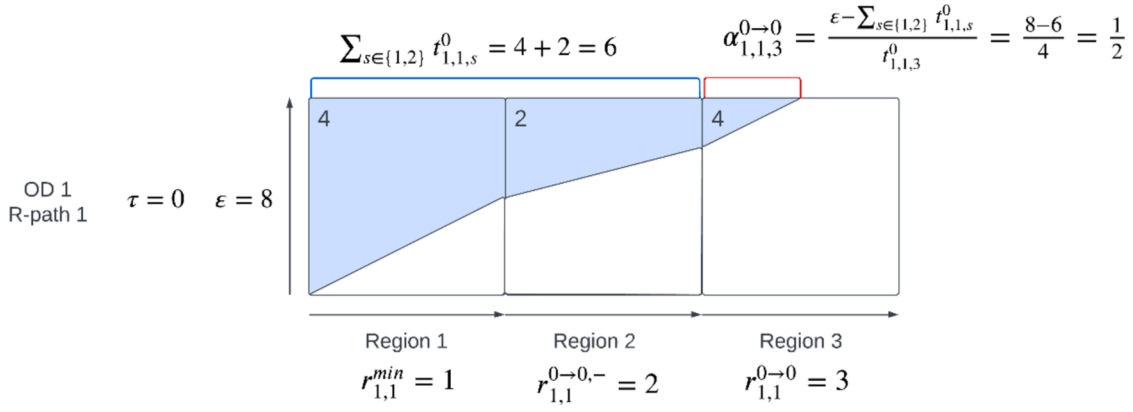

Fig. 38. Demonstrating the calculation of completed proportions ($\alpha^{\tau\to\tau'}_{m,p,k}$) when $\tau = \tau'$.

Next consider the case where $\tau \neq \tau'$. Fig. 39 demonstrates how a completed proportion is calculated in this case. The transition region that the first vehicle departing at the beginning of time-slice 0 traverses but does not complete during time-slice 0 is $r^{0\to0}_{1,1} = 1$. The completed proportion of this region is $\alpha^{0\to0}_{1,1,1} = \frac{1}{2}$. This means that $t^{0\to0}_{1,1,1}\left(1-\alpha^{0\to0}_{1,1,1}\right) = 8\times\frac{1}{2} = 4$ minutes remains to be completed in time-slice 1. $r^{0\to1}_{1,1} = 3$ is the transition region for time-slice 1. The set of regions between and including the region succeeding the transition region for time-slice 0 ($r^{0\to0,+}_{1,1} = 2$) and the region preceding the transition region for time-slice 1 ($r^{0\to1,-}_{1,1} = 2$) is $R^{r^{0\to0,+}_{1,1}\leftrightarrow r^{0\to1,-}_{1,1}}_{1,1} = \{2\}$. The sum of the travel times of these regions is $\sum_{s\in\{2\}} t^1_{1,1,s} = 2$. $\varepsilon - t^{0\to0}_{1,1,1}\left(1-\alpha^{0\to0}_{1,1,1}\right) - \sum_{s\in\{2\}} t^1_{1,1,s} = 8-4-2 = 2$ is therefore the completed travel time of the transition region during time-slice 1. 2 min of the transition region have been completed out of $t^1_{1,1} = 6$ minutes, and thus the completed proportion is $\alpha^{0\to1}_{1,1,3} = \frac{2}{6} = \frac{1}{3}$.

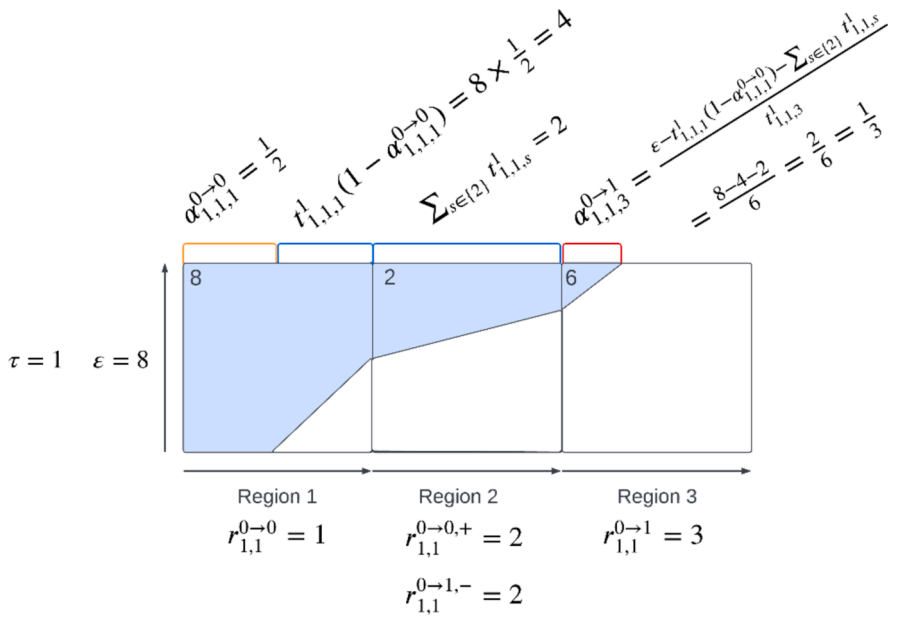

Fig. 39. Demonstrating the calculation of completed proportions ($\alpha^{\tau\to\tau'}_{m,p,k}$) when $\tau \neq \tau'$.

Next, we formulate the first exit proportions.

First exit proportion: the proportion into time-slice τ' that the first vehicle departing at the beginning of time-slice τ travelling r-path $p \in P_m$ exits region k, is calculated as follows:

$$\mu^{\tau\to\tau'}_{m,p,k} = \begin{cases} \dfrac{\sum_{s\in R^{r^{min}_{m,p}\leftrightarrow k}_{m,p}} t^{\tau'}_{m,p,s}}{\varepsilon} & \text{if } \tau = \tau' \\ \dfrac{t^{\tau'}_{m,p,r^{\tau\to\tau'-1}_{m,p}}\left(1-\alpha^{\tau\to\tau'}_{m,p,r^{\tau\to\tau'-1}_{m,p}}\right)}{\varepsilon} & \text{if } \tau \neq \tau' \text{ and } k = r^{\tau\to\tau'-1}_{m,p}, \quad \forall k \in R^{r^{\tau\to\tau'-1}_{m,p}\leftrightarrow r^{\tau\to\tau'-}_{m,p}}_{m,p}. \\ \dfrac{t^{\tau'}_{m,p,r^{\tau\to\tau'-1}_{m,p}}\left(1-\alpha^{\tau\to\tau'}_{m,p,r^{\tau\to\tau'-1}_{m,p}}\right) + \sum_{s\in R^{r^{\tau\to\tau'-1,+}_{m,p}\leftrightarrow k}_{m,p}} \frac{t^{\tau'}_{m,p,s}}{\varepsilon}}{\varepsilon} & \text{if } \tau \neq \tau' \text{ and } k \neq r^{\tau\to\tau'-1}_{m,p} \end{cases}$$

First, consider the case where $\tau = \tau'$. Fig. 40 demonstrates how a first exit proportion is calculated in this case. Region $r^{min}_{1,1} = 1$ is the first region in the r-path and the region we are calculating the first exit proportion for is region $k = 2$. $R^{r^{min}_{m,p}\leftrightarrow k}_{1,1} = R^{1\leftrightarrow 2}_{1,1} = \{1,2\}$ is the set of regions between and including regions $r^{min}_{1,1} = 1$ and $k = 2$. $\sum_{s\in R^{1\leftrightarrow 2}_{1,1}} t^0_{1,1,s} = 4+2 = 6$ is the sum of the travel times of these regions. In the case where $\tau = \tau'$, the first exit proportion of region k is the travel time of region k plus the sum of the travel times of the preceding regions to k, out of the time-slice duration: $\frac{\sum_{s\in R^{1\leftrightarrow 2}_{1,1}} t^0_{1,1,s}}{\varepsilon} = \frac{6}{8} = \frac{3}{4}$.

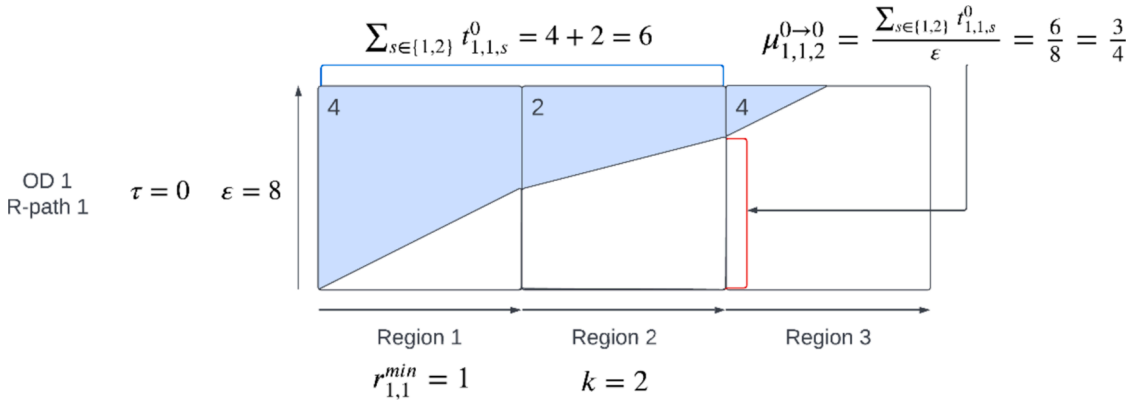

Fig. 40. Demonstrating the calculation of first exit proportions ($\mu^{\tau\to\tau'}_{m,p,k}$) when $\tau = \tau'$.

Next consider the case where $\tau \neq \tau'$ and $k = r^{\tau\to\tau'-1}_{m,p}$. Fig. 41 demonstrates how a first exit proportion is calculated in this case, where region k is the transition region from the previous time-slice, i.e. in the example $k = r^{0\to0}_{1,1} = 1$. $\alpha^{0\to0}_{1,1} = \frac{1}{2}$ is the completed proportion of region 1, and therefore $t^1_{1,1}\left(1-\alpha^{0\to0}_{1,1}\right) = 8\times\frac{1}{2} = 4$ is the travel time remaining. The first exit proportion of region k is this remaining travel time out of the time-slice duration: $\frac{t^1_{1,1}\left(1-\alpha^{0\to0}_{1,1}\right)}{\varepsilon} = \frac{4}{8} = \frac{1}{2}$.

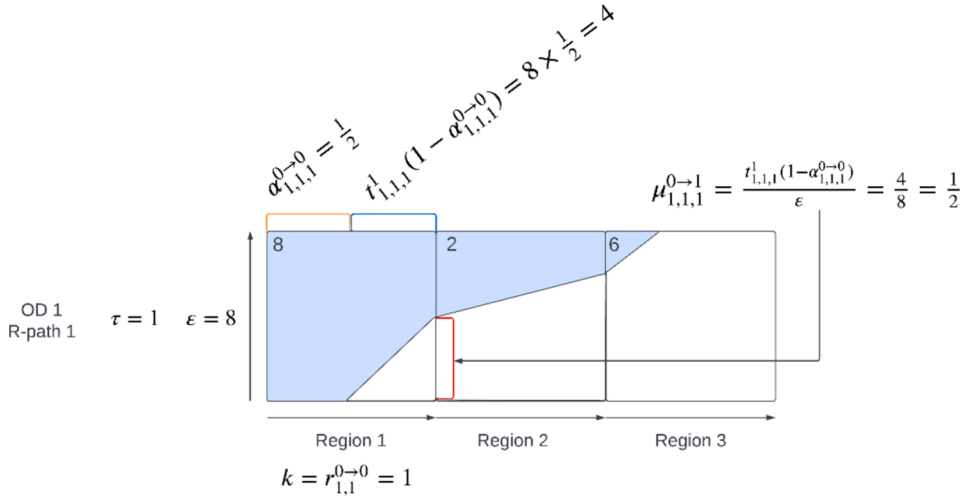

Fig. 41. Demonstrating the calculation of first exit proportions ($\mu^{\tau\to\tau'}_{m,p,k}$) when $\tau \neq \tau'$ and $k = r^{\tau\to\tau'-1}_{m,p}$.

Lastly, consider the case where $\tau \neq \tau'$ and $k \neq r^{\tau\to\tau'-1}_{m,p}$. Fig. 42 demonstrates how a first exit proportion is calculated in this case. Region $r^{0\to0}_{1,1} = 1$ is the transition region from the previous time-slice ($\tau = 0$) and $k = 2$. In the case where $\tau \neq \tau'$ and $k \neq r^{\tau\to\tau'-1}_{m,p}$, the first exit proportion for region k is the remaining travel time of the transition region ($t^1_{1,1}\left(1-\alpha^{0\to0}_{1,1}\right) = 8\times\frac{1}{2} = 4$) plus the sum of the travel times of the regions between and including the region succeeding the transition region ($r^{0\to0,+}_{1,1} = 2$) and region $k = 2$, $\sum_{s\in\{2\}} t^0_{1,1,s}$, out of the time-slice duration: $\frac{t^1_{1,1}\left(1-\alpha^{0\to0}_{1,1}\right)+\sum_{s\in\{2\}} t^0_{1,1,s}}{\varepsilon} = \frac{4+2}{8} = \frac{3}{4}$.

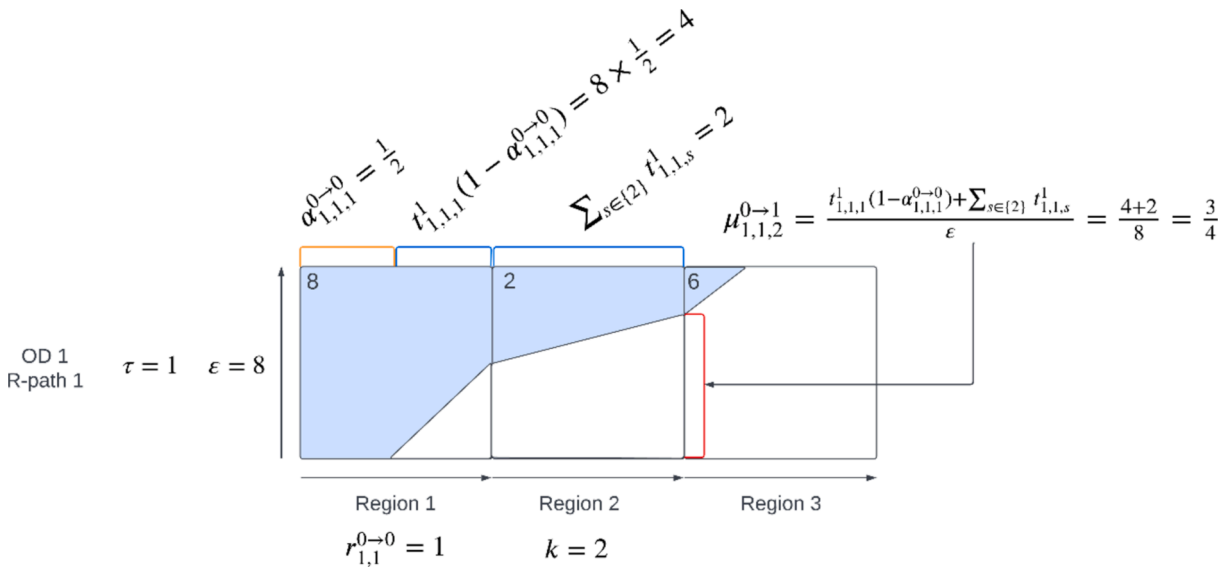

Fig. 42. Demonstrating the calculation of first exit proportions ($\mu^{\tau\to\tau'}_{m,p,k}$) when $\tau \neq \tau'$ and $k = r^{\tau\to\tau'-1}_{m,p}$.

C.2. Formulas for calculating the different possible areas

In this section, we detail all 25 possibilities for the proportional occupying STG areas, with demonstrations, and provide the formulas for calculating the area. The 25 possibilities are as follows:

Possibility 1: $r = r^{min}_{m,p}$, $\tau' = \tau$, and $r \neq r^{\tau'\to\tau}_{m,p}$.

$$A^{\tau'\to\tau}_{m,p,r} = 1 - 0.5 \bullet 1 \bullet \mu^{\tau'\to\tau}_{m,p,r}$$

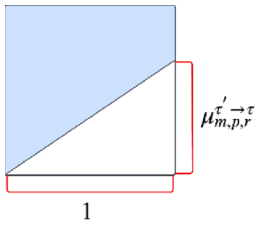

Possibility 2: $r = r^{min}_{m,p}$, $\tau' - 1 = \tau$, $r \neq r^{\tau'\to\tau-1}_{m,p}$, $r \neq r^{\tau'\to\tau}_{m,p}$, and $r \neq r^{\tau'+1\to\tau}_{m,p}$.

$$A^{\tau'\to\tau}_{m,p,r} = 0.5 \bullet 1 \bullet \mu^{\tau'+1\to\tau}_{m,p,r}$$

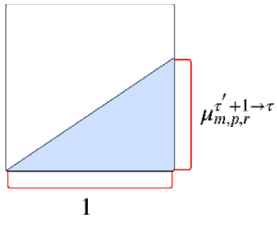

Possibility 3: $r = r^{min}_{m,p}$, $\tau' = \tau$, and $r = r^{\tau'\to\tau}_{m,p}$.

$$A^{\tau'\to\tau}_{m,p,r} = 0.5 \bullet 1 \bullet \alpha^{\tau'\to\tau}_{m,p,r}$$

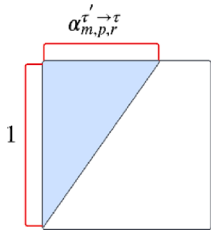

Possibility 4: $r = r_{m,p}^{min}$, $\tau' - 1 = \tau$, $r \neq r_{m,p}^{\tau' \to \tau - 1}$, $r \neq r_{m,p}^{\tau' \to \tau}$, and $r = r_{m,p}^{\tau' + 1 \to \tau}$.

$$A_{m,p,r}^{\tau' \to \tau} = 1 - 0.5 \bullet 1 \bullet \alpha_{m,p,r}^{\tau' + 1 \to \tau}$$

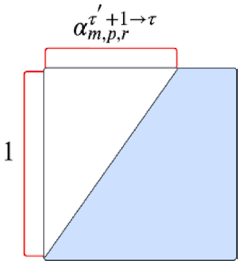

Possibility 5: $r = r_{m,p}^{min}$, $\tau' - 1 = \tau$, $r = r_{m,p}^{\tau' \to \tau - 1}$, $r \neq r_{m,p}^{\tau' \to \tau}$, and $r = r_{m,p}^{\tau' + 1 \to \tau}$.

$$A_{m,p,r}^{\tau' \to \tau} = 1 - 0.5 \bullet 1 \bullet \alpha_{m,p,r}^{\tau' + 1 \to \tau} - 0.5 \bullet \left(1 - \alpha_{m,p,r}^{\tau' \to \tau - 1}\right) \bullet \mu_{m,p,r}^{\tau' \to \tau}$$

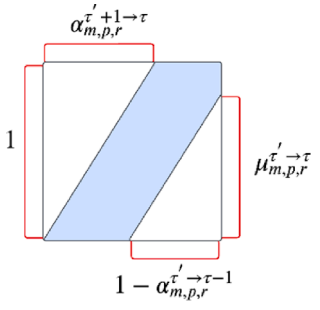

Possibility 6: $r = r_{m,p}^{min}$, $\tau' - 1 = \tau$, $r = r_{m,p}^{\tau' \to \tau - 1}$, $r = r_{m,p}^{\tau' \to \tau}$, and $r = r_{m,p}^{\tau' + 1 \to \tau}$.

$$A_{m,p,r}^{\tau' \to \tau} = 1 - 0.5 \bullet 1 \bullet \alpha_{m,p,r}^{\tau' + 1 \to \tau} - 0.5 \bullet \left(\left(1 - \alpha_{m,p,r}^{\tau' \to \tau - 1}\right) + \left(1 - \alpha_{m,p,r}^{\tau' \to \tau}\right)\right)$$

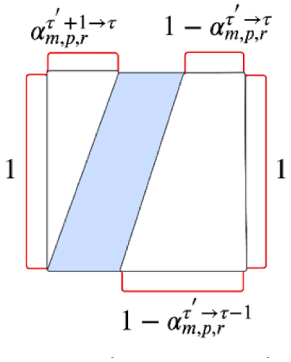

Possibility 7: $r = r_{m,p}^{min}$, $\tau' - 1 = \tau$, $r = r_{m,p}^{\tau'\to\tau-1}$, $r \neq r_{m,p}^{\tau'\to\tau}$, and $r \neq r_{m,p}^{\tau'+1\to\tau}$.

$$A_{m,p,r}^{\tau'\to\tau} = 0.5 \bullet 1 \bullet \mu_{m,p,r}^{\tau'+1\to\tau} - 0.5 \bullet \left(1 - \alpha_{m,p,r}^{\tau'\to\tau-1}\right) \bullet \mu_{m,p,r}^{\tau'\to\tau}$$

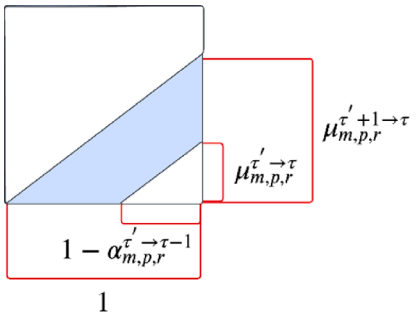

Possibility 8: $r \neq r_{m,p}^{min}$, $\tau = \min\left(\tau'' : \tau'' \in \Psi_{m,p}^{\tau'}\right)$, $\tau \neq \max\left(\tau'' : \tau'' \in \Psi_{m,p}^{\tau'}\right)$, $r \neq r_{m,p}^{\tau'\to\tau}$, and $r \neq r_{m,p}^{\tau'+1\to\tau}$.

$$A_{m,p,r}^{\tau'\to\tau} = 1 - 0.5 \bullet \left(\mu_{m,p,r}^{\tau'\to\tau} + \mu_{m,p,r-}^{\tau'\to\tau}\right)$$

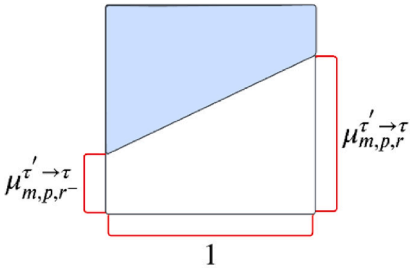

Possibility 9: $r \neq r_{m,p}^{min}$, $\tau \neq \min\left(\tau'' : \tau'' \in \Psi_{m,p}^{\tau'}\right)$, $\tau = \max\left(\tau'' : \tau'' \in \Psi_{m,p}^{\tau'}\right)$, $r \neq r_{m,p}^{\tau'\to\tau-1}$, and $r \neq r_{m,p}^{\tau'+1\to\tau-1}$.

$$A_{m,p,r}^{\tau'\to\tau} = 0.5 \bullet \left(\mu_{m,p,r}^{\tau'+1\to\tau} + \mu_{m,p,r-}^{\tau'+1\to\tau}\right)$$

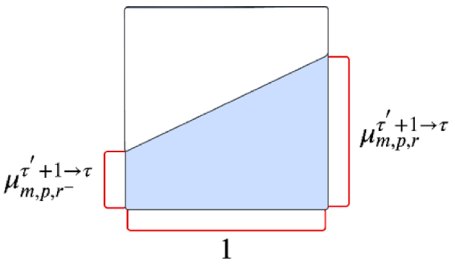

Possibility 10: $r \neq r^{min}_{m,p}$, $\tau = \min\left(\tau'' : \tau'' \in \Psi^{\tau'}_{m,p}\right)$, $\tau \neq \max\left(\tau'' : \tau'' \in \Psi^{\tau'}_{m,p}\right)$, $r = r^{\tau'\to\tau}_{m,p}$, and $r \neq r^{\tau'+1\to\tau}_{m,p}$.

$$A^{\tau'\to\tau}_{m,p,r} = 0.5 \bullet \left(1 - \mu^{\tau'\to\tau}_{m,p,r^-}\right) \bullet \alpha^{\tau'\to\tau}_{m,p,r}$$

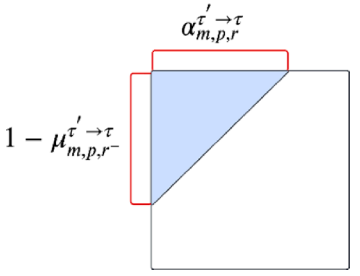

Possibility 11: $r \neq r^{min}_{m,p}$, $\tau \neq \min\left(\tau'' : \tau'' \in \Psi^{\tau'}_{m,p}\right)$, $\tau \neq \max\left(\tau'' : \tau'' \in \Psi^{\tau'}_{m,p}\right)$, $r \neq r^{\tau'\to\tau-1}_{m,p}$, $r \neq r^{\tau'\to\tau}_{m,p}$, $r \neq r^{\tau'+1\to\tau-1}_{m,p}$, and $r = r^{\tau'+1\to\tau}_{m,p}$.

$$A^{\tau'\to\tau}_{m,p,r} = 1 - 0.5 \bullet \left(1 - \mu^{\tau'+1\to\tau}_{m,p,r^-}\right) \bullet \alpha^{\tau'+1\to\tau}_{m,p,r}$$

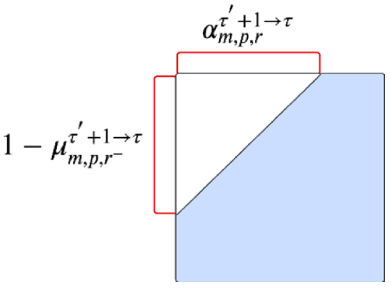

Possibility 12: $r \neq r^{min}_{m,p}$, $\tau \neq \min\left(\tau'' : \tau'' \in \Psi^{\tau'}_{m,p}\right)$, $\tau \neq \max\left(\tau'' : \tau'' \in \Psi^{\tau'}_{m,p}\right)$, $r = r^{\tau'\to\tau-1}_{m,p}$, $r \neq r^{\tau'\to\tau}_{m,p}$, $r \neq r^{\tau'+1\to\tau-1}_{m,p}$, and $r \neq r^{\tau'+1\to\tau}_{m,p}$.

$$A^{\tau'\to\tau}_{m,p,r} = 1 - 0.5 \bullet \left(1 - \alpha^{\tau'\to\tau-1}_{m,p,r}\right) \bullet \mu^{\tau'\to\tau}_{m,p,r}$$

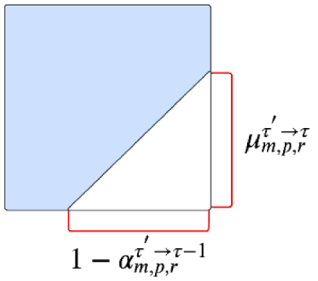

Possibility 13: $r \neq r^{min}_{m,p}$, $\tau \neq \min\left(\tau'' : \tau'' \in \Psi^{\tau'}_{m,p}\right)$, $\tau = \max\left(\tau'' : \tau'' \in \Psi^{\tau'}_{m,p}\right)$, $r \neq r^{\tau' \to \tau-1}_{m,p}$, and $r = r^{\tau'+1 \to \tau-1}_{m,p}$.

$$A^{\tau' \to \tau}_{m,p,r} = 0.5 \bullet \left(1 - \alpha^{\tau'+1 \to \tau-1}_{m,p,r}\right) \bullet \mu^{\tau'+1 \to \tau}_{m,p,r}$$

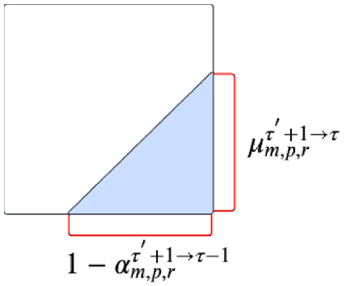

Possibility 14: $r \neq r^{min}_{m,p}$, $\tau \neq \min\left(\tau'' : \tau'' \in \Psi^{\tau'}_{m,p}\right)$, $\tau \neq \max\left(\tau'' : \tau'' \in \Psi^{\tau'}_{m,p}\right)$, $r = r^{\tau' \to \tau-1}_{m,p}$, $r = r^{\tau' \to \tau}_{m,p}$, $r \neq r^{\tau'+1 \to \tau-1}_{m,p}$, and $r \neq r^{\tau'+1 \to \tau}_{m,p}$.

$$A^{\tau' \to \tau}_{m,p,r} = 0.5 \bullet \left(\alpha^{\tau' \to \tau-1}_{m,p,r} + \alpha^{\tau' \to \tau}_{m,p,r}\right)$$

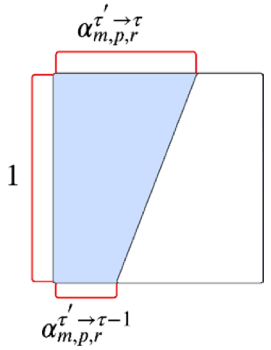

Possibility 15: $r \neq r^{min}_{m,p}$, $\tau \neq \min\left(\tau'' : \tau'' \in \Psi^{\tau'}_{m,p}\right)$, $\tau \neq \max\left(\tau'' : \tau'' \in \Psi^{\tau'}_{m,p}\right)$, $r \neq r^{\tau' \to \tau-1}_{m,p}$, $r \neq r^{\tau' \to \tau}_{m,p}$, $r = r^{\tau'+1 \to \tau-1}_{m,p}$, and $r = r^{\tau'+1 \to \tau}_{m,p}$.

$$A^{\tau' \to \tau}_{m,p,r} = 1 - 0.5 \bullet \left(\alpha^{\tau'+1 \to \tau-1}_{m,p,r} + \alpha^{\tau'+1 \to \tau}_{m,p,r}\right)$$

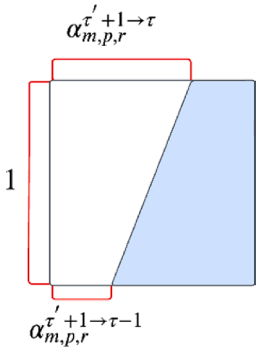

Possibility 16: $r \neq r_{m,p}^{min}$, $\tau \neq \min\left(\tau'' : \tau'' \in \Psi_{m,p}^{\tau'}\right)$, $\tau \neq \max\left(\tau'' : \tau'' \in \Psi_{m,p}^{\tau'}\right)$, $r = r_{m,p}^{\tau'\to\tau-1}$, $r \neq r_{m,p}^{\tau'\to\tau}$, $r \neq r_{m,p}^{\tau'+1\to\tau-1}$, and $r = r_{m,p}^{\tau'+1\to\tau}$.

$$A_{m,p,r}^{\tau'\to\tau} = 1 - 0.5 \bullet \left(1 - \mu_{m,p,r^-}^{\tau'+1\to\tau}\right) \bullet \alpha_{m,p,r}^{\tau'+1\to\tau} - 0.5 \bullet \mu_{m,p,r}^{\tau'\to\tau} \bullet \left(1 - \alpha_{m,p,r}^{\tau'\to\tau-1}\right)$$

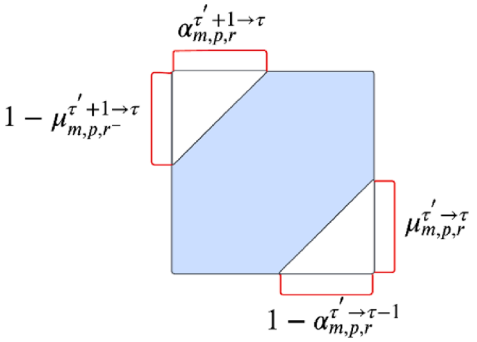

Possibility 17: $r \neq r_{m,p}^{min}$, $\tau = \min\left(\tau'' : \tau'' \in \Psi_{m,p}^{\tau'}\right)$, $\tau \neq \max\left(\tau'' : \tau'' \in \Psi_{m,p}^{\tau'}\right)$, $r \neq r_{m,p}^{\tau'\to\tau}$, and $r = r_{m,p}^{\tau'+1\to\tau}$.

$$A_{m,p,r}^{\tau'\to\tau} = 1 - 0.5 \bullet \left(1 - \mu_{m,p,r^-}^{\tau'+1\to\tau}\right) \bullet \alpha_{m,p,r}^{\tau'+1\to\tau} - 0.5 \bullet \left(\mu_{m,p,r^-}^{\tau'\to\tau} + \mu_{m,p,r}^{\tau'\to\tau}\right)$$

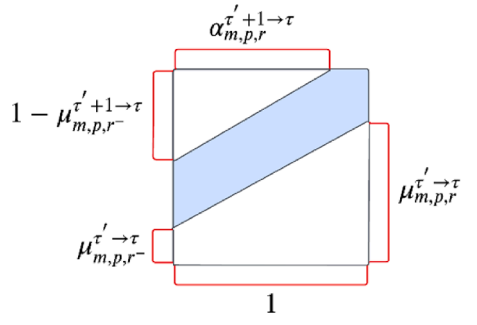

Possibility 18: $r \neq r_{m,p}^{min}$, $\tau \neq \min\left(\tau'' : \tau'' \in \Psi_{m,p}^{\tau'}\right)$, $\tau = \max\left(\tau'' : \tau'' \in \Psi_{m,p}^{\tau'}\right)$, $r = r_{m,p}^{\tau'\to\tau-1}$, and $r \neq r_{m,p}^{\tau'+1\to\tau-1}$.

$$A_{m,p,r}^{\tau'\to\tau} = 1 - 0.5 \bullet \left(\left(1 - \mu_{m,p,r^-}^{\tau'+1\to\tau}\right) + \left(1 - \mu_{m,p,r}^{\tau'+1\to\tau}\right)\right) - 0.5 \bullet \left(1 - \alpha_{m,p,r}^{\tau'\to\tau-1}\right) \bullet \mu_{m,p,r}^{\tau'\to\tau}$$

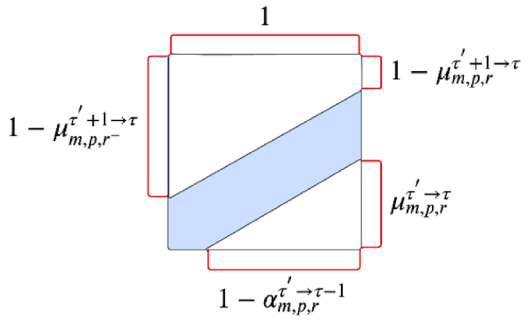

Possibility 19: $r \neq r^{min}_{m,p}$, $\tau = \min\left(\tau'' : \tau'' \in \Psi^{\tau'}_{m,p}\right)$, and $\tau = \max\left(\tau'' : \tau'' \in \Psi^{\tau'}_{m,p}\right)$.

$$A^{\tau'\to\tau}_{m,p,r} = 1 - 0.5 \bullet \left(\left(1-\mu^{\tau'+1\to\tau}_{m,p,r^-}\right) + \left(1-\mu^{\tau'+1\to\tau}_{m,p,r}\right)\right) - 0.5 \bullet \left(\mu^{\tau'\to\tau}_{m,p,r^-} + \mu^{\tau'\to\tau}_{m,p,r}\right)$$

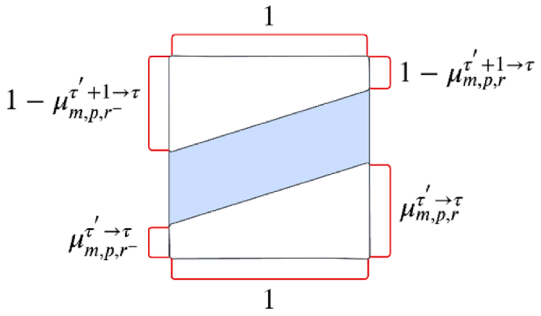

Possibility 20: $r \neq r^{min}_{m,p}$, $\tau \neq \min\left(\tau'' : \tau'' \in \Psi^{\tau'}_{m,p}\right)$, $\tau \neq \max\left(\tau'' : \tau'' \in \Psi^{\tau'}_{m,p}\right)$, $r = r^{\tau'\to\tau-1}_{m,p}$, $r = r^{\tau'\to\tau}_{m,p}$, $r = r^{\tau'+1\to\tau-1}_{m,p}$, and $r = r^{\tau'+1\to\tau}_{m,p}$.

$$A^{\tau'\to\tau}_{m,p,r} = 1 - 0.5 \bullet \left(\alpha^{\tau'+1\to\tau}_{m,p,r} + \alpha^{\tau'+1\to\tau-1}_{m,p,r}\right) - 0.5 \bullet \left(\left(1-\alpha^{\tau'\to\tau}_{m,p,r}\right) + \left(1-\alpha^{\tau'\to\tau-1}_{m,p,r}\right)\right)$$

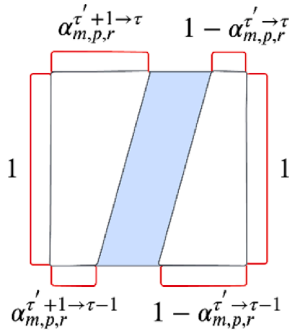

Possibility 21: $r \neq r^{min}_{m,p}$, $\tau \neq \min\left(\tau'' : \tau'' \in \Psi^{\tau'}_{m,p}\right)$, $\tau \neq \max\left(\tau'' : \tau'' \in \Psi^{\tau'}_{m,p}\right)$, $r = r^{\tau'\to\tau-1}_{m,p}$, $r \neq r^{\tau'\to\tau}_{m,p}$, $r = r^{\tau'+1\to\tau-1}_{m,p}$, and $r = r^{\tau'+1\to\tau}_{m,p}$.

$$A^{\tau'\to\tau}_{m,p,r} = 1 - 0.5 \bullet \left(\alpha^{\tau'+1\to\tau}_{m,p,r} + \alpha^{\tau'+1\to\tau-1}_{m,p,r}\right) - 0.5 \bullet \left(1-\alpha^{\tau'\to\tau-1}_{m,p,r}\right) \bullet \mu^{\tau'\to\tau}_{m,p,r}$$

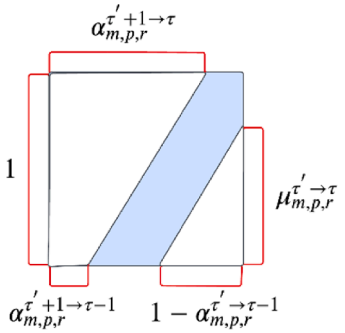

Possibility 22: $r \neq r^{min}_{m,p}$, $\tau \neq \min\left(\tau'' : \tau'' \in \Psi^{\tau'}_{m,p}\right)$, $\tau \neq \max\left(\tau'' : \tau'' \in \Psi^{\tau'}_{m,p}\right)$, $r = r^{\tau'\to\tau-1}_{m,p}$, $r = r^{\tau'\to\tau}_{m,p}$, $r \neq r^{\tau'+1\to\tau-1}_{m,p}$, and $r = r^{\tau'+1\to\tau}_{m,p}$.

$$A^{\tau'\to\tau}_{m,p,r} = 1 - 0.5 \bullet \left(1 - \mu^{\tau'+1\to\tau}_{m,p,r^-}\right) \bullet \alpha^{\tau'+1\to\tau}_{m,p,r} - 0.5 \bullet \left(\left(1 - \alpha^{\tau'\to\tau}_{m,p,r}\right) + \left(1 - \alpha^{\tau'\to\tau-1}_{m,p,r}\right)\right)$$

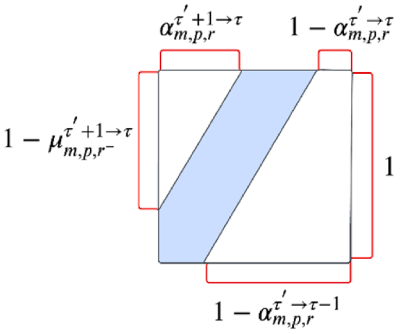

Possibility 23: $r \neq r^{min}_{m,p}$, $\tau \neq \min\left(\tau'' : \tau'' \in \Psi^{\tau'}_{m,p}\right)$, $\tau = \max\left(\tau'' : \tau'' \in \Psi^{\tau'}_{m,p}\right)$, $r = r^{\tau'\to\tau-1}_{m,p}$, and $r = r^{\tau'+1\to\tau-1}_{m,p}$.

$$A^{\tau'\to\tau}_{m,p,r} = 0.5 \bullet \left(1 - \alpha^{\tau'+1\to\tau-1}_{m,p,r}\right) \bullet \mu^{\tau'+1\to\tau}_{m,p,r} - 0.5 \bullet \left(1 - \alpha^{\tau'\to\tau-1}_{m,p,r}\right) \bullet \mu^{\tau'\to\tau}_{m,p,r}$$

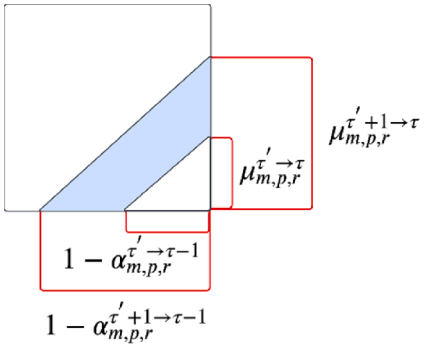

Possibility 24: $r \neq r^{min}_{m,p}$, $\tau = \min\left(\tau'' : \tau'' \in \Psi^{\tau'}_{m,p}\right)$, $\tau \neq \max\left(\tau'' : \tau'' \in \Psi^{\tau'}_{m,p}\right)$, $r = r^{\tau'\to\tau}_{m,p}$, and $r = r^{\tau'+1\to\tau}_{m,p}$.

$$A^{\tau'\to\tau}_{m,p,r} = 1 - 0.5 \bullet \left(1 - \mu^{\tau'\to\tau}_{m,p,r^-}\right) \bullet \alpha^{\tau'\to\tau}_{m,p,r} - 0.5 \bullet \left(1 - \mu^{\tau'+1\to\tau}_{m,p,r^-}\right) \bullet \alpha^{\tau'+1\to\tau}_{m,p,r}$$

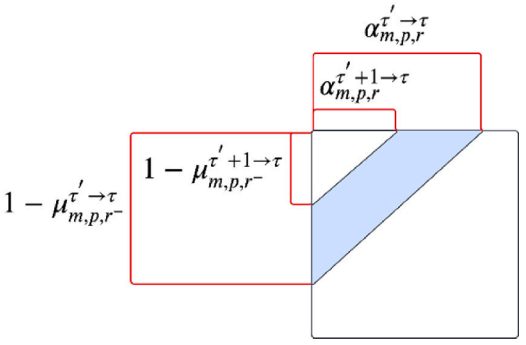

Possibility 25: $r \neq r_{m,p}^{min}$, $\tau \neq \min\left(\tau'' : \tau'' \in \Psi_{m,p}^{\tau'}\right)$, $\tau \neq \max\left(\tau'' : \tau'' \in \Psi_{m,p}^{\tau'}\right)$, $r \neq r_{m,p}^{\tau' \to \tau-1}$, $r \neq r_{m,p}^{\tau' \to \tau}$, $r \neq r_{m,p}^{\tau'+1 \to \tau-1}$, and $r \neq r_{m,p}^{\tau'+1 \to \tau}$.

$$A_{m,p,r}^{\tau' \to \tau} = 1$$

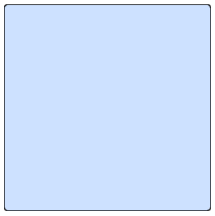

Data availability

Data will be made available on request.

References

Aghamohammadi, R., Laval, J., 2022. Parameter estimation of the macroscopic fundamental diagram: A maximum likelihood approach. Transp. Res. Part C Emerg. Technol. 140, 103678.

Alisoltani, N., Zargayouna, M., Leclercq, L., 2020. A sequential clustering method for the taxi-dispatching problem considering traffic dynamics. IEEE Intell. Transp. Syst. Mag. 12 (4), 169–181.

Alisoltani, N., Leclercq, L., Zargayouna, M., 2021. Can dynamic ride-sharing reduce traffic congestion? Transp. Res. B Methodol. 145, 212–246.

Ambühl, L., Menendez, M., 2016. Data fusion algorithm for macroscopic fundamental diagram estimation. Transp. Res. Part C Emerging Technol. 71, 184–197.

Ambühl, L., Loder, A., Zheng, N., Axhausen, K.W., Menendez, M., 2019. Approximative network partitioning for MFDs from stationary sensor data. Transp. Res. Rec. 2673 (6), 94–103.

Ambühl, L., Loder, A., Bliemer, M., Menendez, M., Axhausen, K., 2020. A functional form with a physical meaning for the macroscopic fundamental diagram. Transp. Res. B Methodol. 137, 119–132.

Ameli, M., Lebacque, J., Leclercq, L., 2020. Cross-comparison of convergence algorithms to solve trip-based dynamic traffic assignment problems. Computer-aided Civil and Infrastructure Engineering 35 (3), 219–240.

Amirgholy, M., Gao, H., 2017. Modeling the dynamics of congestion in large urban networks using the macroscopic fundamental diagram: user equilibrium, system optimum, and pricing strategies. Transp. Res. B Methodol. 104, 215–237.

Amirgholy, M., Shahabi, M., Gao, H., 2017. Optimal design of sustainable transit systems in congested urban networks: a macroscopic approach. Transportation Research Part e: Logistics and Transportation Review 103, 261–285.

Ampountolas, K., Zheng, N., Geroliminis, N., 2017. Macroscopic modelling and robust control of bi-modal multi-region urban road networks. Transp. Res. B Methodol. 104, 616–637.

Arnott, R., 2013. A bathtub model of downtown traffic congestion. J. Urban Econ. 76, 110–121.

Barmpounakis, E., Montesinos-Ferrer, M., Gonzales, E., Geroliminis, N., 2021. Empirical investigation of the emission-macroscopic fundamental diagram. Transp. Res. Part D: Transp. Environ. 101, 103090.

Batista, S., Leclercq, L., 2020. Regional dynamic traffic assignment with bounded rational drivers as a tool for assessing the emissions in large metropolitan areas. Transp. Res. Interdiscip. Perspect. 8, 100248.

Batista, S., Ingole, D., Leclercq, L., Menéndez, M., 2021a. The role of trip lengths calibration in model-based perimeter control strategies. IEEE Trans. Intell. Transp. Syst. 23 (6), 5176–5186.

Batista, S., Leclercq, L., 2019. Regional Dynamic Traffic Assignment Framework for Macroscopic Fundamental Diagram Multi-regions Models. Transp. Sci. 53 (6), 1563–1590.

Batista, S., Leclercq, L., Menendez, M., 2021b. Dynamic Traffic Assignment for regional networks with traffic-dependent trip lengths and regional paths. Transp. Res. Part C Emerging Technol. 127.

Batista, S., Seppecher, M., Leclercq, L., 2021c. Identification and characterizing of the prevailing paths on a urban network for MFD-based applications. Transp. Res. Part C Emerging Technol. 127.

Batista, S., Tilg, G., Menéndez, M., 2022. Exploring the potential of aggregated traffic models for estimating network-wide emissions. Transp. Res. Part D: Transp. Environ. 109, 103354.

Beojone, C., Geroliminis, N., 2021. On the inefficiency of ride-sourcing services towards urban congestion. Transp. Res. Part C Emerging Technol. 124, 102890.

Boyce, D., Lee, D., Ran, B., 2001. Analytical models of the dynamic traffic assignment problem. Netw. Spat. Econ. 1 (3), 377–390.

Byrd, R., Lu, P., Nocedal, J., Zhu, C., 1995. A limited memory algorithm for bound constrained optimization. SIAM J. Sci. Comput. 16 (5), 1190–1208.

Carey, M., 2004a. Link travel times I: desirable properties. Netw. Spat. Econ. 4 (3), 257–268.
Carey, M., 2004b. Link travel times II: properties derived from traffic-flow models. Netw. Spat. Econ. 4, 379–402.
Carey, M., Humphreys, P., McHugh, M., McIvor, R., 2014. Extending travel-time based models for dynamic network loading and assignment, to achieve adherence to first-in-first-out and link capacities. Transp. Res. B Methodol. 65, 90–104.
Casadei, G., Bertrand, V., Gouin, B., Canudas-de-Wit, C., 2018. Aggregation and travel time calculation over large scale traffic networks: An empiric study on the Grenoble city. Transp. Res. Part C Emerging Technol. 95, 713–730.
Cascetta, E., Nuzzolo, A., Russo, F., Vitetta, A., 1996. A modified logit route choice model overcoming path overlapping problems: specification and some calibration results for inter-urban networks. In: In: Proceedings of the 13th International Symposium on Transportation and Traffic Theory, pp. 697–711.
Castillo, E., Menéndez, J., Jiménez, P., Rivas, A., 2008. Closed form expressions for choice probabilities in the Weibull case. Transp. Res. B Methodol. 42 (4), 373–380.
Chen, Y., Gu, Z., Zheng, N., Vu, H., 2023. Optimal coordinated congestion pricing for multiple regions: a surrogate-based approach. Transportation 1–33.
Chen, A., Ryu, S., Xu, X., Choi, K., 2014. Computation and Application of the Paired Combinatorial Logit Stochastic User Equilibrium Problem. Comput. Oper. Res. 43, 68–77.
Daganzo, C., 2007. Urban gridlock: macroscopic modeling and mitigation approaches. Transp. Res. B Methodol. 41 (1), 49–62.
Daganzo, C., Lehe, L., 2015. Distance-dependent congestion pricing for downtown zones. Transp. Res. B Methodol. 75, 89–99.
Dantsuji, T., Fukuda, D., Zheng, N., 2021. Simulation-based joint optimization framework for congestion mitigation in multimodal urban network: a macroscopic approach. Transportation 48, 673–697.
de Romph, E., van Grol, H., Hamerslag, R., 1994. Control strategies for a highway network. SWOV Institute for Road Safety Research, The Netherlands.
del Castillo, J., 2012. Three new models for the flow-density relationship: derivation and testing for freeway and urban data. Transportmetrica 8 (6), 443–465.
Du, J., Rakha, H., Gayah, V., 2016. Deriving macroscopic fundamental diagrams from probe data: Issues and proposed solutions. Transp. Res. Part C Emerging Technol. 66, 136–149.
Duncan, L., Watling, D., Connors, R., Rasmussen, T., Nielsen, O., 2020. Path Size Logit Route Choice Models: Issues with Current Models, a New Internally Consistent Approach, and Parameter Estimation on a Large-Scale Network with GPS Data. Transp. Res. B Methodol. 135, 1–40.
Duncan, L., Watling, D., Connors, R., Rasmussen, T., Nielsen, O., 2021. A bounded path size route choice model excluding unrealistic routes: Formulation and estimation from a large-scale GPS study. Transportmetrica a: Transport Science 18 (3), 435–493.
Duncan, L., Watling, D., Connors, R., Rasmussen, T., Nielsen, O., 2023. Choice set robustness and internal consistency in correlation-based logit stochastic user equilibrium models. Transportmetrica a: Transport Science 19 (3), 2063969.
Fosgerau, M., 2015. Congestion in the bathtub. Econ. Transp. 4 (4), 241–255.
Fu, H., Wang, Y., Tang, X., Zheng, N., Geroliminis, N., 2020. Empirical analysis of large-scale multimodal traffic with multi-sensor data. Transp. Res. Part C Emerging Technol. 118, 102725.
Fu, H., Chen, S., Chen, K., Kouvelas, A., Geroliminis, N., 2021. Perimeter control and route guidance of multi-region mfd systems with boundary queues using colored petri nets. IEEE Trans. Intell. Transp. Syst. 23 (8), 12977–12999.
Gao, X., Gayah, V., 2018. An analytical framework to model uncertainty in urban network dynamics using macroscopic fundamental diagrams. Transp. Res. B Methodol. 117, 660–675.
Genser, A., Kouvelas, A., 2022. Dynamic optimal congestion pricing in multi-region urban networks by application of a Multi-Layer-Neural network. Transp. Res. Part C Emerging Technol. 134, 103485.
Geroliminis, N., Daganzo, C., 2008. Existence of urban-scale macroscopic fundamental diagrams: Some experimental findings. Transp. Res. B 42 (9), 759–770.
Geroliminis, N., Haddad, J., Ramezani, M., 2012. Optimal perimeter control for two urban regions with macroscopic fundamental diagrams: A model predictive approach. IEEE Trans. Intell. Transp. Syst. 14 (1), 348–359.
Geroliminis, N., Sun, J., 2011. Hysteresis phenomena of a macroscopic fundamental diagram in freeway networks. Procedia – Social and Behavioral Sciences 17, 213–228.
Geroliminis, N., Zheng, N., Ampountolas, K., 2014. A three-dimensional macroscopic fundamental diagram for mixed bi-modal urban networks. Transp. Res. Part C Emerging Technol. 42, 168–181.
Greenshields, B.D., Bibbins, J.R., Channing, W.S. and Miller, H.H., 1935, December. A study of traffic capacity. In Highway research board proceedings (Vol. 14, No. 1, pp. 448–477). https://onlinepubs.trb.org/Onlinepubs/hrbproceedings/14/14P1-023.pdf.
Gu, Z., Saberi, M., 2021. Simulation-based optimization of toll pricing in large-scale urban networks using the network fundamental diagram: A cross-comparison of methods. Transp. Res. Part C Emerging Technol. 122, 102894.
Gu, Z., Waller, S., Saberi, M., 2019. Surrogate-based toll optimization in a large-scale heterogeneously congested network. Computer-Aided Civil and Infrastructure Engineering 34 (8), 638–653. https://doi.org/10.1111/mice.12444.
Gu, Z., Shafiei, S., Liu, Z., Saberi, M., 2018. Optimal distance-and time-dependent area-based pricing with the Network Fundamental Diagram. Transp. Res. Part C Emerging Technol. 95, 1–28.
Guo, Q., Ban, X., 2020. Macroscopic fundamental diagram based perimeter control considering dynamic user equilibrium. Transp. Res. B Methodol. 136, 87–109.
Haddad, J., 2017a. Optimal coupled and decoupled perimeter control in one-region cities. Control Eng. Pract. 61, 134–148.
Haddad, J., 2017b. Optimal perimeter control synthesis for two urban regions with aggregate boundary queue dynamics. Transp. Res. B Methodol. 96, 1–25.
Haddad, J., Ramezani, M., Geroliminis, N., 2013. Cooperative traffic control of a mixed network with two urban regions and a freeway. Transp. Res. B Methodol. 54, 17–36.
Hosseinzadeh, F., Moshahedi, N., Kattan, L., 2023. An MFD approach to route guidance with consideration of fairness. Transp. Res. Part C Emerging Technol. 157, 104359.
Huang, Y., Xiong, J., Sumalee, A., Zheng, N., Lam, W., He, Z., Zhong, R., 2020. A dynamic user equilibrium model for multi-region macroscopic fundamental diagram systems with time-varying delays. Transp. Res. B Methodol. 131, 1–25.
Huang, Y., Sun, D., Zhang, S., 2022. Three-dimensional macroscopic fundamental diagram for car and bicycle heterogeneous traffic. Transportmetrica b: Transport Dynamics 10 (1), 312–339.
Huang, Y., Xiong, J., Hsu, S., Sumalee, A., Lam, W., Zhong, R., 2024. A comparison of the accumulation-based. In: Transportmetrica, A. (Ed.), Trip-Based and Time Delay Macroscopic Fundamental Diagram Models. Transport Science, pp. 1–37.
Huang, C., Zheng, N., Zhang, J., 2019. Investigation of bimodal macroscopic fundamental diagrams in large-scale urban networks: empirical study with GPS data for Shenzhen city. Transp. Res. Rec. 2673 (6), 114–128.
Janson, B., 1991b. Dynamic traffic assignment for urban road networks. Transp. Res. B Methodol. 25 (2–3), 143–161.
Janson B, (1991a). Convergent algorithm for dynamic traffic assignment. Transportation Research Record, (1328).
Johari, M., Keyvan-Ekbatani, M., 2024. Macroscopic modeling of mixed bi-modal urban networks: A hybrid model of accumulation-and trip-based principles. Transp. Res. B Methodol. 182, 102921. https://doi.org/10.1016/j.trb.2024.102921.
Kessels F, (2019). The Fundamental Diagram. In: Traffic Flow Modelling. EURO Advanced Tutorials on Operational Research, p.21-34.
Keyvan-Ekbatani, M., Kouvelas, A., Papamichail, I., Papageorgiou, M., 2012. Exploiting the fundamental diagram of urban networks for feedback-based gating. Transp. Res. B Methodol. 46 (10), 1393–1403.
Keyvan-Ekbatani, M., Papageorgiou, M., Knoop, V., 2015a. Controller design for gating traffic control in presence of time-delay in urban road networks. Transp. Res. Part C Emerging Technol. 59, 308–322.
Keyvan-Ekbatani, M., Yildirimoglu, M., Geroliminis, N., Papageorgiou, M., 2015b. Multiple concentric gating traffic control in large-scale urban networks. IEEE Trans. Intell. Transp. Syst. 16 (4), 2141–2154.
Kitthamkesorn, S., Chen, A., 2013. Path-size weibit stochastic user equilibrium model. Transp. Res. B Methodol. 57, 378–397.
Kitthamkesorn, S., Chen, A., 2014. Unconstrained weibit stochastic user equilibrium model with extensions. Transp. Res. B Methodol. 59, 1–21.
Knoop, V., Hoogendoorn, S., Van Lint, J., 2012. Routing strategies based on macroscopic fundamental diagram. Transp. Res. Rec. 2315 (1), 1–10.

Kouvelas, A., Saeedmanesh, M., Geroliminis, N., 2017. Enhancing model-based feedback perimeter control with data-driven online adaptive optimization. Transp. Res. B Methodol. 96, 26–45.
Lamotte, R., Geroliminis, N., 2016. The Morning Commute in Urban Areas: Insights from Theory and Simulation No, 16–2003.
Lamotte, R., Geroliminis, N., 2017. The morning commute in urban areas with heterogeneous trip lengths. Transp. Res. B Methodol. 117, 794–810.
Leclercq, L., Sénécat, A., Mariotte, G., 2017. Dynamic macroscopic simulation of on-street parking search: A trip-based approach. Transp. Res. B Methodol. 101, 268–282.
Lehe, L., 2017. Downtown tolls and the distribution of trip lengths. Econ. Transp. 11, 23–32.
Lentzakis, A., Seshadri, R., Ben-Akiva, M., 2023. Predictive distance-based road pricing – Designing tolling zones through unsupervised learning. Transp. Res. A Policy Pract. 170, 103611.
Liu, W., Geroliminis, N., 2017. Doubly dynamics for multi-modal networks with park-and-ride and adaptive pricing. Transp. Res. B Methodol. 102, 162–179.
Liu, H., He, X., He, B., 2009. Method of successive weighted averages (MSWA) and self-regulated averaging schemes for solving stochastic user equilibrium problem. Netw. Spat. Econ. 9 (4), 485–503.
Loder, A., Ambühl, L., Menendez, M., Axhausen, K., 2017. Empirics of multi-modal traffic networks – Using the 3D macroscopic fundamental diagram. Transp. Res. Part C Emerging Technol. 82, 88–101.
Loder, A., Bliemer, M., Axhausen, K., 2022. Optimal pricing and investment in a multi-modal city – Introducing a macroscopic network design problem based on the MFD. Transp. Res. A Policy Pract. 156, 113–132.
Lopez, C., Leclercq, L., Krishnakumari, P., Chiabaut, N., van Lint, H., 2017. Revealing the day-to-day regularity of urban congestion patterns with 3D speed maps. Scientific Report 7 (1), 1–11.
Ma, W., Huang, Y., Jin, X., Zhong, R., 2024. Functional form selection and calibration of macroscopic fundamental diagrams. Physica A 640, 129691.
Mansourianfar, M., Gu, Z., Waller, S., Saberi, M., 2021. Joint routing and pricing control in congested mixed autonomy networks. Transp. Res. Part C Emerging Technol. 131, 103338.
Mansourianfar, M., Gu, Z., Saberi, M., 2024. Joint Routing and Pricing Control in Bimodal Mixed Autonomy Networks with Elastic Demand and Three-Dimensional Passenger Macroscopic Fundamental Diagram. Transp. Res. Rec., 03611981241243080
Mariotte, G., Leclercq, L., Laval, J., 2017. Macroscopic urban dynamics: Analytical and numerical comparisons of existing models. Transp. Res. B Methodol. 101, 245–267.
Mariotte, G., Leclercq, L., 2019. Flow exchanges in multi-reservoir systems with spillbacks. Transp. Res. B 122, 327–349.
Mariotte, G., Leclercq, L., Batista, F., Krug, J., Paipuri, M., 2020. Calibration and validation of multi-reservoir MFD models: A case study in Lyon. Transp. Res. B Methodol. 136, 62–86.
McFadden, D., Train, K., 2000. Mixed MNL models for discrete response. J. Appl. Economet. 15 (5), 447–470.
Menelaou, C., Timotheou, S., Kolios, P., Panayiotou, C., 2023. Convexification approaches for regional route guidance and demand management with generalized MFDs. Transp. Res. Part C Emerging Technol. 154, 104245.
Quddus, M., Ochieng, W., Noland, R., 2007. Current map-matching algorithms for transport applications: State-of-the art and future research directions. Transp. Res. Part C Emerging Technol. 15 (5), 312–328.
Raadsen, M., Bliemer, M., Bell, M., 2020. Aggregation, disaggregation and decomposition methods in traffic assignment: historical perspectives and new trends. Transp. Res. B Methodol. 139, 199–223.
Ramezani, M., Valadkhani, A., 2023. Dynamic ride-sourcing systems for city-scale networks-Part I: Matching design and model formulation and validation. Transp. Res. Part C Emerging Technol. 152, 104158.
Ramezani, M., Haddad, J., Geroliminis, N., 2015. Dynamics of heterogeneity in urban networks: aggregated traffic modeling and hierarchical control. Transp. Res. B Methodol. 74, 1–19.
Ramezani, M., Nourinejad, M., 2018. Dynamic modeling and control of taxi services in large-scale urban networks: A macroscopic approach. Transp. Res. Part C Emerging Technol. 94, 203–219.
Rasmussen, T., Duncan, L., Watling, D., Nielsen, O., 2024. Local Detouredness: A New Phenomenon for Modelling Route Choice and Traffic Assignment. Transportation Research Part B: Methodological.
Rasmussen T, Brun B, & Hansen C, (2021). Dynamic Traffic Assignment in a large-scale transport model (COMPASS). Proceedings of Trafikdage, August 23-24, Aalborg Denmark.
Rich, J., Hansen, C., 2016. The danish national passenger model – model specification and results. Eur. J. Transp. Infrastruct. Res. 16 (4).
Saeedmanesh, M., Geroliminis, N., 2016. Clustering of heterogeneous networks with directional flows based on "snake" similarities. Transp. Res. B Methodol. 91, 250–269.
Saeedmanesh, M., Geroliminis, N., 2017. Dynamic clustering and propagation of congestion in heterogeneously congested urban traffic networks. Transp. Res. B Methodol. 105, 193–211.
Sbayti, H., Lu, C., Mahmassani, H., 2007. Efficient implementation of method of successive averages in simulation-based dynamic traffic assignment models for large-scale network applications. Transp. Res. Rec. 2029 (1), 22–30.
Sheffi, Y., 1985. Urban Transportation Networks: Equilibrium Analysis with Mathematical Programming Methods. Prentice-Hall.
Smulders, S., 1990. Control of freeway traffic flow by variable speed signs. Transp. Res. B Methodol. 24 (2), 111–132.
Valadkhani, A., Ramezani, M., 2023. Dynamic ride-sourcing systems for city-scale networks, Part II: Proactive vehicle repositioning. Transp. Res. Part C Emerging Technol. 152, 104159.
Wang, X., Gayah, V., 2021. Cordon-Based Pricing Schemes for Mixed Urban-Freeway Networks using Macroscopic Fundamental Diagrams. Transp. Res. Rec. 2675 (10), 1339–1351.
Wardrop, J., 1952. Some theoretical aspects of road traffic research. Proc. Inst. Civ. Eng. 1, 325–378.
Watling, D., Rasmussen, T., Prato, C., Nielsen, O., 2015. Stochastic user equilibrium with equilibrated choice sets: Part I – Model formulations under alternative distributions and restrictions. Transp. Res. B Methodol. 77, 166–181.
Wismans, L., Berkum, E., Bliemer, M., 2011. Modelling Externalities using Dynamic Traffic Assignment Models: A Review. Transp. Rev. 31 (4), 521–545.
Wu, C., Yang, L., Du, J., Pei, X., Wong, S., 2024. Continuum dynamic traffic models with novel local route-choice strategies for urban cities. Transp. Res. B Methodol. 181, 102888.
Xu, X., Chen, A., 2013. C-logit stochastic user equilibrium model with elastic demand. Transp. Plan. Technol. 36 (5), 463–478.
Yang, C., Chen, A., Xu, X., 2013. Improved partial linearization algorithm for solving the combined travel-destination-mode-route choice problem. J. Urban Plann. Dev. 139 (1), 22–32.
Yao, J., Chen, A., Ryu, S., Shi, F., 2014. A general unconstrained optimization formulation for the combined distribution and assignment problem. Transp. Res. B Methodol. 59, 137–160.
Yildirimoglu, M., Geroliminis, N., 2014. Approximating dynamic equilibrium conditions with macroscopic fundamental diagrams. Transp. Res. B Methodol. 70, 186–200.
Yildirimoglu, M., Ramezani, M., Geroliminis, N., 2015. Equilibrium analysis and route guidance in large-scale networks with MFD dynamics. Transp. Res. Procedia 9, 185–204.
Zheng, N., Geroliminis, N., 2013. On the distribution of urban road space for multimodal congested networks. Procedia Soc. Behav. Sci. 80, 119–138.
Zheng, N., Geroliminis, N., 2016. Modeling and optimization of multimodal urban networks with limited parking and dynamic pricing. Transp. Res. B Methodol. 83, 36–58.
Zheng, N., Geroliminis, N., 2020. Area-based equitable pricing strategies for multimodal urban networks with heterogeneous users. Transp. Res. A Policy Pract. 136, 357–374.

Zhong, R., Chen, C., Huang, Y., Sumalee, A., Lam, W., Xu, D., 2018a. Robust perimeter control for two urban regions with macroscopic fundamental diagrams: A control-Lyapunov function approach. Transp. Res. B Methodol. 117, 687–707.
Zhong, R., Huang, Y., Chen, C., Lam, W., Xu, D., Sumalee, A., 2018b. Boundary conditions and behavior of the macroscopic fundamental diagram based network traffic dynamics: a control systems perspective. Transp. Res. B Methodol. 111, 327–355.
Zhong, R., Xiong, J., Huang, Y., Sumalee, A., Chow, A., Pan, T., 2020. Dynamic system optimum analysis of multi-region macroscopic fundamental diagram systems with state-dependent time-varying delays. IEEE Trans. Intell. Transp. Syst. 21 (9), 4000–4016.
Zhou, Z., Chen, A., Bekhor, S., 2012. C-logit stochastic user equilibrium model: formulations and solution algorithm. Transportmetrica 8 (1), 17–41.